Technische Universität München
TUM School of Natural Sciences

# Wigner Tomography of Quantum States and Processes and its Implementation on Near-Term Quantum Devices

Amit Devra

Vollständiger Abdruck der von der TUM School of Natural Sciences der Technischen Universität München zur Erlangung eines

**Doktors der Naturwissenschaften (Dr. rer. nat.)**

genehmigten Dissertation.

Vorsitz: Prof. Dr. Bernd Reif

Prüfer der Dissertation:

1. Prof. Dr. Steffen J. Glaser
2. Prof. Dr. Stefan Filipp
3. Prof. Dr. Balint Koczor (University of Oxford)

Die Dissertation wurde am 18.03.2024 bei der Technischen Universität München eingereicht und durch die TUM School of Natural Sciences am 04.05.2024 angenommen.

# Declaration

I hereby declare that the content of my thesis is an original work and is based on the following publications, which have already been submitted or planned to be submitted to scientific journals:

- A. Devra, N. J. Glaser, D. Huber, and S. J. Glaser. *Wigner state and process tomography on near-term quantum devices.* Preprint: arXiv:2302.12725.
- A. Devra, L. Van Damme, F. vom Ende, E. Malvetti, and S. J. Glaser. *Wigner tomography of unknown quantum processes.* In preparation.

Garching, 13.03.2024 Amit Devra

# List of Publications

- A. Devra, P. Prabhu, H. Singh, Arvind, and K. Dorai. *Efficient experimental design of high-fidelity three-qubit quantum gates via genetic programming.* Quantum Inf Process 17, 67 (2018).
- V. Martikyan, A. Devra, D. Guéry-Odelin, S. J. Glaser, and D. Sugny. *Robust control of an ensemble of springs: Application to ion cyclotron resonance and two-level quantum systems.* Phys. Rev. A 102, 053104 (2020).
- A. Devra, N. J. Glaser, D. Huber, and S. J. Glaser. *Wigner state and process tomography on near-term quantum devices.* Preprint: arXiv:2302.12725.
- A. Devra, L. Van Damme, F. vom Ende, E. Malvetti, and S. J. Glaser. *Wigner tomography of unknown quantum processes.* In preparation.
- Z. Zhang, L. Van Damme, A. Devra, S. J. Glaser, and A. Alberti. *Scalable, recoil-free quantum gates with optical qubits.* In preparation.
- Z. Zhang, L. Van Damme, A. Devra, S. J. Glaser, and A. Alberti. *Time-optimal optical qubit gate with suppressed photon recoil.* In preparation.

# Abstract

For the development of fully error-corrected quantum computers, an understanding of the current near-term noisy devices is vital. Experimental verification of quantum operators plays an essential role in characterizing and thereby improving the performance of a quantum computer. The underlying theory of quantum computing is complex, and gaining a deeper understanding of the quantum system and its dynamics is crucial. In this context, visualization techniques assume a significant role, especially those that can directly visualize quantum operators, such as density matrices, processes, Hamiltonians, etc.

The DROPS (Discrete Representation of OPeratorS) representation is a visualization tool that visualizes operators using shapes (*droplets*) assembled from linear combinations of spherical harmonics. This thesis presents a scanning-based tomography approach that experimentally tomographs the droplets corresponding to density matrices and processes. Building on the underlying theory of Wigner state and process tomography initially developed for an ensemble-based NMR (nuclear magnetic resonance) setting, this thesis introduces a reformulation of this theory tailored for pure-state general-purpose quantum computers.

Furthermore, this work tackles the existing limitation of Wigner tomography, which was previously applicable only to *known* unitary processes, by extending this theory to encompass the tomography of *unknown* unitary processes. This thesis provides an experimental methodology for directly implementing scanning-based tomography techniques on pure-state quantum computers and also presents the experimental results of our tomography approaches performed on IBM quantum devices.

# Acknowledgements

I would like to start by saying a big thank you to Prof. Steffen Glaser for being an exceptional supervisor, teacher, and mentor. Your passion for science continues to encourage me. Throughout this journey, I have learned a lot from you. Thank you for giving me various exciting opportunities and for believing in me. This definitely would not have been possible without your constant support.

I would like to extend my gratitude to everyone involved in the QuSCo project, where this entire journey began. In particular, I want to acknowledge Prof. Dominique Sugny for his mentorship, Prof. Cristiane Koch for organizing outstanding scientific and non-scientific events, and Prof. Stefan Filipp and Mattia Giardini. I believe this was the best beginning one could get, with the best PIs and the wonderful ESRs, who have become really good friends. I would like to acknowledge all my friends and colleagues involved in the QuSCo project. My special thanks go to Shaeema, Tiantian, Max, Nimba, Vardan, Alastair, and Federico for being fantastic friends.

I would like to express my sincere appreciation to the Glaser group, which has been incredibly supportive throughout my PhD journey. I'd like to thank Ms. Namalee Danwatte for her continuous administrative support, which made it easier for us to work with all the bureaucratic work involved. Special thanks to Dr. Raimund Marx for being helpful on several occasions and for inspiring me to invest in a camera (which I haven't done yet) through his exceptional nature photography skills. Furthermore, I want to express my gratitude to Dr. Thomas Schulte-Herbrüggen for all the interesting scientific and non-scientific conversations over coffee.

I would like to thank my office mates Leo, Emanuel, and Amanda (formerly) for fostering a friendly and productive work environment and the much-needed post-work drinking sessions. Special thanks to Moritz for his IT-related help and his friendly conversations, and Dennis for his support at work and during our badminton sessions. Additionally, I extend my thanks to former colleagues Bálint Koczor, Michael Tesch, and Frederik vom Ende for providing a friendly work environment.

I extend my sincere thanks to the funding agencies EU-Horizon 2020 and Munich Quantum Valley for their support of this work. I would also like to thank Niklas Glaser for his contribution to this work. I acknowledge the use of IBM Quantum services for this work. A special note of appreciation goes to Dr. Sabine Tornow for her assistance with the IBM devices. Furthermore, I thank my Munich Quantum Valley (MQV) colleagues, who have helped me gain valuable management skills.

Of course, this would not have been even nearly possible without the continuous encouragement from my parents. They have been a supportive pillar and continue motivating me to aim higher. I am certain that nobody will celebrate this success more than they do. My heartfelt gratitude extends to my sisters, Sangeeta and Nisha, and my brothers-in-law, Vijay and Prashant, for always being there for me and for all your love and support. A special thanks to my uncle, Nilesh, for sparking scientific and non-scientific conversations that motivated me to pursue science.

Some things remain constant in life, irrespective of highs and lows, which brings me to my friends Himanshu and Rohan, who have been tremendously supportive throughout. Also, big thanks to Katrin, Kira, Anubhuti, Melina, Ashima, Divanshu, Marco, Nikhil, Gabi, Yonatan, Selam, Atul, Ajit, JP, and Mihai for all the wonderful and memorable conversations that have made this journey enjoyable. I would also like to express my thanks to Karl for his friendship, invaluable assistance during this time, and the many insightful conversations we've shared.

Last but certainly not least, I am deeply grateful, with all my heart, to Priyanka Bansal, who has been a constant presence in my life. She played an essential part during this journey and provided me with an escape to Switzerland whenever needed. Her support throughout is invaluable. Thank you, Priyanka, for your continuous encouragement!

I would also like to acknowledge Karl and Priyanka for their helpful comments on the thesis. I also would like to acknowledge Nitin Kachariya for his help in the thesis submission.

Thank you to everyone who has been part of this journey with me directly or indirectly for your motivation and encouragement.

Lastly, thank you, dear reader, for your interest in this work.

*To my unwavering support system – parents, family, and friends.*

# Contents

Chapter

# 1 Introduction

This chapter is dedicated to describing fundamental concepts of quantum computing, with a primary focus on the visualization of quantum operators using DROPS representation [1], which establishes the foundation of this work.

## 1.1 Quantum computing

Quantum computers leverage the principles of quantum physics to execute computational processes, distinguishing themselves from classical computers, which rely on classical physics principles. In classical computing, information is encoded as 'bits', short for binary digits with two possible states: "0" or "1". Quantum computers utilize 'qubits', a portmanteau of 'quantum' and 'bit' [2], as a fundamental computation unit. Qubits can exist in various superpositions of states, simultaneously representing both 0 and 1. This state encoding facilitates parallel computation, contributing to the accelerated processing capabilities of quantum computers. These properties make quantum computers powerful enough to provide a speedup over their classical counterparts for solving certain complex algorithms. In recent years, quantum computing has seen a remarkable advancement, but many challenges remain to overcome. Here, we briefly introduce some important concepts of quantum computing.

### 1.1.1 Quantum state

A general single qubit ($N = 1$) state can be written down as a linear combination of basis states:

$$|\psi\rangle = c_0|0\rangle + c_1|1\rangle. \tag{1.1}$$

This linear combination of states is often referred to as *superposition* [3]. The complex coefficients $c_0$ and $c_1$ are the probability amplitudes, i.e., the probability after measurement to find a qubit in state $|0\rangle$ is $p_0 = |c_0|^2$ and in state $|1\rangle$ is $p_1 = |c_1|^2$. These probabilities sum to one, i.e., $p_0 + p_1 = 1$. The states can be written down in the state-vector matrix form as:

$$|0\rangle = \begin{pmatrix} 1 \\ 0 \end{pmatrix} \quad \text{and} \quad |1\rangle = \begin{pmatrix} 0 \\ 1 \end{pmatrix}. \tag{1.2}$$

These pure states can be geometrically represented on a Bloch sphere as shown in Fig. 1.1.

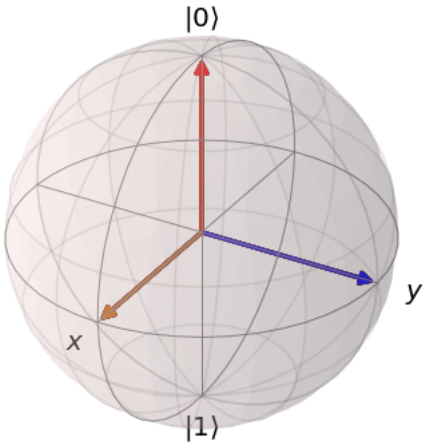


**Figure 1.1:** Representation of a single qubit state on the surface of a Bloch sphere. The north and south poles correspond to state $|0\rangle$ and $|1\rangle$, respectively. On the transverse plane, the $x$ axis corresponds to an equal superposition state $|\psi\rangle = \sqrt{\frac{1}{2}}(|0\rangle + |1\rangle)$, for example.

Similarly, for a two-qubit ($N = 2$) system, a general quantum state can be written as

$$|\psi\rangle = c_{00}|00\rangle + c_{01}|01\rangle + c_{10}|10\rangle + c_{11}|11\rangle, \tag{1.3}$$

where $|01\rangle = |0\rangle \otimes |1\rangle$, refers to state of qubit one is $|0\rangle$ and the state of qubit two is $|1\rangle$, for example. The symbol '$\otimes$' represents the tensor or Kronecker product.

In practical scenarios, a state generally can not be written in terms of state vectors and must be expressed as a statistical ensemble of multiple states. This statistical mixture is usually called a 'mixed' state and is described by a density matrix.

### 1.1.2 Density matrix

The state vector formalism (Eq. 1.1 and Eq. 1.3) only describes a 'pure' state, i.e., states which can be precisely defined at every point in time. A density matrix or density operator represents a quantum system whose state is not fully known [3]. A mathematical description of the density matrix for a given quantum system with different states $|\psi_i\rangle$ and corresponding probability $p_i$ is:

$$\rho = \sum_i p_i |\psi_i\rangle\langle\psi_i|, \tag{1.4}$$

where $\rho$ is a density matrix of size $2^N \times 2^N$ for a system of $N$ qubits.

### 1.1.3 Quantum gates

For performing any computation, it is imperative to manipulate the state of a qubit, which is achieved by quantum gates in quantum computing. For an $N$ qubit system, quantum gates or processes are represented by a $2^N \times 2^N$ unitary matrices. An initial state $|\psi_i\rangle$ evolves after an application of a quantum gate $U$ as:

$$|\psi_f\rangle = U|\psi_i\rangle, \tag{1.5}$$

where $|\psi_f\rangle$ is the final state. Similarly, in the density matrix representation, an initial density matrix $\rho_i = |\psi_i\rangle\langle\psi_i|$ evolves to a final density matrix $\rho_f$ after an application of a quantum gate $U$ as:

$$\rho_f = U\rho_i U^\dagger, \tag{1.6}$$

where $U^\dagger$ is the complex conjugate of $U$, and $UU^\dagger = \mathbb{1}$.

#### Single-qubit gates

For a single qubit, a unitary gate is a rotation around an axis in a Bloch sphere (see Fig. 1.1). For example, an X (or NOT) gate is given by:

$$\mathrm{X} = \begin{pmatrix} 0 & 1 \\ 1 & 0 \end{pmatrix}, \tag{1.7}$$

and is achieved by a rotation of $\pi$ radians around the $x$ axis. This gate inverts the state of a qubit, for example, $|0\rangle \to |1\rangle$. Another important and fundamental gate in quantum computation is a Hadamard (H) gate, the matrix form of which is given by:

$$\mathrm{H} = \sqrt{\frac{1}{2}} \begin{pmatrix} 1 & 1 \\ 1 & -1 \end{pmatrix}. \tag{1.8}$$

This gate creates an equal superposition state when applied on a computational basis state, i.e., $|0\rangle \to \sqrt{\frac{1}{2}}(|0\rangle + |1\rangle)$. This gate is a rotation of angle $\pi$ around the diagonal axis between the $x$ and $z$ axes.

The matrix form of the most general single qubit rotation, which is also known as $\mathrm{U}_3$ gate, is (up to a global phase) given by

$$\mathrm{U}_3(\theta, \phi, \lambda) = \begin{pmatrix} \cos(\theta/2) & -\mathrm{e}^{i\lambda}\sin(\theta/2) \\ \mathrm{e}^{i\phi}\sin(\theta/2) & \mathrm{e}^{i\lambda+i\phi}\cos(\theta/2) \end{pmatrix}, \tag{1.9}$$

which can be equivalently written in the form of the following Euler angle decomposition [4]

$$\begin{aligned} \mathrm{U}_3(\theta, \phi, \lambda) &= RZ(\phi)RY(\theta)RZ(\lambda) \\ &= RZ(\phi)RX(-\pi/2)RZ(\theta)RX(\pi/2)RZ(\lambda). \end{aligned} \tag{1.10}$$

This corresponds to a rotation of angle $\lambda$ around the $z$ axis, followed by a rotation of $\theta$ around the $y$ axis and a rotation of $\phi$ around the $z$ axis.

In general, given a *rotation angle* $\gamma$, the rotation operator is given by: $RX(\gamma) = e^{-i\gamma\sigma_x/2}$, $RY(\gamma) = e^{-i\gamma\sigma_y/2}$, and $RZ(\gamma) = e^{-i\gamma\sigma_z/2}$, where $\sigma_x$, $\sigma_y$, and $\sigma_z$ are the Pauli matrices, defined as:

$$\sigma_x = \begin{pmatrix} 0 & 1 \\ 1 & 0 \end{pmatrix}, \sigma_y = \begin{pmatrix} 0 & -i \\ i & 0 \end{pmatrix}, \sigma_z = \begin{pmatrix} 1 & 0 \\ 0 & -1 \end{pmatrix}. \tag{1.11}$$

The values of three Euler angles $\lambda, \theta, \phi$ in Eq. 1.10 can be adjusted to implement any single qubit rotation or gate [4]. For example, $\mathrm{U}_3(\theta, -\pi/2, \pi/2)$ corresponds to a rotation around the $x$ axis by an angle $\theta$ and $\mathrm{U}_3(\theta, 0, 0)$ corresponds to a rotation around the $y$ axis by an angle $\theta$. Further two or multi-qubit gates can be designed based on these single-qubit rotations.

**Multi-qubit gates**

In addition to the fundamental single-qubit gates described above, we highlight some multi-qubit gates here. For multi-qubit systems, an important gate is the SWAP gate, which exchanges the state of the qubits, i.e., $|00\rangle \to |00\rangle$, $|01\rangle \to |10\rangle$, $|10\rangle \to |01\rangle$, and $|11\rangle \to |11\rangle$. Its matrix representation is given by:

$$\mathrm{SWAP} = \begin{pmatrix} 1 & 0 & 0 & 0 \\ 0 & 0 & 1 & 0 \\ 0 & 1 & 0 & 0 \\ 0 & 0 & 0 & 1 \end{pmatrix}. \tag{1.12}$$

Another important class of gates is controlled gates, which only act on the target qubits if the control qubit is in state $|1\rangle$. For example, a controlled-NOT (CNOT) gate is crucial for establishing entanglement between qubits in a two-qubit system. Considering the first qubit as a control qubit, a matrix description of the CNOT gate is given by:

$$\mathrm{CNOT} = \begin{pmatrix} 1 & 0 & 0 & 0 \\ 0 & 1 & 0 & 0 \\ 0 & 0 & 0 & 1 \\ 0 & 0 & 1 & 0 \end{pmatrix}. \tag{1.13}$$

This gate transforms the two-qubit computational basis states 1.3 as: $|00\rangle \to |00\rangle$, $|01\rangle \to |01\rangle$, $|10\rangle \to |11\rangle$, and $|11\rangle \to |10\rangle$.

Another important controlled gate is a three-qubit controlled SWAP (CSWAP) gate, also known as the Fredkin gate. This gate swaps the state of two target qubits when

the control qubit is in state $|1\rangle$. Considering the first qubit as a control qubit, a matrix description of the CSWAP gate is given by:

$$\text{CSWAP} = \begin{pmatrix} 1 & 0 & 0 & 0 & 0 & 0 & 0 & 0 \\ 0 & 1 & 0 & 0 & 0 & 0 & 0 & 0 \\ 0 & 0 & 1 & 0 & 0 & 0 & 0 & 0 \\ 0 & 0 & 0 & 1 & 0 & 0 & 0 & 0 \\ 0 & 0 & 0 & 0 & 1 & 0 & 0 & 0 \\ 0 & 0 & 0 & 0 & 0 & 0 & 1 & 0 \\ 0 & 0 & 0 & 0 & 0 & 1 & 0 & 0 \\ 0 & 0 & 0 & 0 & 0 & 0 & 0 & 1 \end{pmatrix}. \tag{1.14}$$

This gate transforms the three-qubit computational basis as: $|000\rangle \to |000\rangle$, $|001\rangle \to |001\rangle$, $|010\rangle \to |010\rangle$, $|011\rangle \to |011\rangle$, $|100\rangle \to |100\rangle$, $|101\rangle \to |110\rangle$, $|110\rangle \to |101\rangle$, and $|111\rangle \to |111\rangle$. This gate also plays a crucial role in the work presented in this thesis (see Chapter 4).

## 1.2 Visualization of quantum operators

Visualizing quantum operators, such as density matrices, processes (quantum gates), Hamiltonians, etc., is crucial for understanding a quantum system and its dynamics. The state of a single qubit system can be visualized using a Bloch vector on a three-dimensional Bloch sphere, as illustrated in Fig. 1.1. However, extending this visualization to density matrices or even pure-state multi-qubit systems introduces challenges, where conventional methods like the skyscraper representation of a density matrix [3] lack intuitive insight (see left panel of Fig. 1.2). The DROPS (Discrete Representation of OPeratorS) representation [1, 5] emerges as a vital tool, offering a sophisticated visualization technique for quantum operators. DROPS representation provides a rich visualization of quantum operators and helps to understand a quantum system and its dynamics intuitively, as illustrated using an example in Fig. 1.2.

DROPS representation was initially introduced by Garon et al. [1, 6] for coupled spin-1/2 system and was later extended for up to six coupled spins in work by Leiner et al. [7]. DROPS uses a generalization of continuous phase-space representation over a sphere, which is also known as Wigner representation for spins [8, 9]. This visualization approach is based on Stratonovich's postulates [10] and works by mapping quantum *operators* (matrices) onto a set of spherical functions, also known as spherical *droplets*.

### 1.2.1 Mapping of quantum operators onto spherical droplets

The visualization approach of DROPS representation relies on a bijective mapping between multi-qubit basis given by irreducible spherical tensor operators [11] and

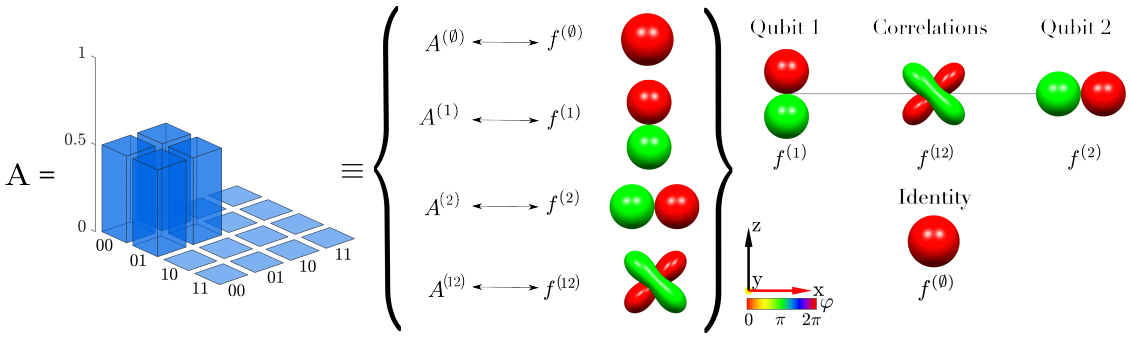


**Figure 1.2:** Skyscraper (left) and DROPS (right) visualization of a two-qubit quantum state $|\psi\rangle = \frac{1}{\sqrt{2}}(|00\rangle + |01\rangle)$ for which the density operator is represented by the operator $A = \frac{1}{4}(\mathbb{1}+\sigma_{1z}+\sigma_{2x}+\sigma_{1z}\sigma_{2x})$. The individual components $A^{(\ell)}$ of operator $A$ with label $\ell$ are mapped to spherical functions $f^{(\ell)}$ using a bijective mapping: $A = \sum_{\ell\in L} A^{(\ell)} \longleftrightarrow \bigcup_{\ell\in L} f^{(\ell)}$. The droplets are systematically combined in the rightmost panel, illustrating droplets corresponding to the state of the first qubit ($\sigma_{1z} = \sigma_z \otimes \mathbb{1}$), the second qubit ($\sigma_{2x} = \mathbb{1} \otimes \sigma_x$), correlations ($\sigma_{1z}\sigma_{2x} = \sigma_z \otimes \sigma_x$), and identity ($\mathbb{1}$) terms. In these three-dimensional polar plots of droplets $f^{(\ell)}(\beta, \alpha)$, the distance from the origin to a point on the surface represents the absolute value $|f^{(\ell)}(\beta, \alpha)|$, and the color indicates the phase $\varphi = \arg[f^{(\ell)}(\beta, \alpha)]$ as defined by the color bar.

multiple sets of spherical harmonics [12]. Although the DROPS representation can be applied to arbitrary finite-dimensional quantum systems [1, 13], here we focus on systems consisting of one or more qubits that are of particular interest in quantum information processing.

The method maps an arbitrary operator $A$ on a set of spherical functions $f^{(\ell)}$ which can easily be visualized, e.g., in the polar representation used here (or as colored spherical surfaces) [14]. Let us first consider an example of visualization shown in Fig. 1.2 and break it down into building block components. Panel (a) of Fig. 1.3 shows an example where the density operator $A$ of a two-qubit state is mapped to a set of four individual droplet functions $f^{(\ell)}$.

For systems consisting of up to two qubits, each of the individual droplet functions ($f^{(\emptyset)}$, $f^{(1)}$, $f^{(2)}$, and $f^{(12)}$) corresponds to one of the four possible (sub) sets of qubits: $\{\emptyset\}$ labels the empty set, $\{1\}$ labels the subset consisting only of the first qubit, $\{2\}$ labels the subset consisting only of the second qubit, and $\{12\}$ labels the set consisting of both qubits. Each subset is specified by a corresponding superscript label $\ell$. (For systems consisting of more than two qubits, specifying the (sub) systems of qubits is not sufficient, and additional selection criteria, such as permutation symmetry, are necessary to specify each droplet [1].) The method first decomposes any given operator $A$ as a sum of operators $A^{(\ell)}$, which are defined based on the criteria of the labels $\ell$ specified above. For example, the operator $A^{(1)}$ acts only on the first qubit, whereas, e.g., the operator $A^{(12)}$ acts on both the first and the second qubit, etc.

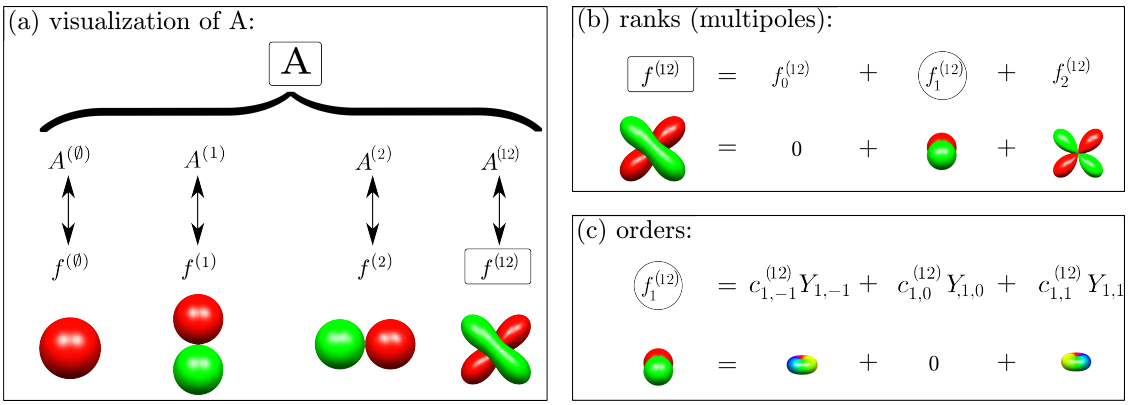


**Figure 1.3:** (a) For the two-qubit state $\frac{1}{\sqrt{2}}(|00\rangle + |01\rangle)$, the density operator is represented by $A = \frac{1}{4}(\mathbb{1} + \sigma_{1z} + \sigma_{2x} + \sigma_{1z}\sigma_{2x})$ and is visualized using multiple spherical functions $f^{(\ell)} = f^{(\ell)}(\beta, \alpha)$. The individual droplet operators $A^{(\ell)}$ of operator $A$ are mapped to the spherical droplet functions $f^{(\ell)}$. (b) $f^{(12)}$ (in a box) is decomposed into its contributions $f_j^{(12)}$ with $j \in \{0, 1, 2\}$. (c) $f_1^{(12)}$ (in a circle) is decomposed into spherical harmonics of order $m \in \{-1, 0, 1\}$.

As shown on the left side of the double-headed arrow in Eq. 1.15 (*vide infra*), each droplet operator $A^{(\ell)}$ can be expanded in an operator basis consisting of irreducible spherical tensor operator components $T_{jm}^{(\ell)}$ with expansion coefficients $c_{jm}^{(\ell)}$ [1, 13], where $j$ is the rank and $m$ is the order of the spherical tensor operators $T_{jm}^{(\ell)}$. Based on the well-known correspondence [15] between irreducible tensor operator components $T_{jm}$ and spherical harmonics $Y_{jm}$, a bijective mapping between the droplet operators $A^{(\ell)}$ and corresponding spherical droplet functions $f^{(\ell)}$ can be defined as

$$A^{(\ell)} = \sum_{j \in J(\ell)} \sum_{m=-j}^{j} c_{jm}^{(\ell)} T_{jm}^{(\ell)} \longleftrightarrow f^{(\ell)} = \sum_{j \in J(\ell)} \sum_{m=-j}^{j} c_{jm}^{(\ell)} Y_{jm}, \tag{1.15}$$

where identical expansion coefficients $c_{jm}^{(\ell)}$ are used on both sides of the double-headed arrow. Eq. 1.15 can be rewritten in the more compact form

$$A^{(\ell)} = \sum_{j \in J(\ell)} A_j^{(\ell)} \longleftrightarrow f^{(\ell)} = \sum_{j \in J(\ell)} f_j^{(\ell)}, \tag{1.16}$$

where we defined the rank $j$ droplet operators $A_j^{(\ell)}$ and droplet functions $f_j^{(\ell)}$ as

$$A_j^{(\ell)} = \sum_{m=-j}^{j} c_{jm}^{(\ell)} T_{jm}^{(\ell)} \quad \textit{and} \quad f_j^{(\ell)} = \sum_{m=-j}^{j} c_{jm}^{(\ell)} Y_{jm}. \tag{1.17}$$

As shown for the example of the droplet $f^{(12)}$ in panel (b) of Fig. 1.3, each spherical droplet function $f^{(\ell)}$ can be expressed as a sum of spherical functions $f_j^{(\ell)}$ with different

ranks $j$. For the case of $f^{(12)}$, the rank $j$ can be 0, 1, or 2. (Note that in the special case of the operator, $A$ represented in Fig. 1.3, the droplet function with rank 0 happens to vanish, i.e., $f_0^{(12)} = 0$.) This graphically illustrates the decomposition given on the right side of the double-headed arrow in Eq. 1.16.

The decomposition of $f_j^{(\ell)}$ in terms of the spherical harmonics $Y_{jm}$ with the expansion coefficients $c_{jm}^{(\ell)}$ (see right hand side of Eq. 1.17) is illustrated in panel (c) of Fig. 1.3 for the rank $j = 1$ spherical function $f_1^{(12)}$, which is decomposed in terms of the spherical harmonics $Y_{1,-1}$, $Y_{1,0}$, and $Y_{1,1}$ with the expansion coefficients $c_{1,-1} = \frac{i}{2}$, $c_{1,0} = 0$, and $Y_{1,1} = \frac{i}{2}$.

### 1.2.2 Visualization examples

**Single qubit state**

Let us consider a single qubit state $|\psi\rangle = |0\rangle$, the corresponding density matrix is given by

$$\rho = |0\rangle\langle 0| = \begin{pmatrix} 1 & 0 \\ 0 & 0 \end{pmatrix} = \frac{1}{2}(\mathbb{1} + \sigma_z). \tag{1.18}$$

Where $\sigma_z$ and $\mathbb{1}$ are the Pauli $z$ and identity matrices respectively. Using the basis transformation provided in Ref. [1], and summarized in Appendix A.1, the above density matrix can be written in terms of spherical tensor operators $T_{jm}^{(\ell)}$ as

$$\rho = \sqrt{\frac{1}{2}}(T_{00}^{(\emptyset)} + T_{10}^{(1)}). \tag{1.19}$$

Where the first of the two terms $T_{00}^{(\emptyset)}$ has rank $j = 0$, order $m = 0$, and linearity label $\ell = \emptyset$, which corresponds to an identity term in this terminology. The second term $T_{10}^{(1)}$ has rank $j = 1$, order $m = 0$, and label $\ell = 1$ which corresponds to a linear term. As described in Eq. 1.15, the spherical tensor operators $T_{jm}^{(\ell)}$ is mapped onto a complex spherical harmonics $Y_{jm}(\beta, \alpha) = r(\beta, \alpha)\exp(i\varphi(\beta, \alpha))$ to form droplet functions $f_j^{(\ell)}$ corresponding to a density matrix $\rho$:

$$f_0^{(\emptyset)}(\beta, \alpha) = \sqrt{\frac{1}{2}}(Y_{00}(\beta, \alpha)) \quad , \quad f_1^{(1)}(\beta, \alpha) = \sqrt{\frac{1}{2}}(Y_{10}(\beta, \alpha)). \tag{1.20}$$

These two droplet functions representing the density matrix corresponding to the quantum state $|\psi\rangle = |0\rangle$ are illustrated in Fig. 1.4.

In these three-dimensional polar plots of droplets $f^{(\ell)}(\beta, \alpha)$, the distance from the origin to a point on the surface is the absolute value $|f^{(\ell)}(\beta, \alpha)|$ and the color represents

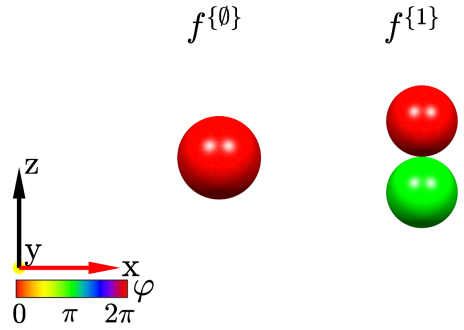


**Figure 1.4:** Droplets representing a density matrix corresponding to the quantum state $|\psi\rangle = |0\rangle$.

the phase $\varphi = \arg[f^{(\ell)}(\beta, \alpha)]$ as defined by the color bar. The direction of a droplet reflects the direction of a qubit in the Bloch sphere.

Different quantum operators can be similarly visualized by decomposing them into spherical tensor operators and mapping them to spherical harmonics. A few other examples of single-qubit state droplets are shown in Fig. 1.5.

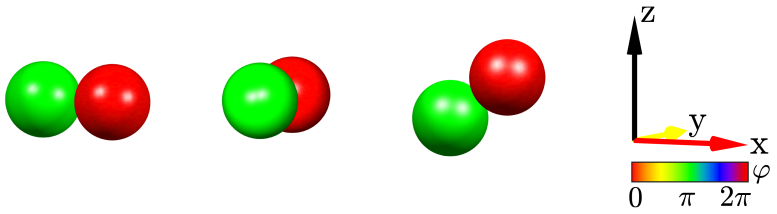


**Figure 1.5:** Droplets corresponding to quantum states: $\frac{|0\rangle+|1\rangle}{\sqrt{2}}$, $\frac{|0\rangle+i|1\rangle}{\sqrt{2}}$, and $0.885|0\rangle + 0.466|1\rangle$ from left to right. The rank $j = 0$ droplet $f_0^{(\emptyset)}$ representing the identity component of a density matrix is not shown here.

### Two qubit state

A visualization example for a two-qubit state $|\psi\rangle = \frac{1}{\sqrt{2}}(|00\rangle + |01\rangle)$ is presented in Fig. 1.2 and Fig. 1.3. Here, another two-qubit example of visualization is provided in Fig. 1.6 for the Bell state $|\Phi^+\rangle = \frac{1}{\sqrt{2}}(|00\rangle + |11\rangle)$. The corresponding density matrix is represented by the operator $A = \frac{1}{4}(\mathbb{1} + \sigma_{1x}\sigma_{2x} - \sigma_{1y}\sigma_{2y} + \sigma_{1z}\sigma_{2z})$. Since it is a maximally entangled state, the linear terms in the density matrix are zero, i.e., droplets $f^{(1)} = f^{(2)} = 0$, and only droplets $f^{(12)}$ and $f^{(\emptyset)}$ representing correlations and identity, respectively are non-zero.

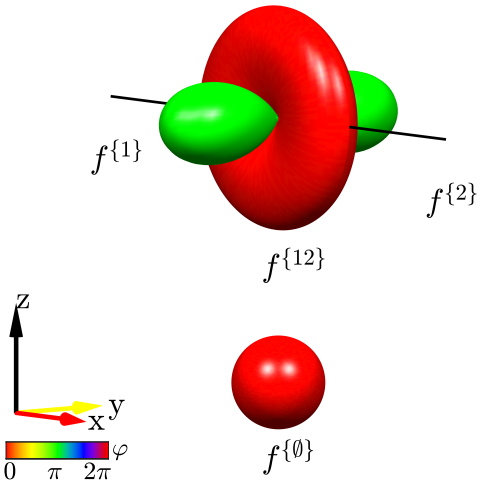


**Figure 1.6:** DROPS representation of the Bell state $|\Phi^+\rangle = \frac{1}{\sqrt{2}}(|00\rangle + |11\rangle)$.

### Single qubit gates

Similar to density matrices, quantum gates or processes (i.e., time-evolution operators) can also be visualized using DROPS representation. Let's take an example of Hadamard (H) gate, which can be decomposed in Pauli basis and spherical tensor ($T^{(\ell)}_{jm}$) basis as follows:

$$\mathrm{H} = \sqrt{\frac{1}{2}}\begin{pmatrix} 1 & 1 \\ 1 & -1 \end{pmatrix} = \sqrt{\frac{1}{2}}(\sigma_x + \sigma_z) = \sqrt{\frac{1}{2}}(T^{(1)}_{1-1} - T^{(1)}_{11} + \sqrt{2}T^{(1)}_{10}). \tag{1.21}$$

The corresponding droplet functions are:

$$f^{(\emptyset)}_0(\beta,\alpha) = 0 \quad , \quad f^{(1)}_1(\beta,\alpha) = \sqrt{\frac{1}{2}}(Y_{1-1}(\beta,\alpha) - Y_{11}(\beta,\alpha) + \sqrt{2}Y_{10}(\beta,\alpha)). \tag{1.22}$$

These droplet functions ($f^{(\emptyset)}_0 + f^{(1)}_1$) corresponding to the Hadamard gate, among other examples, are illustrated in Fig 1.7.

It is interesting to observe that the orientation of the process droplets aligns with the rotation axis for single-qubit quantum gates. For instance, in Fig. 1.7 (leftmost), the droplet corresponding to the NOT gate points parallel to the $x$ axis. In the cases of the NOT and Hadamard gates, the corresponding droplet functions displayed in Fig. 1.7 are real, resulting in only red (as $\varphi = \arg[f^{(\ell)}(\beta,\alpha)] = 0$ corresponds to positive real values) and green (as $\varphi = \arg[f^{(\ell)}(\beta,\alpha)] = \pi$ corresponds to negative real values) colors.

In contrast, the other droplets (related to $RY\left(\frac{3\pi}{2}\right)$, S and $\sqrt{\text{NOT}}$) possess non-zero imaginary components, and thus the colors representing the complex phase are not limited to red and green only. This characteristic is notable for rotation angles that are not integer multiples of $\pi$ as detailed in Ref. [16].

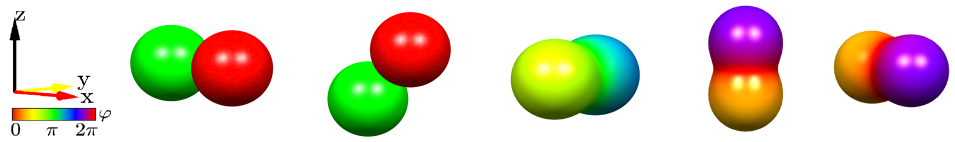


**Figure 1.7:** DROPS representation of different quantum gates (from left to right): NOT $= \begin{pmatrix} 0 & 1 \\ 1 & 0 \end{pmatrix}$, H $= \sqrt{\frac{1}{2}} \begin{pmatrix} 1 & 1 \\ 1 & -1 \end{pmatrix}$, $RY(\frac{3\pi}{2}) = \sqrt{\frac{1}{2}} \begin{pmatrix} -1 & -1 \\ 1 & -1 \end{pmatrix}$, S $= \sqrt{\frac{1}{2}} \begin{pmatrix} 1-i & 0 \\ 0 & 1+i \end{pmatrix}$, and $\sqrt{\text{NOT}} = \sqrt{\frac{1}{2}} \begin{pmatrix} 1 & -i \\ -i & 1 \end{pmatrix}$. The droplets shown here are plotted by combining rank $j = 0$ and $j = 1$ components, i.e., $f_0^{(\emptyset)} + f_1^{(1)}$.

## 1.3 Quantum tomography

Quantum tomography is a powerful methodology that aims to characterize and reconstruct the complete quantum state of a system. It plays a crucial role in experimental quantum information processing, offering a means to validate the success of quantum operations and gain insight into the quantum devices.

There are two primary categories of tomography: state tomography and process tomography. State tomography aims to reconstruct or tomograph the experimental density matrix of a quantum system by performing a set of measurements on an identically prepared system. Similarly, process tomography aims to characterize a quantum operation experimentally, which describes how a quantum state transforms under the influence of a particular operation or gate.

In addition to the standard methods for state tomography [3], alternative approaches include the classical shadow [17, 18], neural networks [19, 20], and the compressed sensing [21] approach to determine the state of a quantum system experimentally. Likewise, for process tomography, besides the standard protocol [3, 22], alternative methods such as unsupervised learning [23] and compressed sensing [24] are employed to reconstruct an unknown process from experimentally measured data.

This work focuses on methodologies to directly tomograph the shapes, i.e., droplets corresponding to quantum states and processes experimentally. This scanning-based tomography approach was developed to measure the droplets corresponding to quantum

states [14] and *known* unitary processes [16]. The procedures were implemented on an ensemble state-based NMR quantum information processor [25], where expectation values of observables can be directly measured [26]. In this work, we initially present the adaption of this approach to experimentally implement state and process tomography on a pure-state quantum computer. Subsequently, we extend this approach to *unknown* processes. In contrast to an NMR quantum information processor, on a pure-state quantum computer, expectation values are measured by many repetitions of projective measurements on individual quantum systems [3].

## 1.4 Outline of this thesis

This work provides a comprehensive description of Wigner tomography for both quantum states and known processes, along with its extension to address the previously missing aspect of Wigner tomography of unknown processes. This thesis is structured into three distinct parts: (i) Wigner quantum state tomography, (ii) Wigner tomography of known quantum processes, and (iii) Wigner tomography of unknown quantum processes. These sections encompass essential theoretical insights, detailed procedures for applying tomography techniques on pure-state quantum devices, and the experimental implementation for a limited number of qubits.

Chapter 2 Wigner quantum state tomography starts by introducing a scanning-based tomography approach in Sec. 2.1, which plays a significant role in this work. Sec. 2.2 introduces a generalized procedure for Wigner quantum state tomography. Sec. 2.3 presents a general method for estimating a density matrix from experimental tomographed droplets. In Sec. 2.4, we present an experimental framework for performing Wigner state tomography on a pure-state quantum computer for one and two-qubit systems. This section also shows the results of the experiments performed on IBM quantum systems. Sec. 2.5 presents a numerical study to compare the performance of different sampling schemes for state tomography along with the standard tomography [3] method. The Sec. 2.6 shows the usefulness of the DROPS tomography approach in visually identifying the type of error directly using an example. In Sec. 2.7, we introduce a Python package `DROPStomo` [27] for performing Wigner state tomography for single and two-qubit systems on a quantum computer along with an example code for a single-qubit system.

In Chapter 3, we start by presenting an approach to map a known unitary process matrix onto a density matrix to extend the scanning-based tomography approach in Sec. 3.1. Sec. 3.2 presents a generalized procedure for Wigner tomography of known processes. Similar to Wigner state tomography, in Sec. 3.3, we present a method for estimating unitary process matrices from the experimental droplets. In Sec. 3.4, we provide an experimental framework and present the results for a single qubit system. We provide an example code for the single qubit system for performing Wigner tomography

for known processes using a Python package `DROPStomo` [27].

In Chapter 4, we first present the existing circuit to map an unknown process matrix onto a density matrix and discuss the resulting blindspots in Sec. 4.1. Sec. 4.2 presents the extended circuit for mapping scaled versions of the unknown process matrices onto density matrices. In Sec. 4.3, we provide a generalized procedure for Wigner tomography of unknown processes. Sec. 4.4 provides an algorithm to reconstruct an unknown process from scaled process droplets. In this section, we explain the reconstruction algorithm using different examples and present a variant with optimization. In Sec. 4.5, we showcase the results of a numerical study for reconstruction algorithm with and without optimization. Sec. 4.6 provides an experimental procedure for performing tomography of unknown processes. We also discuss the experimental details, calibration circuits, and the results for a single qubit system performed on IBM systems in Sec. 4.6.

Chapter 5 presents an adaptive approach to performing Wigner process tomography and showcases it using multiple examples. We conclude in Chapter 6 by summarizing and discussing the theoretical and experimental aspects of the tomography approaches. Further technical details are deferred to the appendix. Appendix D presents the experimental design and details of the tomography of unknown processes on an ensemble-state-based NMR quantum information processor.

Chapter

# 2 Wigner Quantum State Tomography

This chapter is based on the manuscript [28] and delves into the theory of Wigner quantum state tomography. It explores a general experimental framework designed for pure-state near-term quantum devices and presents the outcomes of experiments conducted on IBM quantum devices.

In this chapter, our primary focus lies in experimentally scanning the Wigner representations of a density operator, as detailed in Sec. 1.2.2. This is a special case of quantum state tomography (QST), a vital tool in quantum computing and quantum information processing. Since the beginning of the field, extensive work has been carried out in this direction [29, 30, 31]. Recent studies use neural networks [19, 20], compressed sensing [21], and classical shadow approach [17, 18] to extract information about an unknown experimental state.

Here, we use a phase space [32] tomography approach, which is helpful in experimentally visualizing quantum operators in finite-dimensional quantum systems. These, in general, can be any quantum operators such as density operators, quantum processes (propagators), etc. The following section describes the scanning-based tomography approach, which is fundamental to the work presented in this thesis.

## 2.1 Scanning-based tomography approach

A general procedure for performing tomography in the context of Wigner representations using a scanning approach is described in the study [14] (see results 1 and 2). Here, we summarize this approach.

The following focuses without loss of generality on a system consisting of $N$ qubits. Consider a multi-qubit quantum operator $A$, which is also represented by a set of rank $j$ and label $\ell$ spherical droplet functions $f^{(\ell)} = \sum_{j \in J(\ell)} f_j^{(\ell)}(\beta, \alpha)$ as described in Sec. 1.2. To distinguish the size of different matrices, here we refer to operators as $A^{[N]}$, where $N$ is the number of qubits and therefore, the operator $A^{[N]}$ is represented by a matrix of size $2^N \times 2^N$. The main goal here is to experimentally reconstruct a spherical droplet function $f_j^{(\ell)}$ representing a quantum operator $A$ and this can be done by experimentally

estimating the scalar products of rotated axial tensor operators $T^{(\ell)[N]}_{j,\alpha\beta}$ with operator $A^{[N]}$, where

$$T^{(\ell)[N]}_{j,\alpha\beta} = R^{[N]}_{\alpha\beta}(T^{(\ell)}_{j0})^{[N]}(R^{[N]}_{\alpha\beta})^{\dagger}. \tag{2.1}$$

The term $(T^{(\ell)}_{j,\alpha\beta})^{[N]}$ is the rotated version of axial tensor operators $(T^{(\ell)}_{j0})^{[N]}$ of rank $j$ and order $m = 0$. The rotation operator is given by

$$R^{[N]}_{\alpha\beta} = \exp(-i\alpha F^{[N]}_z)\exp(-i\beta F^{[N]}_y) \tag{2.2}$$

where $F_z = \frac{1}{2}\sum_{k=1}^{N}\sigma^{[N]}_{kz}$ and $F_y = \frac{1}{2}\sum_{k=1}^{N}\sigma^{[N]}_{ky}$. The rotation operator $R^{[N]}_{\alpha\beta}$ corresponds to a rotation around the $y$ axis by polar angle $\beta \in [0, \pi]$ followed by rotation around the $z$ axis by azimuthal angle $\alpha \in [0, 2\pi)$. Here we use the shorthand notation $\sigma_{ka} = \mathbb{1} \otimes \cdots \otimes \mathbb{1} \otimes \sigma_a \otimes \mathbb{1} \otimes \cdots \otimes \mathbb{1}$, where $\sigma_a$ is located on the $k^{th}$ position and $a \in \{x, y, z\}$. For given angles $\beta$ and $\alpha$, droplet function $f^{(\ell)}_j$ can be calculated by

$$f^{(\ell)}_j(\beta, \alpha) = s_j \langle T^{(\ell)[N]}_{j,\alpha\beta} | A^{[N]} \rangle, \tag{2.3}$$

which can be equivalently written using a shorthand notation as

$$f^{(\ell)}_j(\beta, \alpha) = s_j \langle T^{(\ell)[N]}_{j,\alpha\beta} \rangle_{A^{[N]}}, \tag{2.4}$$

where, $s_j = \sqrt{(2j+1)/(4\pi)}$ and the scalar product $\langle T^{(\ell)[N]}_{j,\alpha\beta} | A^{[N]} \rangle$ is expressed as the expectation value of $T^{(\ell)[N]}_{j,\alpha\beta}$ for the density operator $A^{[N]}$:

$$\langle T^{(\ell)[N]}_{j,\alpha\beta} \rangle_{A^{[N]}} = \mathrm{tr}\Big\{(T^{(\ell)[N]}_{j,\alpha\beta})A^{[N]}\Big\}. \tag{2.5}$$

Note that axial tensor operators are Hermitian, i.e., $(T^{(\ell)[N]}_{j,\alpha\beta})^{\dagger} = (T^{(\ell)[N]}_{j,\alpha\beta})$ [14].

For the experimental reconstruction of droplet functions $f^{(\ell)}_j(\beta, \alpha)$ using the scanning approach, a multitude of choices for the set of sampling angles $\beta$ and $\alpha$ can be used. Fig. 2.1 illustrates three such sampling techniques: equiangular, REPULSION [33], and Lebedev [34]. For simplicity, in the demonstration experiments shown for state and known process tomography, an equiangular grid is used, and a numerical study using more sophisticated sampling techniques is presented and discussed in Sec. 2.5.

## 2.2 Procedure for Wigner quantum state tomography

In this section, we first present a generalized algorithm for performing Wigner quantum state tomography and then elaborate on each step individually. A general step-wise procedure (Fig. 2.2) to experimentally measure a spherical droplet function $f^{(\ell)}_j$ representing a density matrix $\rho^{[N]} = |\psi^{[N]}\rangle\langle\psi^{[N]}|$ is the following:

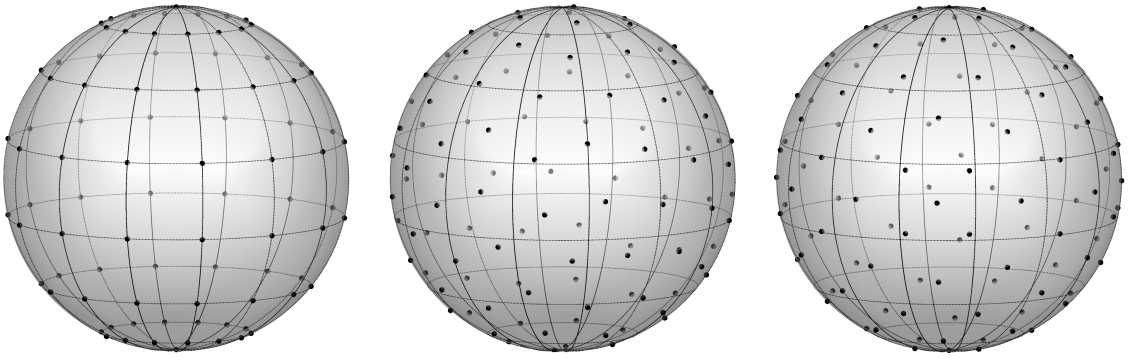

**Figure 2.1:** Examples of different sampling techniques on a sphere for scanning purpose (from left to right): equiangular, REPULSION [33], and Lebedev [34]. The grid points are plotted as dots on the sphere (faded dots represent grid points located at the rear side of the sphere). Expectation values are computed for specified points on the sphere to reconstruct the spherical functions representing a quantum operator $A$, as described in Eq. 2.4.

1. **Preparation ($\mathcal{P}$)**: Prepare the desired quantum state $\rho^{[N]}$ from a defined initial state $\rho_i^{[N]}$.
2. **Rotation ($\mathcal{R}$)**: Rotate the density operator $\rho^{[N]}$ inversely for scanning.
3. **Detection-associated rotations ($\mathcal{D}$)**: Apply local unitary operations to measure expectation values of Pauli operator components of axial tensor operators $T_{j0}^{(\ell)[N]}$ (see Table 2.1) that are not directly measurable.

These steps are repeated for the set of angles $\beta \in [0, \pi]$, $\alpha \in [0, 2\pi]$ and for different local unitary operators $u_n$ (*vide infra*), rank $j$, and label $\ell$ to experimentally scan the droplet functions $f_j^{(\ell)}$. In the rest of this section, we elaborate on each step of the presented algorithm.

*Step 1*: The first block of the algorithm, 'Preparation', can be achieved by applying unitary operations depending on the initial and the desired state.

*Step 2*: Since our operator of interest is a density matrix $\rho^{[N]}$, Eq. 2.4 takes the following form:

$$f_j^{(\ell)}(\beta, \alpha) = s_j \langle T_{j,\alpha\beta}^{(\ell)[N]} \rangle_{\rho^{[N]}}. \tag{2.6}$$

Instead of rotating the axial tensor operators $T_{j0}^{(\ell)[N]}$ as shown in Eq. 2.1, it is equivalent (and experimentally more convenient) to rotate the density matrix $\rho^{[N]}$ inversely, such that:

$$f_j^{(\ell)}(\beta, \alpha) = s_j \langle T_{j0}^{(\ell)[N]} \rangle_{\tilde{\rho}^{[N]}}, \tag{2.7}$$

where

$$\tilde{\rho}^{[N]} = (R_{\alpha\beta}^{[N]})^{-1} \rho^{[N]} R_{\alpha\beta}^{[N]}. \tag{2.8}$$

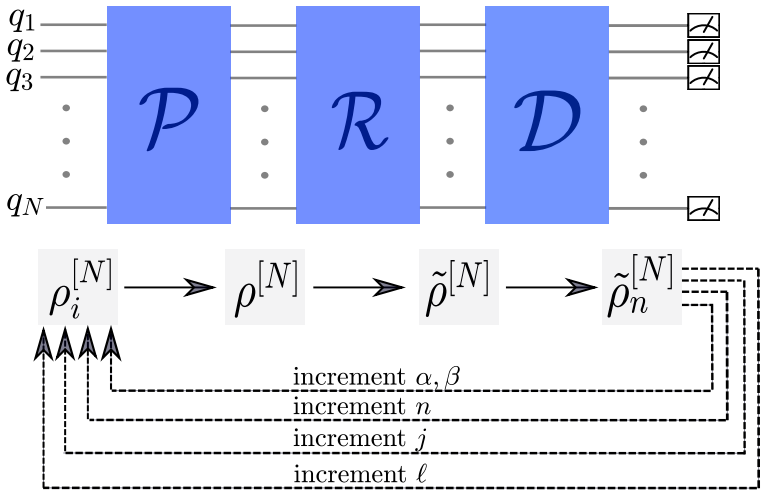


**Figure 2.2:** Schematic for the Wigner quantum state tomography algorithm. In general, the algorithm consists of three key blocks, namely Preparation ($\mathcal{P}$), Rotation ($\mathcal{R}$), and Detection-associated rotations ($\mathcal{D}$), which act on qubits $q_1, q_2, \ldots, q_N$ and are followed by projective measurements. The lower part of the figure shows the evolution of the density matrix after each block. The algorithm is repeated for all desired combinations of parameters.

The axial tensor operators ($T_{j0}^{(\ell)}$) are explicitly given in [1, 13] for systems consisting of up to six qubits. Table 2.1 summarizes the axial tensor operators for one and two-qubit systems.

*Step 3*: Depending on the number of qubits $N$ and rank $j$, the axial tensors $T_{j0}^{(\ell)}$ consist of different Pauli operators (see Table 2.1), but it might not be possible to measure these components directly depending on the specific quantum computing hardware. In a typical pure-state quantum computing device, the measurement is done along the $z$ axis, which implies that the directly measurable operators are: $\mathbb{1}$, $\sigma_{1z}$, $\sigma_{2z}$, and $\sigma_{1z}\sigma_{2z}$. In this case, measuring expectation values of non-directly measurable operators can be achieved with the help of local unitary operations $u_n$. For example, consider the expectation value $\langle T_{10}^{(12)} \rangle_{\tilde{\rho}(\beta,\alpha)}$ given by:

$$\begin{aligned} \langle T_{10}^{(12)} \rangle_{\tilde{\rho}(\beta,\alpha)} &= \frac{1}{2\sqrt{2}} \langle \sigma_{1x}\sigma_{2y} - \sigma_{1y}\sigma_{2x} \rangle_{\tilde{\rho}(\beta,\alpha)} \\ &= \frac{1}{2\sqrt{2}} \langle \sigma_{1x}\sigma_{2y} \rangle_{\tilde{\rho}(\beta,\alpha)} - \frac{1}{2\sqrt{2}} \langle \sigma_{1y}\sigma_{2x} \rangle_{\tilde{\rho}(\beta,\alpha)}. \end{aligned} \tag{2.9}$$

In the first term ($n = 1$) of Eq. 2.9, the expectation value $\langle \sigma_{1x}\sigma_{2y} \rangle_{\tilde{\rho}(\beta,\alpha)}$ needs to be determined. This can be achieved by measuring instead the expectation value

$$\langle \sigma_{1z}\sigma_{2z} \rangle_{\tilde{\rho}_1(\beta,\alpha)} = \langle \sigma_{1x}\sigma_{2y} \rangle_{\tilde{\rho}(\beta,\alpha)}, \tag{2.10}$$

where

$$\tilde{\rho}_1(\beta,\alpha) = u_1 \tilde{\rho}(\beta,\alpha) u_1^\dagger. \tag{2.11}$$

**Table 2.1:** Axial tensor operators $T_{j0}^{(\ell)}$ for one ($N = 1$) and two ($N = 2$) qubit systems.

| $N$ | $\ell$ | $j$ | $T_{j0}^{(\ell)}$ |
|---|---|---|---|
| 1 | $\emptyset$ | 0 | $T_{00}^{(\emptyset)} = \frac{1}{\sqrt{2}}(\mathbb{1})$ |
| | 1 | 1 | $T_{10}^{(1)} = \frac{1}{\sqrt{2}}(\sigma_z)$ |
| 2 | $\emptyset$ | 0 | $T_{00}^{(\emptyset)} = \frac{1}{2}\mathbb{1}$ |
| | 1 | 1 | $T_{10}^{(1)} = \frac{1}{2}(\sigma_{1z})$ |
| | 2 | 1 | $T_{10}^{(2)} = \frac{1}{2}(\sigma_{2z})$ |
| | 12 | 0 | $T_{00}^{(12)} = \frac{1}{2\sqrt{3}}(\sigma_{1x}\sigma_{2x} + \sigma_{1y}\sigma_{2y} + \sigma_{1z}\sigma_{2z})$ |
| | 12 | 1 | $T_{10}^{(12)} = \frac{1}{2\sqrt{2}}(\sigma_{1x}\sigma_{2y} - \sigma_{1y}\sigma_{2x})$ |
| | 12 | 2 | $T_{20}^{(12)} = \frac{-1}{2\sqrt{6}}(\sigma_{1x}\sigma_{2x} + \sigma_{1y}\sigma_{2y} - 2\sigma_{1z}\sigma_{2z})$ |

The density operator $\tilde{\rho}_1(\beta, \alpha)$ is obtained from $\tilde{\rho}(\beta, \alpha)$ by applying a $-\pi/2$ rotation around the $y$ axis (for bringing the $x$ axis to the $z$ axis) to the first qubit and a $\pi/2$ rotation around the $x$ axis (for bringing the $y$ axis to the $z$ axis) to the second qubit. This corresponds to the local unitary transformation $u_1 = \left((R_{0,\frac{\pi}{2}})^{-1} \otimes \mathbb{1}\right) \cdot (\mathbb{1} \otimes (R_{\frac{\pi}{2},\frac{\pi}{2}})^{-1})$.

Similarly, in the second term ($n = 2$) of Eq. 2.9, the expectation value $\langle \sigma_{1y}\sigma_{2x} \rangle_{\tilde{\rho}(\beta,\alpha)}$ needs to be determined. This can be achieved by measuring instead the expectation value

$$\langle \sigma_{1z}\sigma_{2z} \rangle_{\tilde{\rho}_2(\beta,\alpha)} = \langle \sigma_{1y}\sigma_{2x} \rangle_{\tilde{\rho}(\beta,\alpha)}, \tag{2.12}$$

where

$$\tilde{\rho}_2(\beta, \alpha) = u_2 \tilde{\rho}(\beta, \alpha) u_2^\dagger. \tag{2.13}$$

The density operator $\tilde{\rho}_2(\beta, \alpha)$ is obtained from $\tilde{\rho}(\beta, \alpha)$ by applying a $\pi/2$ rotation around the $x$ axis (for bringing the $y$ axis to the $z$ axis) to the first qubit and a $-\pi/2$ rotation around the $y$ axis (for bringing the $x$ axis to the $z$ axis) to the second qubit. This corresponds to the local unitary transformation $u_2 = ((R_{\frac{\pi}{2},\frac{\pi}{2}})^{-1} \otimes \mathbb{1}) \cdot (\mathbb{1} \otimes (R_{0,\frac{\pi}{2}})^{-1})$.

Overall, for $\ell = \{12\}$ and $j = 1$, the droplet function from Eq. 2.7 can be expressed as

$$\begin{aligned} f_1^{(12)}(\beta, \alpha) &= s_1 \langle T_{10}^{(12)} \rangle_{\tilde{\rho}(\beta,\alpha)} \\ &= \frac{s_1}{2\sqrt{2}} (\langle \sigma_{1z}\sigma_{2z} \rangle_{\tilde{\rho}_1(\beta,\alpha)} + \langle \sigma_{1z}\sigma_{2z} \rangle_{\tilde{\rho}_2(\beta,\alpha)}). \end{aligned} \tag{2.14}$$

Hence, only projective measurements along the $z$ axis are required.

## 2.3 Estimation of a density matrix from the droplet functions

In this section, we explain how the *matrix* form of a density operator can be estimated based on its experimentally measured DROPS representation. A general $N$-qubit density matrix [3] can be expressed in terms of Pauli operators as:

$$\rho^{[N]} = \sum_{a=0}^{3}\sum_{b=0}^{3}\cdots\sum_{g=0}^{3} r_{ab\ldots g}(\sigma_a \otimes \sigma_b \otimes \cdots \otimes \sigma_g), \tag{2.15}$$

where $\sigma_0$ is $\mathbb{1}$ (the 2×2 identity matrix), while $\sigma_1, \sigma_2$, and $\sigma_3$ are Pauli matrices $\sigma_x, \sigma_y$, and $\sigma_z$ respectively as defined in Eq. 1.11. The terms $r_{ab\ldots g}$ are real coefficients. Given the DROPS representation of a density operator, these coefficients can be computed by calculating the scalar product between basis droplets (ideally simulated without noise) and experimental droplets [14]. The basis droplets can be generated using the definitions provided in supplementary Sec. A.1 for one and two qubits.

The scalar product between two tensor operators can be approximated by the *discretized* scalar product between their droplet functions; see supplementary Sec. A.2. In the general case of a droplet $f_A$ with complex values $f_A(\theta_i, \phi_i)$ and another droplet $f_B$ with complex values $f_B(\theta_i, \phi_i)$ at the grid points, the scalar product or overlap between the two droplets is given by

$$r = \langle f_A | f_B \rangle = \sum_i \mathrm{w}_i f_A^*(\theta_i, \phi_i) f_B(\theta_i, \phi_i), \tag{2.16}$$

where $f_A^*(\theta_i, \phi_i)$ is the complex conjugate of $f_A(\theta_i, \phi_i)$ and $\mathrm{w}_i$ are the sampling weights. The sampling weights $\mathrm{w}_i$ reflect the relative surface area represented by each sample point, which depends on the distribution of the sample points on the sphere for a chosen sampling scheme (see Fig. 2.1 for different sampling choices on a sphere).

The sampling weights for an equiangular grid are discussed next, and the sampling weights for other sampling techniques, such as REPULSION and Lebedev, are available in [35] and [36], respectively.

#### Sampling weights for an equiangular grid

Considering an equiangular grid, where the sample points are equally distributed along polar ($\theta \in [0, \pi]$) angles as:

$$\theta_k = (k-1)d, \tag{2.17}$$

for $k = 1, 2, \ldots, M+1$. The points are distributed along azimuthal ($\phi \in [0, 2\pi)$) angles as:

$$\phi_l = (l-1)d, \tag{2.18}$$

for $l = 1, 2, \ldots, 2M$, where $M$ is a constant and $d = \dfrac{\pi}{M}$ is the angle increment. In this case, the part of Eq. 2.16 can be written in the form

$$\langle f_A | f_B \rangle = \sum_k \sum_l \mathrm{w}_{k,l}\ f_A^*(\theta_k, \phi_l) f_B(\theta_k, \phi_l). \tag{2.19}$$

At the north pole (where $k = 1$, corresponding to $\theta_1 = 0$) and at the south pole (where $k = M + 1$, corresponding to $\theta_{M+1} = \pi$), the weights are

$$\mathrm{w}_{1,l} = \mathrm{w}_{M+1,l} = \frac{1}{4M}\left[1 - \cos\left(\frac{d}{2}\right)\right]. \tag{2.20}$$

For all other sampling points, the weights are given by

$$\mathrm{w}_{k,l} = \frac{1}{4M}\left[\cos\left(\theta_k - \frac{d}{2}\right) - \cos\left(\theta_k + \frac{d}{2}\right)\right], \tag{2.21}$$

where $\theta_k$ is given in Eq. 2.17. In Eq. 2.20 and Eq. 2.21, $l$ runs from 1 to $2M$ and in Eq. 2.21, $k$ runs from 2 to $M$.

In the experiments, for redundancy, for each polar angle $\theta_k$, we measured not $2M$ but $2M + 1$ phase angles $\phi_l$ for sampling points, i.e., according to Eq. 2.18 the phase angle $\phi_{2M+1} = 2\pi$ and hence corresponds to $\phi_1 = 0$. This can be simply taken into account by scaling the weights by half for these specific points, i.e., $\mathrm{w}_{k,1} = \mathrm{w}_{k,2M+1} = \frac{1}{2}\mathrm{w}_{k,l}$, where $\mathrm{w}_{k,l}$ is given in Eq. 2.20 and Eq. 2.21.

**Fidelity estimation**

Based on the estimated experimental density operator $\rho^{[N]}$, the state fidelity ($\mathcal{F}_s$) [37] with which a desired state $\rho_t^{[N]}$ has been reached can be calculated using the normalized scalar product:

$$\mathcal{F}_s = \frac{\mathrm{tr}(\rho^{[N]}\rho_t^{[N]})}{\sqrt{\mathrm{tr}((\rho^{[N]})^2)\mathrm{tr}((\rho_t^{[N]})^2)}}. \tag{2.22}$$

The next section focuses on the experimental implementation of the presented algorithm for one and two-qubit systems and showcases the experimental results performed on IBM quantum devices.

## 2.4 Experimental implementation of quantum state tomography

This section explains how the Wigner quantum state tomography algorithm can be implemented on an experimental pure-state near-term quantum device. For concreteness, we will present the implementation using Qiskit [38], an open-source quantum development platform for simulations and experiments. Wigner state tomography can be used directly for one- and two-qubit systems using the Python-based software package `DROPStomo` [27], which is presented in Sec. 2.7.

### 2.4.1 One qubit

For a system consisting of one qubit ($N = 1$), there are only two possible values for the rank $j$: $j = 0$ for $\ell = \{\emptyset\}$ and $j = 1$ for $\ell = \{1\}$. Hence, the single qubit density matrix $\rho^{[1]}$ represented by spherical functions $f_0^{(\emptyset)}$ and $f_1^{(1)}$ can be reconstructed by measuring the expectation values from Eq. 2.7 as

$$\begin{aligned} f_0^{(\emptyset)}(\beta,\alpha) &= \sqrt{\frac{1}{4\pi}}\langle (T_{00}^{(\emptyset)})^{[1]}\rangle_{\tilde{\rho}^{[1]}}, \\ f_1^{(1)}(\beta,\alpha) &= \sqrt{\frac{3}{4\pi}}\langle (T_{10}^{(1)})^{[1]}\rangle_{\tilde{\rho}^{[1]}}. \end{aligned} \tag{2.23}$$

Substituting the explicit form of the tensor operators $T_{00}^{(\emptyset)}$ and $T_{10}^{(1)}$ from Table 2.1 gives

$$\begin{aligned} f_0^{(\emptyset)}(\beta,\alpha) &= \sqrt{\frac{1}{8\pi}}\langle \mathbb{1}\rangle_{\tilde{\rho}^{[1]}}, \\ f_1^{(1)}(\beta,\alpha) &= \sqrt{\frac{3}{8\pi}}\langle \sigma_z\rangle_{\tilde{\rho}^{[1]}}, \end{aligned} \tag{2.24}$$

where $\mathbb{1}$ is the $2 \times 2$ identity matrix. The required expectation values can be computed directly on a pure-state quantum computer based on the outcome probabilities $p_0$ and $p_1$ corresponding to state $|0\rangle$ and state $|1\rangle$ respectively:

$$\begin{aligned} \langle \mathbb{1}\rangle &= p_0 + p_1 \\ \langle \sigma_z\rangle &= p_0 - p_1. \end{aligned} \tag{2.25}$$

The probabilities $p_0$ and $p_1$ can be experimentally measured by repeating an experiment multiple times, where the number of repetitions is also referred to as number of shots $N_s$. We discuss this in more detail in supplementary Sec. A.3. In the considered case, the detection-associated rotation ($\mathcal{D}$) step is not required.

The probabilities $p_0$ and $p_1$ required for computing the expectation values for droplets $f_0^{(\emptyset)}$ and $f_1^{(1)}$ can be measured in the same experiment; hence the algorithm presented in Fig. 2.2 does not require to be repeated for rank $j$ and label $\ell$.

The Fig. 2.3 explicitly shows the quantum circuit for performing state tomography of a qubit in state $|\psi\rangle = \frac{1}{\sqrt{2}}(|0\rangle + |1\rangle)$. As shown in Fig. 2.3, this state is prepared from the initial state $|\psi_i\rangle = |0\rangle$ using $\mathrm{U}_3(\frac{\pi}{2}, 0, 0)$ (alternately, a Hadamard gate could be used). This preparation step is followed by the rotation step $\mathcal{R}$ which is implemented by $\mathrm{U}_3^{-1}(\beta,\alpha,0) = \mathrm{U}_3(-\beta, 0, -\alpha)$. In the experiments, we used 8 values of polar ($\beta$) angles and 15 values of azimuthal ($\alpha$) angles. Therefore, the quantum circuit is repeated 120 ($=8 \cdot 15$) times.

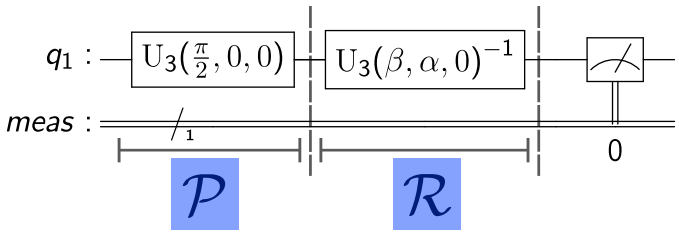


**Figure 2.3:** Quantum circuit for Wigner state tomography corresponding to a state $|\psi\rangle = \frac{|0\rangle+|1\rangle}{\sqrt{2}}$. The first and second block of the circuit corresponds to the Preparation ($\mathcal{P}$) and Rotation ($\mathcal{R}$) step of state tomography from left to right. The superposition state is prepared from the initial state $|\psi\rangle_i = |0\rangle$. The $U_3$ gate used in the circuit is discussed in Sec. 1.1.3.

Fig. 2.4 shows the plots of corresponding simulated and experimental expectation values $\langle\sigma_z\rangle_{\tilde{\rho}^{[1]}}$ for all combinations of scanning angles $\beta_k = (k-1)\frac{\pi}{7}$ and $\alpha_l = (l-1)\frac{\pi}{7}$, where $k = 1, 2, \ldots, 8$ and $l = 1, 2, \ldots, 15$. Fig. 2.4a shows the ideal expectation values with no noise, Fig. 2.4b shows the simulated expectation values with shot noise for number of shots $N_s = 8192$, and Fig. 2.4c shows the experimental expectation values for the same number of shots $N_s$. The rank $j = 0$ ($f_0^{(\emptyset)}$) component is a sphere (indicating the identity droplet) which is not shown here. The right panel of Fig. 2.4 shows the corresponding tomographed droplets.

The single-qubit state tomography experimental results are illustrated in Fig. 2.5 for different quantum states. To avoid redundancy, Fig. 2.5 only shows the plot of the rank $j = 1$ droplets, as the rank $j = 0$ droplet is a sphere of radius $\sqrt{1/(8\pi)}$ in the single-qubit case. These experiments were performed on the `ibm_lagos` device with $N_s = 8192$ shots per sample point, i.e., for every combination of angles $\beta$ and $\alpha$. The simulated droplets shown in the results are plotted with high resolution, whereas the experimental droplets are interpolated between the experimentally determined sampling points using the Matlab *surf* function [39].

Based on the experimentally tomographed droplet functions $f_0^{(\emptyset)}$ and $f_1^{(1)}$, the corresponding density matrix can be estimated as discussed in Sec. 2.3. For a single qubit, the density matrix can be expressed in terms of Pauli operators as

$$\rho^{[1]} = \sum_{k=0}^{3} r_k \sigma_k. \tag{2.26}$$

To compute the coefficient $r_0$, a scalar product is calculated using Eq. 2.16 between the ideal basis droplet ($f_{\sigma_0}$) and the experimentally tomographed $f_0^{(\emptyset)}$ droplet:

$$r_0 = \langle f_{\sigma_0} | f_0^{(\emptyset)} \rangle. \tag{2.27}$$

To compute the remaining coefficients $r_k$ for $k \in \{1, 2, 3\}$, we calculate the scalar product between all ideal basis droplets with label $\ell = 1$, rank $j = 1$, and the experimentally

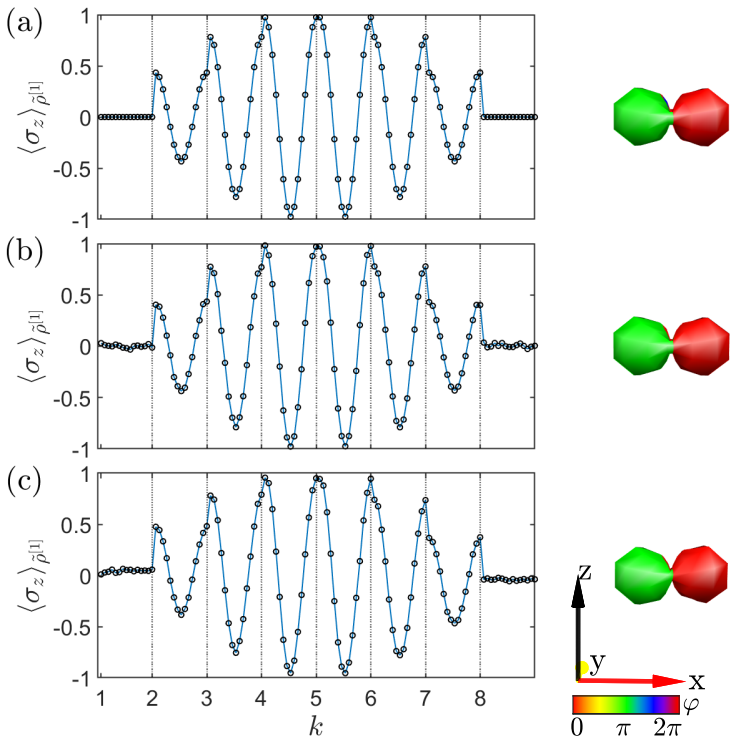


**Figure 2.4:** The expectation values and the droplet corresponding to the rank $j = 1$ component of a quantum state $|\psi\rangle = \frac{1}{\sqrt{2}}(|0\rangle + |1\rangle)$: (a) ideal simulation, (b) simulation with shot noise, and (c) experimental data. The expectation values are calculated for the combinations of eight polar angles $\beta_k = (k-1)\frac{\pi}{7}$ and fifteen azimuthal angles $\alpha_l = (l-1)\frac{\pi}{7}$, where $k = 1, 2, \ldots, 8$ and $l = 1, 2, \ldots, 15$. In the figure, for each value of $k$ the azimuthal counter $l$ is incremented from 1 to 15.

tomographed rank $j = 1$ droplet $f_1^{(1)}$:

$$r_k = \langle f_{\sigma_k} | f_1^{(1)} \rangle. \tag{2.28}$$

The ideal basis droplet functions $f_{\sigma_k}$ are provided in supplementary Sec. A.1. Hence, by calculating these overlap coefficients $r_k$, an estimate of the density matrix can be obtained using Eq. 2.26. Table 2.2 provides experimental state tomography fidelities computed using Eq. 2.22 for different states considered in Fig. 2.5. The standard deviations given in Table 2.2 were estimated by conducting the experiment three times with the state $|\psi_t\rangle = 0.885|0\rangle + 0.466|1\rangle$, for a reference.

### 2.4.2 Two qubits

For a two-qubit system ($N = 2$), there are four possible labels $\ell$, and based on these labels, there are different ranks $j$ as shown in Table 2.1. Therefore, for a two-qubit system, the Wigner quantum state tomography requires measuring the following

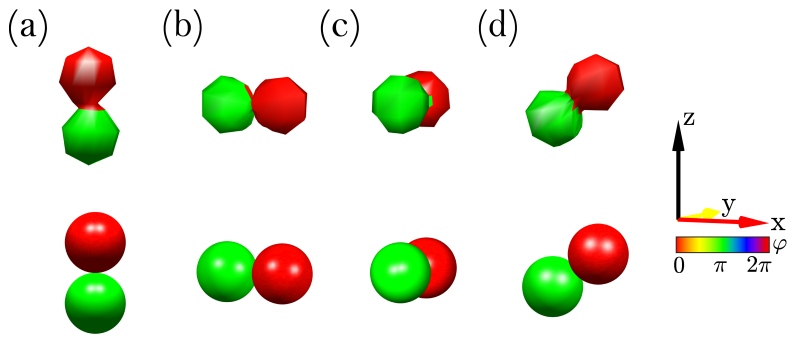


**Figure 2.5:** Experimentally tomographed (top panel) and simulated (lower panel) droplets corresponding to quantum states: (a) $|0\rangle$, (b) $\frac{|0\rangle+|1\rangle}{\sqrt{2}}$, (c) $\frac{|0\rangle+i|1\rangle}{\sqrt{2}}$, and (d) $0.885|0\rangle + 0.466|1\rangle$.

**Table 2.2:** Experimental state tomography fidelities ($\mathcal{F}_s$) corresponding to the desired single-qubit quantum states $|\psi_t\rangle$, see Fig. 2.5.

| $\|\psi_t\rangle$ | $\mathcal{F}_s$ |
|---|---|
| $\frac{1}{\sqrt{2}}(\|0\rangle + \|1\rangle)$ | $0.9991 \pm 1 \times 10^{-3}$ |
| $\|0\rangle$ | $0.9991 \pm 1 \times 10^{-3}$ |
| $\frac{1}{\sqrt{2}}(\|0\rangle + i\|1\rangle)$ | $0.9992 \pm 1 \times 10^{-3}$ |
| $0.885\|0\rangle + 0.466\|1\rangle$ | $0.9990 \pm 1 \times 10^{-3}$ |

spherical droplets $f_j^{(\ell)}$:

$$\begin{aligned} f_0^{(\emptyset)}(\beta,\alpha) &= \sqrt{\frac{1}{4\pi}}\,\langle (T_{00}^{(\emptyset)})^{[2]}\rangle_{\tilde{\rho}^{[2]}} \\ &= \frac{1}{4\sqrt{\pi}}\,\langle \mathbb{1}\rangle_{\tilde{\rho}^{[2]}} \end{aligned} \tag{2.29}$$

for the identity droplet ($j = 0$, and $\ell = \emptyset$), here $\mathbb{1}$ is the 4×4 identity matrix. For droplets of rank $j = 1$, for each qubit (with labels $\ell = 1$ and $\ell = 2$) we have:

$$\begin{aligned} f_1^{(1)}(\beta,\alpha) &= \sqrt{\frac{3}{4\pi}}\,\langle (T_{10}^{(1)})^{[2]}\rangle_{\tilde{\rho}^{[2]}} \\ &= \frac{1}{4}\sqrt{\frac{3}{\pi}}\,\langle \sigma_{1z}\rangle_{\tilde{\rho}^{[2]}}\,, \end{aligned} \tag{2.30}$$

$$\begin{aligned} f_1^{(2)}(\beta,\alpha) &= \sqrt{\frac{3}{4\pi}}\,\langle (T_{10}^{(2)})^{[2]}\rangle_{\tilde{\rho}^{[2]}} \\ &= \frac{1}{4}\sqrt{\frac{3}{\pi}}\,\langle \sigma_{2z}\rangle_{\tilde{\rho}^{[2]}}\,. \end{aligned} \tag{2.31}$$

For bilinear terms with label $\ell = 12$, we have

$$\begin{aligned} f_0^{(12)}(\beta,\alpha) &= \sqrt{\frac{1}{4\pi}}\,\langle (T_{00}^{(12)})^{[2]}\rangle_{\tilde{\rho}^{[2]}} \\ &= \frac{1}{4\sqrt{3\pi}}\,\langle (\sigma_{1x}\sigma_{2x}+\sigma_{1y}\sigma_{2y}+\sigma_{1z}\sigma_{2z})\rangle_{\tilde{\rho}^{[2]}} \end{aligned} \tag{2.32}$$

for rank $j = 0$,

$$\begin{aligned} f_1^{(12)}(\beta,\alpha) &= \sqrt{\frac{3}{4\pi}}\,\langle (T_{10}^{(12)})^{[2]}\rangle_{\tilde{\rho}^{[2]}} \\ &= \frac{1}{4}\sqrt{\frac{3}{2\pi}}\,\langle (\sigma_{1x}\sigma_{2y}-\sigma_{1y}\sigma_{2x})\rangle_{\tilde{\rho}^{[2]}} \end{aligned} \tag{2.33}$$

for rank $j = 1$, and

$$\begin{aligned} f_2^{(12)}(\beta,\alpha) &= \sqrt{\frac{5}{4\pi}}\,\langle (T_{20}^{(12)})^{[2]}\rangle_{\tilde{\rho}^{[2]}} \\ &= \frac{1}{4}\sqrt{\frac{5}{6\pi}}\,\langle (-\sigma_{1x}\sigma_{2x}-\sigma_{1y}\sigma_{2y}+2\sigma_{1z}\sigma_{2z})\rangle_{\tilde{\rho}^{[2]}} \end{aligned} \tag{2.34}$$

for rank $j = 2$. Different Pauli operator expectation values are required in Eq. 2.29 to Eq. 2.34, and some of them are not directly measurable. In this case, the last block of the algorithm detection-associated rotations ($\mathcal{D}$) is used, which is explained with an example in Sec. 2.2. The rotations required for step $\mathcal{D}$ can be implemented in terms of local $U_3$ gates (see Eq. 1.9). Similar to the computation of expectation values of linear terms in Eq. 2.25, the expectation values of bilinear terms can be computed by combining the outcome probabilities:

$$\begin{aligned} \langle \mathbb{1}\rangle &= p_{00}+p_{01}+p_{10}+p_{11}, \\ \langle \sigma_{1z}\sigma_{2z}\rangle &= p_{00}-p_{01}-p_{10}+p_{11}, \end{aligned} \tag{2.35}$$

where $p_{ab}$ for $a, b \in \{0, 1\}$ is the probability corresponding to state $|ab\rangle$. Please refer to supplementary Sec. A.3 for more information.

The Fig. 2.6 explicitly show the quantum circuits for a Wigner state tomography of a Bell state $|\psi\rangle = \frac{1}{\sqrt{2}}(|00\rangle + |11\rangle)$, as an example. The different circuits in the figure are used for calculating the different expectation values, which are then combined to form a particular droplet function $f_j^{(\ell)}$. Hence, for a two-qubit Wigner quantum state tomography, a maximum of five quantum circuits are required, which are repeated for all combinations of values of the angles $\beta$ and $\alpha$. Two-qubit state tomography results are illustrated in Fig. 2.7 and Fig. 2.8 for a Bell state $|\psi\rangle = \frac{1}{\sqrt{2}}(|00\rangle + |11\rangle)$ and state $|\psi\rangle = \frac{1}{\sqrt{2}}(|00\rangle + |01\rangle)$, respectively. The experiments were performed on a seven qubit

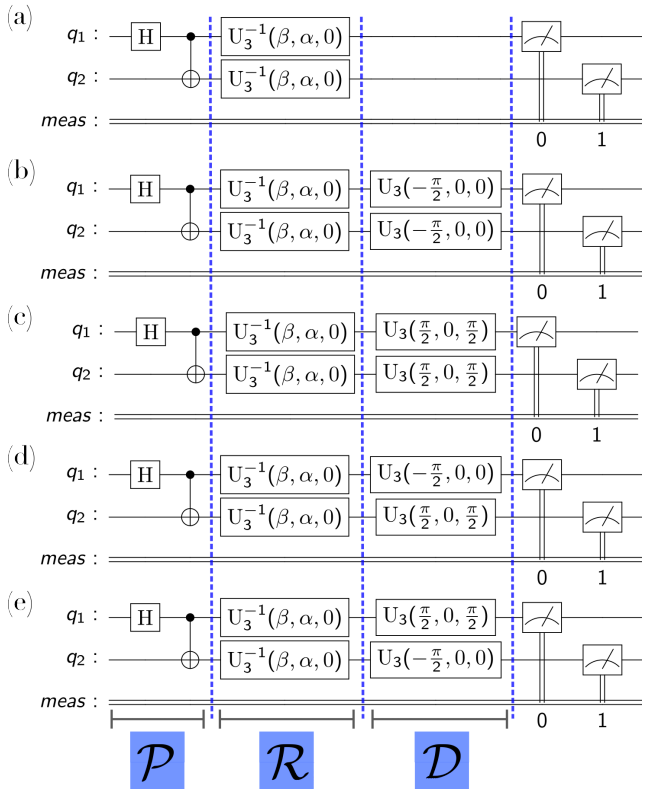


**Figure 2.6:** Quantum circuit set for a two-qubit Wigner state tomography of a Bell state $|\psi\rangle = \frac{1}{\sqrt{2}}(|00\rangle + |11\rangle)$. The Bell state is prepared from the initial state $|\psi\rangle_i = |00\rangle$ by applying the Hadamard (H) gate on $q_1$ followed by a controlled-NOT gate. The three blocks Preparation ($\mathcal{P}$), Rotation ($\mathcal{R}$), and Detection-associated rotations ($\mathcal{D}$) are shown here. Circuit (a) provides the expectation values for the operators $\mathbb{1}, \sigma_{1z}, \sigma_{2z}$, and $\sigma_{1z}\sigma_{2z}$. Similarly, circuits (b), (c), (d), and (e) provide the expectation values for the operators $\sigma_{1x}\sigma_{2x}, \sigma_{1y}\sigma_{2y}, \sigma_{1x}\sigma_{2y}$, and $\sigma_{1y}\sigma_{2x}$, respectively.

`ibm_lagos` device with $N_s = 8192$ shots per sample point, i.e., for eight polar angles $\beta_k = (k-1)\frac{\pi}{7}$ and fifteen azimuthal angles $\alpha_l = (l-1)\frac{\pi}{7}$, where $k = 1, 2, \ldots, 8$ and $l = 1, 2, \ldots, 15$. The experimental example shown in Figs. 2.7 and 2.8 are plotted with the same resolution. The high-resolution simulated figures for these two examples are provided in Fig.1.6 and Fig.1.2.

Similar to the one-qubit system, the density matrix based on the experimentally tomographed droplets can be estimated. The density matrix for a two-qubit system can be expressed in terms of Pauli operators as

$$\rho^{[2]} = \sum_{k=0}^{3}\sum_{l=0}^{3} r_{kl}(\sigma_k \otimes \sigma_l). \tag{2.36}$$

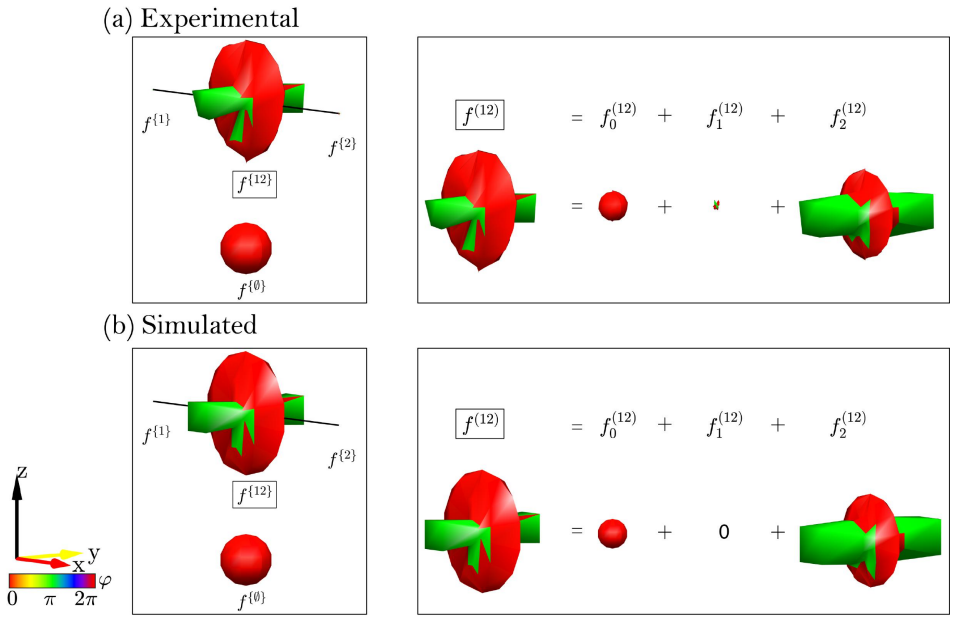


**Figure 2.7:** DROPS representation of the Bell state $|\psi\rangle = \frac{1}{\sqrt{2}}(|00\rangle + |11\rangle)$. Experimentally, tomographed droplets are shown in the upper panel (a), whereas the simulated droplets are shown in the lower panel (b). The right panels show the respective bilinear droplet function $f^{(12)}$ (box) decomposed into its multipole contribution $f_j^{(12)}$ with $j \in \{0, 1, 2\}$. Here, both experimental and simulated droplets are plotted with the same resolution.

The terms $r_{kl}$ with $k, l \in \{0, 1, 2, 3\}$ are real coefficients and can be calculated by computing the scalar product between the droplet functions as shown in Eq. 2.16. To compute $r_{00}$, the scalar product is calculated between the simulated ideal basis droplet $(f_{\sigma_0})$ with label $\ell = \emptyset$, rank $j = 0$ and the experimentally tomographed droplet function $f_0^{(\emptyset)}$ as,

$$r_{00} = \langle f_{\sigma_0} | f_0^{(\emptyset)} \rangle. \tag{2.37}$$

To calculate the coefficients $r_{k0}$ for $k \in \{1, 2, 3\}$ the scalar product is computed between all ideal basis droplets with label $\ell = 1$, rank $j = 1$ and the experimentally tomographed droplet $f_1^{(1)}$:

$$r_{k0} = \langle f_{\sigma_{1k}} | f_1^{(1)} \rangle. \tag{2.38}$$

Similarly, the coefficients $r_{0l}$ for $l \in \{1, 2, 3\}$ can be computed by calculating the scalar product between the ideal basis droplets of label $\ell = 2$, rank $j = 1$ and experimentally tomographed droplet $f_1^{(2)}$:

$$r_{0l} = \langle f_{\sigma_{2l}} | f_1^{(2)} \rangle. \tag{2.39}$$

The remaining bilinear coefficients $r_{kl}$ for $k, l \in \{1, 2, 3\}$ can be calculated by computing the scalar product between the ideal bilinear basis droplets $f_{\sigma_{1k}\sigma_{2l}}$ with the sum of the

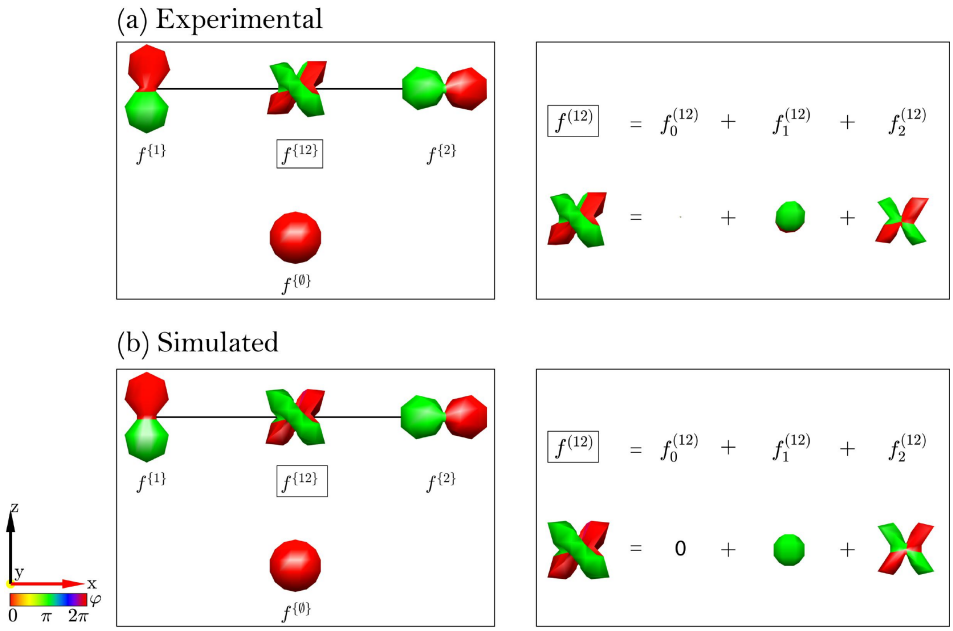


**Figure 2.8:** DROPS representation of the state $|\psi\rangle = \frac{1}{\sqrt{2}}(|00\rangle + |01\rangle)$. Experimentally, tomographed droplets are shown in the upper panel (a), whereas the simulated droplets are shown in the lower panel (b). Right panels show the respective bilinear droplet function $f^{(12)}$ (box) decomposed into its multipole contribution $f_j^{(12)}$ with $j \in \{0, 1, 2\}$. Here, both experimental and simulated droplets are plotted with the same resolution.

experimentally tomographed droplets $f_0^{(12)}$, $f_1^{(12)}$, and $f_2^{(12)}$:

$$r_{kl} = \langle f_{\sigma_{1k}\sigma_{2l}} | f_0^{(12)} + f_1^{(12)} + f_2^{(12)} \rangle. \tag{2.40}$$

The ideal basis droplets are provided in the supplementary Sec. A.1. Hence, by calculating these coefficients for every value of $k$ and $l$, a density matrix can be estimated using Eq. 2.36 and the state fidelity ($\mathcal{F}_s$) can be computed using Eq. 2.22. Table 2.3 provides the experimental state fidelities of two-qubit examples. The standard deviation given in Table 2.3 was estimated by conducting the experiment three times with the state $|\psi_t\rangle = \frac{1}{\sqrt{2}}(|00\rangle + |11\rangle)$, for a reference.

**Table 2.3:** Experimental state fidelities ($\mathcal{F}_s$) corresponding to desired two-qubit quantum state $|\psi_t\rangle$, see Fig. 2.7 and Fig. 2.8.

| $\lvert\psi_t\rangle$ | $\mathcal{F}_s$ |
|---|---|
| $\frac{1}{\sqrt{2}}(\lvert00\rangle + \lvert11\rangle)$ | $0.9989 \pm 1 \times 10^{-3}$ |
| $\frac{1}{\sqrt{2}}(\lvert00\rangle + \lvert01\rangle)$ | $0.9982 \pm 1 \times 10^{-3}$ |

## 2.5 Scanning using different sampling schemes: a numerical study

Scanning is a key step in the Wigner tomography approach, and hence, choosing a suitable sampling scheme on a sphere is important. This is a topic of interest in the general field of signal processing [40], and a number of different sampling schemes have been proposed in the literature.

In the ideal case of negligible experimental noise, only a small number of sampling points would be necessary to determine the correct expansion coefficients of spherical harmonics as each droplet function is band-limited [41, 16]. An advantage of using a large number of sampling points is to obtain a direct view of the experimentally measured droplet shapes without additional signal processing steps, such as the extraction of expansion coefficients of spherical harmonics or the estimation of the matrix representation of an operator. Note that a larger number of sampling points $N_p$ does not necessarily entail an increase in the total number of experiments $N_{tot}(= N_p \cdot N_s)$ because the number $N_s$ of shots per sampling point can also be adapted to each sampling scheme. In the following, we compare the performance of different sampling schemes for (approximately) the same total number of shots ($N_{tot}$) given by the product of the number of sampling points ($N_p$) and the number of shots per sampling point ($N_s$).

In Fig. 2.9, the mean fidelity ($\bar{\mathcal{F}}_s$) of the tomographed state is shown as a function of the total number of experiments for the Lebedev [34], REPULSION [33], and SHREWD [42] sampling schemes along with the simple equiangular grid and the standard tomography method [3, 43]. For more detailed information, including standard deviations, see supplementary Sec. A.4. For this study, only the noise due to a limited number of shots is considered. In the simple case of an equiangular grid [44, 45] of eight polar angles $\beta \in \{0, \frac{\pi}{7}, \dots \pi\}$ and fifteen azimuthal angles $\alpha \in \{0, \frac{2\pi}{14}, \dots 2\pi\}$ as shown in Fig. 2.1a, the total number of grid points is 120. For Lebedev, REPULSION, and SHREWD, 110 grid points were used. Since the number of sampling points in both cases is similar, for simplicity, the same number of shots per sampling point was chosen. In contrast, for the standard tomography method, only three measurement settings are required for the case of a single-qubit. The forty-fold decrease in the number of sampling points was compensated by correspondingly increasing the number of shots per measurement setting by a factor of 40 to arrive at the same total number of shots $N_{tot}$ as in the previous cases.

In the supplementary Sec. A.4, the result of the same study for the state $|\psi\rangle = \frac{1}{\sqrt{2}}(|0\rangle + |1\rangle)$ is provided. The plots indicate that the mean fidelity differs depending on sampling techniques and tomography methods and also show that an equiangular grid is not an optimal choice, as expected because the density of grid points is higher near the poles compared to the equator of the sphere. This numerical study is expected to help make an informed choice of the sampling scheme for quantum computing applications

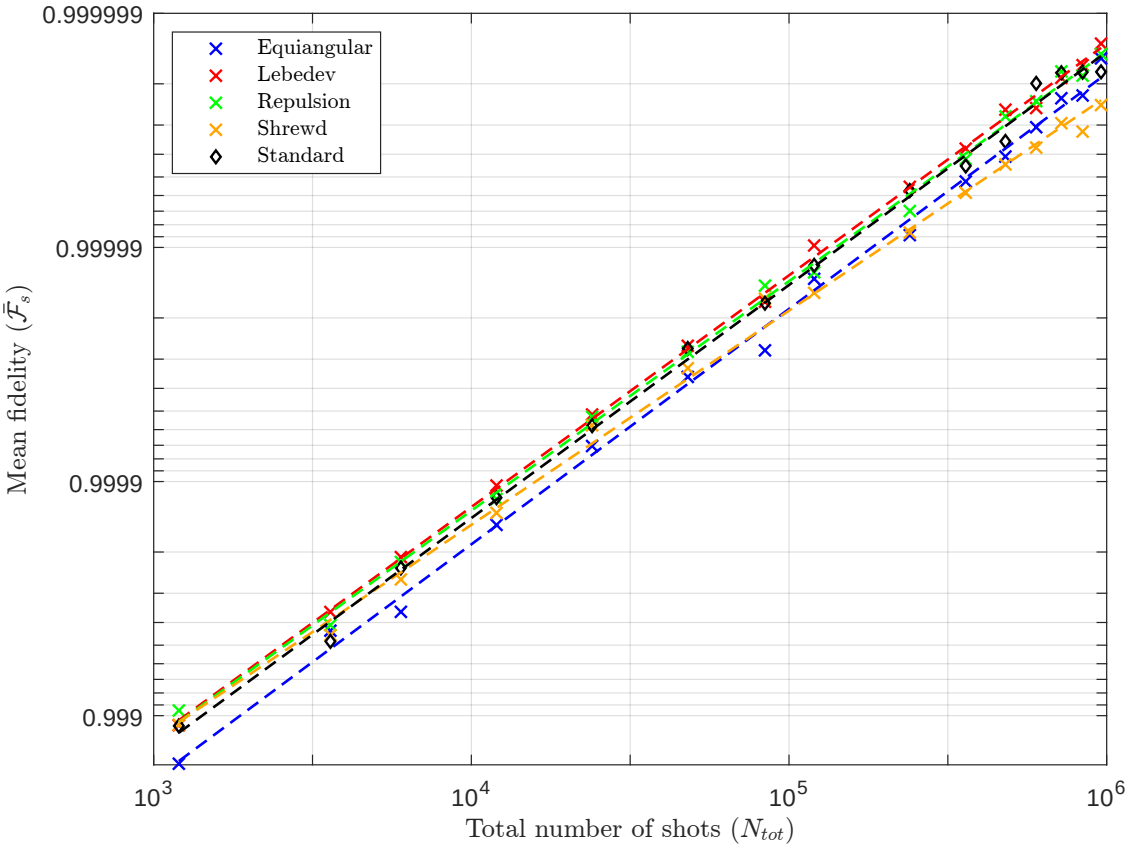


**Figure 2.9:** Plot of the mean fidelity ($\bar{\mathcal{F}}_s$) as a function of the total number of shots ($N_{tot}$) for different sampling techniques and for the standard state tomography method applied to the quantum state $|\psi\rangle = (-0.69 - 0.098i)|0\rangle + (0.66 + 0.30i)|1\rangle$. The mean fidelity is calculated by repeating the simulation 100 times for each data point. In the simulation, only the noise due to a limited number of shots is considered. The corresponding plot with standard deviation is available in supplementary Sec. A.4.

in which an estimate of the quantum state with high precision is required.

The Spinach [35] software was used to generate angles and weights for the REPULSION and the SHREWD sampling techniques. For standard state tomography, the maximum-likelihood estimation (MLE) method [46, 47] was used on the numerical data to estimate a valid quantum state. We used the corresponding qiskit [38] classes to perform the standard state tomography based on the MLE method.

## 2.6 DROPS for visualizing errors

Quantum devices are prone to different kinds of errors both in the implementation of desired states and quantum gates. Here, we focus on the example of rotation errors,

e.g., due to errors in pulse calibrations, etc. Visualizing or identifying these errors directly is useful in quantum information processing. Here, we show how the DROPS representation is helpful to achieve this. As described in the caption of Fig. 1.2, the radius (distance from the origin to a point on the sphere) of a droplet represents the absolute value of a droplet function $f^{(\ell)}$, and color represents the phase $\varphi = \arg[f^{(\ell)}]$. In addition, the direction of a qubit droplet reflects the direction of the Bloch vector for quantum states (see: Fig. 1.2 and 2.5) and of the rotation axis for single-qubit quantum gates (see Fig. 3.3).

As an example, we show the experimental tomography result of the desired quantum state $|\psi\rangle = \frac{1}{\sqrt{2}}(|00\rangle + |01\rangle)$ with some error in the state preparation. We deliberately introduce an additional rotation of $\mathrm{U}_3(\pi/12, 0, 0)$ on qubit $q_1$, and $\mathrm{U}_3(\pi/9, \pi/12, 0)$ on qubit $q_2$ in the preparation step. Fig. 2.10a shows that these kinds of errors are directly visible in the DROPS representations as misalignment of the linear droplet functions $f^{(1)}$ and $f^{(2)}$ compared to the ideal (without rotation errors) case shown in Fig 2.10b and experimental tomography results of the case without rotation error shown in Fig. 2.8.

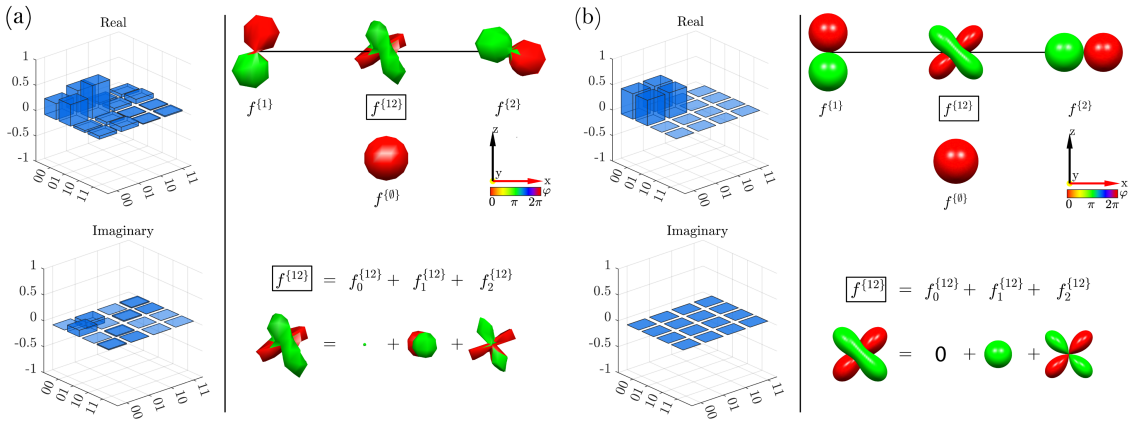


**Figure 2.10:** Standard skyscraper and DROPS plot for the state $|\psi\rangle = \frac{1}{\sqrt{2}}(|00\rangle + |01\rangle)$. (a) Experimental tomographed droplets with additional rotations of $\mathrm{U}_3(\pi/12, 0, 0)$ on qubit $q_1$, and $\mathrm{U}_3(\pi/9, \pi/12, 0)$ on qubit $q_2$ in the preparation step. (b) Simulated droplet plots with no rotation error. The DROPS plot (right block of (a) and (b)) also shows the respective bilinear droplet function $f^{(12)}$ (box) decomposed into its multipole contribution $f_j^{(12)}$ with $j \in \{0, 1, 2\}$.

Note that such a direct physical interpretation of the error terms is not possible using the standard skyscraper visualization [3] of the density matrix (left block of Fig. 2.10a). In Fig. 2.11, we also show the droplet plots from a different perspective to emphasize the misalignment errors.

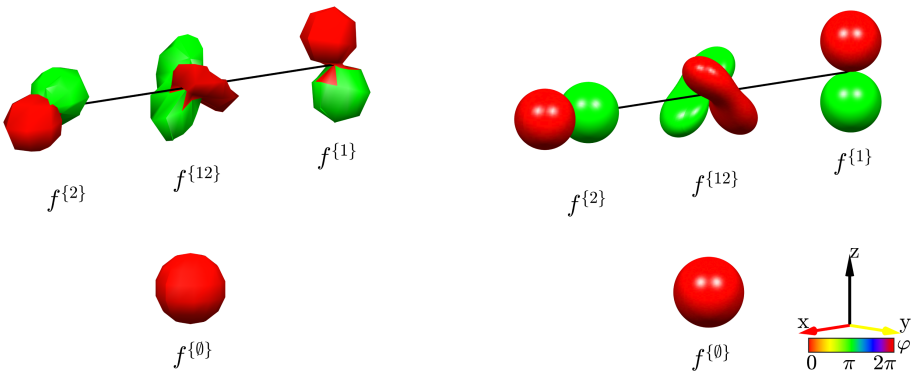


**Figure 2.11:** Different perspective of the DROPS visualization of the density matrix corresponding to the state $|\psi\rangle = \frac{1}{\sqrt{2}}(|00\rangle + |01\rangle)$: experimental tomographed droplets with rotation errors (left) and simulated droplets with no errors (right).

## 2.7 Performing WQST on near-term quantum devices using DROPStomo

DROPStomo [27] is a Python-based software package for performing Wigner Quantum State Tomography (WQST) for one two-qubit system and process tomography for a single-qubit system. With DROPStomo, users can simulate (on a simulator or on quantum hardware) and analyze the tomographed droplets interactively. The package is based on the Qiskit framework [38]. However, it is straightforward to adapt it to other frameworks. The packages DROPStomo can be installed using the following command:

```
# install the package
pip install DROPStomo
```

Here, we give a code snippet for performing Wigner state tomography for a one-qubit superposition state $|\psi\rangle = \frac{|0\rangle+|1\rangle}{\sqrt{2}}$ for eight polar angles $\beta \in [0, \pi]$ and fifteen azimuthal angles $\alpha \in [0, 2\pi]$.

```
# import the required modules
from DROPStomo import WQST1Q
from DROPStomo import WQST2Q

# ***Input***
# Gate for state preparation.
Up = U3Gate(theta=pi/2, phi=0, lam=0)
# Resolution for scanning
res_beta= 8
res_alpha = 15
# Define target density matrix
rho = np.matrix([[0.5,0.5],[0.5,0.5]])
```

```
13
14 # Prepare quantum circuits for tomography
15 circ_q = WQST1Q.WQST_1Q_circuits(res_beta,Up)
16
17 # Provide a simulator or a quantum hardware. For example:
18 simulator = Aer.get_backend('qasm_simulator')
19
20 # Run quantum circuits on a simulator or on a quantum hardware.
21 WQST1Q.WQST_1Q_runner(res_theta,circuits=circ_q,device=simulator,shots
       =8192,inter=1,rhoT=rho)
22
23 # ***Output***
24 # Experimental tomographed droplets (non-interactive, if inter=0 and
       interactive, if inter=1).
25 # Experimental expectation values.
26 # Experimental density matrix with state fidelity.
```

We provide the extended tutorial codes for one and two-qubit Wigner state tomography in our repository [27].

Chapter

# 3 Wigner Tomography of Known Quantum Processes

This chapter is based on the manuscript [28] and presents an approach to perform Wigner tomography of *known* quantum processes.

In general, process tomography [3, 22, 48] is a technique used to characterize a quantum process based on experimentally measured data. Here, we focus on directly scanning the droplets corresponding to a unitary process. The considered unitary processes could refer to quantum gates, time evolution operators, or pulse sequences. Leveraging the theory and experimental framework established for ensemble-state-based NMR quantum computers in Ref. [16], we adapt this methodology to the domain of pure-state quantum computing. This chapter delves into the method for mapping a known unitary process matrix onto a density matrix, the procedure of Wigner tomography of *known* quantum processes, a general experimental framework tailored for pure-state near-term quantum devices, and the results of experiments conducted on IBM quantum devices.

As detailed in Sec. 2.2, if the operator of interest is a quantum state or a density operator represented by $\rho^{[N]}$, the spherical droplet function $f_j^{(\ell)}(\beta, \alpha)$ can be measured experimentally. In the case of process tomography, our operator of interest is an $N$ qubit quantum process $U^{[N]}$. It is possible to scan the Wigner representation of an arbitrary operator $A^{[N]}$ if it can be experimentally mapped onto the density operator. The following section presents the algorithm for Wigner process tomography based on a method to map a unitary process matrix onto a density matrix [16, 49, 50, 51].

## 3.1 Mapping of a known unitary process matrix onto a density matrix

Mapping a general *unitary* matrix $U^{[N]}$ onto a *Hermitian* density matrix of the same dimension is not possible. Here, we double the dimension of the density matrix by using an additional ancilla qubit $q_0$ and by a controlled process $cU^{[N+1]}$ operation we inscribe the unitary $U^{[N]}$ (and its adjoint $(U^{[N]})^\dagger$) in an off-diagonal block of the density matrix $\rho^{[N+1]}$ as shown below. Under $cU^{[N+1]}$, the unitary $U^{[N]}$ acts only on the target qubits $q_1, \ldots, q_N$ if the control qubit $q_0$ is in state $|1\rangle$. The corresponding

matrix representation of the controlled process $cU^{[N+1]}$ is

$$cU^{[N+1]} = \begin{pmatrix} \mathbb{1}^{[N]} & 0^{[N]} \\ 0^{[N]} & U^{[N]} \end{pmatrix}, \tag{3.1}$$

where the top diagonal block corresponds to a $2^N \times 2^N$ dimensional identity matrix $\mathbb{1}^{[N]}$ and the lower diagonal block is the unitary $U^{[N]}$. The off-diagonal blocks are $2^N \times 2^N$ dimensional zero matrices.

As shown in [16] for ensemble quantum processors, $U^{[N]}$ can be mapped onto the density operator $\rho^{[N+1]}$ by preparing the ancilla (control) qubit $q_0$ in the superposition state $\frac{1}{\sqrt{2}}(|0\rangle + |1\rangle)$ and the remaining system qubits $q_1, \ldots, q_N$ in the maximally mixed state. Hence, the prepared density operator is

$$\begin{aligned} \rho_0^{[N+1]} &= \frac{1}{2}\Big(|0\rangle + |1\rangle\Big)\Big(\langle 0| + \langle 1|\Big) \otimes \frac{1}{2^N}(\mathbb{1}^{[N]}), \\ &= \frac{1}{2^{N+1}} \begin{pmatrix} \mathbb{1}^{[N]} & \mathbb{1}^{[N]} \\ \mathbb{1}^{[N]} & \mathbb{1}^{[N]} \end{pmatrix} \end{aligned} \tag{3.2}$$

and the density operator after application of $cU^{[N+1]}$ is

$$\rho_U^{[N+1]} = cU^{[N+1]} \rho_0^{[N+1]} (cU^{[N+1]})^\dagger, \tag{3.3}$$

which can be rewritten in block matrix form as

$$\rho_U^{[N+1]} = \frac{1}{2^{(N+1)}} \begin{pmatrix} \mathbb{1}^{[N]} & (U^{[N]})^\dagger \\ U^{[N]} & \mathbb{1}^{[N]} \end{pmatrix}. \tag{3.4}$$

Using this approach, the unitary $U^{[N]}$ is now imprinted onto the density operator $\rho^{[N+1]}$ of the augmented system. Since the experimental implementation of a controlled process $cU^{[N+1]}$ requires the knowledge of $U^{[N]}$, this version of Wigner process tomography described here is in general only applicable for *known* processes [16]. The next section describes the procedure for performing Wigner process tomography experimentally.

## 3.2 Procedure for Wigner quantum process tomography

In this section, we first present a generalized algorithm for performing process tomography and then explain each step individually for pure-state quantum processors. A droplet function $f_j^{(\ell)}$ representing an $N$ qubit quantum process $U^{[N]}$ can be experimentally measured using the following steps (see Fig. 3.1):

1. **Preparation ($\mathcal{P}$)**: Prepare ancilla qubit $q_0$ in the superposition state $\frac{1}{\sqrt{2}}(|0\rangle + |1\rangle)$ and effectively create the maximally mixed state of the system qubits $q_1, \ldots, q_N$ by temporal averaging.

2. **Mapping ($\mathcal{M}$)**: Implement the $cU^{[N+1]}$ operation to map the process $U^{[N]}$ onto $\rho_U^{[N+1]}$.

3. **Rotation ($\mathcal{R}$)**: Rotate the system qubits $q_1, \ldots, q_N$ inversely for scanning.

4. **Detection-associated rotations ($\mathcal{D}$)**: Apply local unitary operations to measure required expectation values of Pauli operator components of axial tensor operators $T_{j0}^{(\ell)[N]}$ (see Table 2.1) that are not directly measurable.

These four steps are repeated for a set of angles $\beta \in [0, \pi]$ and $\alpha \in [0, 2\pi]$ and for different $n$, rank $j$ and labels $\ell$ to calculate the droplet function $f_j^{(\ell)}(\beta, \alpha)$. The next part elaborates on each step individually.

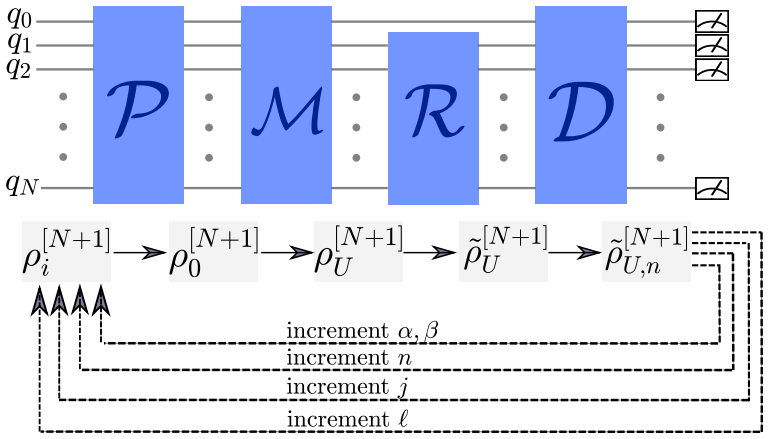


**Figure 3.1:** Schematic of the presented Wigner tomography algorithm for known unitary processes. The algorithm consists of four key blocks, namely Preparation ($\mathcal{P}$), Mapping ($\mathcal{M}$), Rotation ($\mathcal{R}$), and Detection-associated rotations ($\mathcal{D}$) followed by measurements. The rotation ($\mathcal{R}$) block acts only on system qubits $q_1, \ldots, q_N$, whereas all the other three blocks act on all the qubits $q_0, q_1, \ldots, q_N$. The lower part of the figure shows the evolution of the density matrix after each block. The algorithm is repeated for all desired combinations of parameters.

*Step 1*: The algorithm starts with the initial state $\rho_i = |0 \ldots 0\rangle\langle 0 \ldots 0|$. The state $\rho_0$ (Eq. 3.2) is prepared by applying a Hadamard gate to qubit $q_0$ to achieve an equal superposition. The maximally mixed state of qubits $q_1, \ldots, q_N$ is created by temporally averaging experiments for all the possible computational basis states by applying appropriate local NOT gates (see supplementary Sec. B.2). We discuss this in detail for a single-qubit system in Sec. 3.4.1.

*Step 2*: The operation $cU^{[N+1]}$ used for mapping can be experimentally implemented by decomposing it into elementary gates [52] or using pulse-level control methods [53, 54].

*Step 3*: Since our operator of interest is an $N$-qubit unitary process matrix $U^{[N]}$, Eq. 2.4 takes the form

$$f_j^{(\ell)}(\beta,\alpha) = s_j \langle T_{j,\alpha\beta}^{(\ell)[N]} | U^{[N]} \rangle. \tag{3.5}$$

As shown in supplementary Sec. B.1, Eq. 3.5 can be rewritten as

$$f_j^{(\ell)}(\beta,\alpha) = s_j \langle \sigma^+ \otimes T_{j,\alpha\beta}^{(\ell)[N]} \rangle_{\rho_U^{[N+1]}}, \tag{3.6}$$

Similarly as in state tomography (Sec. 2.2), instead of rotating the axial tensor operator $T_{j0}^{(\ell)[N]}$, we equivalently rotate the density matrix of the system qubits $q_1, \ldots, q_N$ inversely, such that:

$$f_j^{(\ell)}(\beta,\alpha) = s_j \langle \sigma^+ \otimes T_{j0}^{(\ell)[N]} \rangle_{\tilde{\rho}_U^{[N+1]}}, \tag{3.7}$$

where

$$\tilde{\rho}_U^{[N+1]} = (R_{\alpha\beta}^{[N+1]})^{-1} \rho_U^{[N+1]} R_{\alpha\beta}^{[N+1]}, \tag{3.8}$$

and $R_{\alpha\beta}^{[N+1]} = \mathbb{1}^{[1]} \otimes R_{\alpha\beta}^{[N]}$ which corresponds to the rotation of only the system qubits $q_1, \ldots, q_N$ for scanning. Using the relation $\sigma^+ = \frac{1}{2}(\sigma_x + i\sigma_y)$, Eq. 3.7 can be rewritten in terms of Pauli operators as:

$$f_j^{(\ell)}(\beta,\alpha) = \frac{s_j}{2}\Big( \langle \sigma_x \otimes T_{j0}^{(\ell)[N]} \rangle_{\tilde{\rho}_U^{[N+1]}} + i \langle \sigma_y \otimes T_{j0}^{(\ell)[N]} \rangle_{\tilde{\rho}_U^{[N+1]}} \Big). \tag{3.9}$$

*Step 4*: In analogy to the case of Wigner state tomography presented in Sec. 2.2, the expectation values of Pauli operators, which are not directly observable, can be measured with the help of local unitary operations $u_n$ (detection-associated rotations).

## 3.3 Estimation of unitary process matrices from droplet functions

Similar to the estimation of density matrices in the case of Wigner state tomography 2.3, unitary process matrices can also be estimated from the experimentally tomographed droplets. A general $N$-qubit unitary process matrix can be expressed in terms of Pauli operators [3] as:

$$U^{[N]} = \sum_{a=0}^{3} \sum_{b=0}^{3} \cdots \sum_{g=0}^{3} c_{ab\ldots g} (\sigma_a \otimes \sigma_b \otimes \cdots \otimes \sigma_g), \tag{3.10}$$

where $\sigma_0$ is a 2×2 identity ($\mathbb{1}$) matrix, while $\sigma_1$, $\sigma_2$ and $\sigma_3$ are the standard Pauli matrices $\sigma_x$, $\sigma_y$ and $\sigma_z$, respectively. The complex coefficients $c_{ab\ldots g}$ can be computed by calculating the scalar product between basis droplets (ideally simulated without noise) and experimental droplets, as shown in Eq. 2.16. The basis droplets can be generated using the definitions provided in supplementary Sec. A.1. Based on the estimated process matrix $U^{[N]}$, the process tomography fidelity $\mathcal{F}_U$ [55] can be calculated using the relation:

$$\mathcal{F}_U = \frac{|\mathrm{tr}(U^{[N]}(U_t^{[N]})^\dagger)|}{2^N}, \tag{3.11}$$

where $U_t^{[N]}$ is an $N$ qubit target unitary process matrix.

The next section focuses on the experimental implementation of the presented algorithm for a single-qubit system and showcases the results of the experiments performed on IBM quantum devices.

## 3.4 Experimental implementation of Wigner process tomography

This section describes the approach to implementing the above-mentioned Wigner process tomography on experimental quantum devices. Here, we present the simulated and experimental process tomography results performed on IBM quantum devices for a pure state of an individual quantum system. The quantum circuits provided here are general and can be directly adapted to other near-term quantum devices. The Wigner process tomography can be directly implemented using the Python-based software package `DROPStomo` [27] for a single-qubit system, which is presented in Sec. 3.5.

### 3.4.1 Single qubit system

For the Wigner process tomography of a single-qubit ($N = 1$) system, the total number of qubits required is two ($q_0$ and $q_1$), where $q_0$ is an ancilla qubit and $q_1$ is the system qubit. For a single-qubit system, the possible values of rank $j$ are (c.f. Table 2.1): $j = 0$ for label $\ell = \emptyset$, and $j = 1$ for label $\ell = 1$. Hence, a single-qubit unitary process is represented by the spherical functions $f_0^{(\emptyset)}$ and $f_1^{(1)}$, which can be calculated based on the measured expectation values of Eq. 3.9 as:

$$\begin{aligned} f_0^{(\emptyset)}(\beta,\alpha) &= \frac{1}{2}\sqrt{\frac{1}{4\pi}}\Big(\langle\sigma_x \otimes T_{00}^{(\emptyset)[1]}\rangle_{\tilde{\rho}_U^{[2]}} + i\langle\sigma_y \otimes T_{00}^{(\emptyset)[1]}\rangle_{\tilde{\rho}_U^{[2]}}\Big) \\ f_1^{(1)}(\beta,\alpha) &= \frac{1}{2}\sqrt{\frac{3}{4\pi}}\Big(\langle\sigma_x \otimes T_{10}^{(1)[1]}\rangle_{\tilde{\rho}_U^{[2]}} + i\langle\sigma_y \otimes T_{10}^{(1)[1]}\rangle_{\tilde{\rho}_U^{[2]}}\Big). \end{aligned} \tag{3.12}$$

Substituting the explicit form of the tensor operators $T_{00}^{(\emptyset)}$ and $T_{10}^{(1)}$ from Table 2.1 gives

$$\begin{aligned} f_0^{(\emptyset)}(\beta,\alpha) &= \frac{1}{4}\sqrt{\frac{1}{2\pi}}\Big(\langle\sigma_{0x}\rangle_{\tilde{\rho}_U^{[2]}} + i\langle\sigma_{0y}\rangle_{\tilde{\rho}_U^{[2]}}\Big) \\ f_1^{(1)}(\beta,\alpha) &= \frac{1}{4}\sqrt{\frac{3}{2\pi}}\Big(\langle\sigma_{0x}\sigma_{1z}\rangle_{\tilde{\rho}_U^{[2]}} + i\langle\sigma_{0y}\sigma_{1z}\rangle_{\tilde{\rho}_U^{[2]}}\Big). \end{aligned} \tag{3.13}$$

We first focus on the preparation step ($\mathcal{P}$) of the algorithm, i.e., preparing qubits $q_0$ and $q_1$ in a state whose density matrix corresponds to Eq. 3.2 for $N = 1$. The preparation of the ancilla qubit $q_0$ in the superposition state can be achieved straightforwardly by applying the Hadamard (H) gate on $q_0$. The qubit $q_1$ requires to be prepared in a *maximally* mixed state. Preparing it directly in pure-state quantum computing is not

possible. We use the *temporal* averaging approach [56, 57], where the experiment is repeated for the set of computational basis states, and the average of measurement outcomes is computed. For example, in the case of a single qubit ($N = 1$), the maximally mixed state $\rho_{mm}^{[1]}$ can be realized by simply repeating the experiment twice (one experiment with the pure state $|0\rangle$ and another experiment with the pure state $|1\rangle$) and averaging the measurement results:

$$\rho_{mm}^{[1]} = \frac{1}{2}\mathbb{1}^{[1]} = \frac{1}{2}\begin{pmatrix} 1 & 0 \\ 0 & 1 \end{pmatrix} = \frac{1}{2}|0\rangle\langle 0| + \frac{1}{2}|1\rangle\langle 1|. \tag{3.14}$$

More information on temporal averaging, alternative methods, and the proof of expressing the expectation value of mixed states as an average of expectation values of pure states is detailed in supplementary Sec. B.2.

Interestingly, temporal averaging was initially introduced in quantum information processing to mimic experiments of a pure state by averaging expectation values obtained by measuring a set of experiments on (partially) mixed states of an ensemble quantum processor [56]. In contrast, here experiments on the maximally mixed state of the system qubits $q_1, \ldots, q_N$ are mimicked by averaging expectation values obtained by measuring a set of experiments with pure states.

As an example, Fig. 3.2 shows the set of quantum circuits for process tomography where the unitary operator of interest is the Hadamard gate (H). Hence, a controlled Hadamard gate is applied in the mapping step ($\mathcal{M}$) of each experiment in (a)-(d). After the preparation step $\mathcal{P}$, the system qubit $q_1$ is in state $|0\rangle$ for circuits (a) and (c), whereas it is switched to $|1\rangle$ by applying a NOT (X) gate on $q_1$ in circuits (b) and (d). The (temporally) averaged expectation values of experiments (a) and (b) provide $\langle\sigma_{0x}\rangle$ (and also $\langle\sigma_{0x}\sigma_{1z}\rangle$). Similarly, the (temporally) averaged expectation values of experiments (c) and (d) provide $\langle\sigma_{0y}\rangle$ (and also $\langle\sigma_{0y}\sigma_{1z}\rangle$).

Using Eq. 3.13, these expectation values can be combined to obtain the droplet functions $f_0^{(\emptyset)}$ and $f_1^{(1)}$, see Fig 3.3 (first column) for the combined ($f = f_0^{(\emptyset)} + f_1^{(1)}$) droplets and Fig. 3.4 (first row) for the individual droplets $f_0^{(\emptyset)}$ and $f_1^{(1)}$. Fig. 3.3 also shows experimental droplets of the NOT (X) gate and the process corresponding to a rotation of $\frac{3\pi}{2}$ around the $y$ axis. The separate droplets $f_0^{(\emptyset)}$ and $f_1^{(1)}$ for rank $j = 0$ and $j = 1$ are provided in the Fig. 3.4.

The experiments were performed on a seven qubit `ibm_lagos` device with $N_s = 8192$ shots per sample point, i.e., for eight polar angles $\beta_k = (k-1)\frac{\pi}{7}$ and fifteen azimuthal angles $\alpha_l = (l-1)\frac{\pi}{7}$, where $k = 1, 2, \ldots, 8$ and $l = 1, 2, \ldots, 15$.

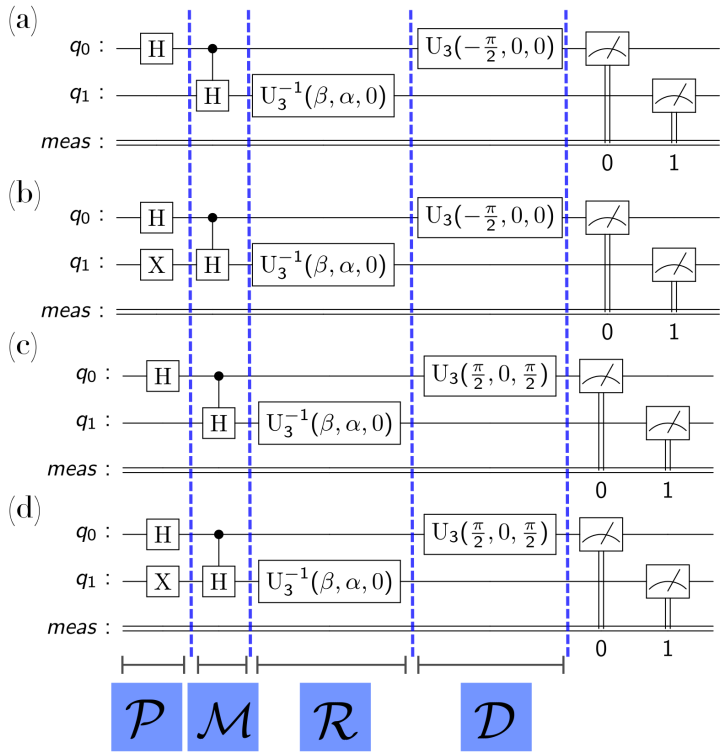


**Figure 3.2:** Set of quantum circuits for the Wigner process tomography of the Hadamard (H) gate. The initial state of the qubits is $|\psi\rangle_i = |00\rangle$. The four blocks of the algorithm preparation ($\mathcal{P}$), mapping ($\mathcal{M}$), rotation ($\mathcal{R}$), and detection-associated rotations ($\mathcal{U}$) are explicitly shown here.

Based on the experimentally measured droplet functions $f_0^{(\emptyset)}$ and $f_1^{(1)}$, a process matrix can be estimated (as shown in Sec. 3.3): any single-qubit unitary process can be expressed in terms of Pauli operators [3] as

$$U^{[1]} = \sum_{k=0}^{3} c_k \sigma_k \tag{3.15}$$

with in general complex coefficients $c_k$ for $k \in \{0,1,2,3\}$. Using Eq. 2.16, the coefficients $c_k$ are obtained by calculating the scalar product between the basis droplets $f_{\sigma_k}$ (refer to Sec. A.1.1) and the sum of the experimentally tomographed droplets $f_0^{(\emptyset)}$ and $f_1^{(1)}$:

$$c_k = \langle f_{\sigma_k} | f_0^{(\emptyset)} + f_1^{(1)} \rangle. \tag{3.16}$$

Table 3.1 summarizes the experimental process fidelities of the gates considered above. The standard deviation given in Table 3.1 was estimated by conducting the experiment three times for the NOT gate for reference.

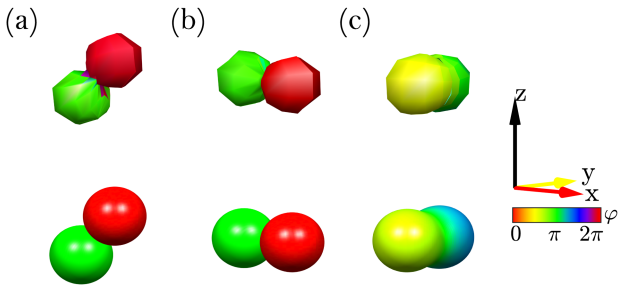


**Figure 3.3:** Experimentally tomographed (top panel) and simulated (lower panel) droplets for different quantum processes: (a) Hadamard gate, (b) NOT gate, and (c) $\left[\frac{3\pi}{2}\right]_y$ rotation. Refer to Fig. 3.4 for separate droplets of $f_0^{(\emptyset)}$ and $f_1^{(1)}$.

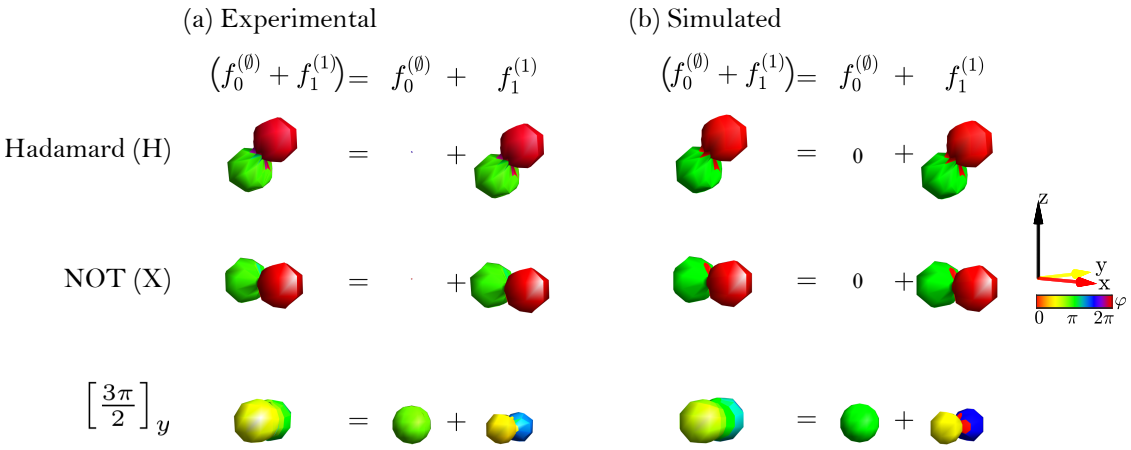


**Figure 3.4:** Experimentally tomographed (a) and simulated (b) droplets of different quantum processes. The rank $j = 0$ droplet $f_0^{(\emptyset)}$ and $j = 1$ droplet $f_1^{(1)}$ are shown here. Both experimental and simulated droplets are plotted with the same resolution.

**Table 3.1:** Experimental process tomography fidelity ($\mathcal{F}_U$) corresponds to target quantum gates $U_t$. The corresponding droplets are shown in Fig. 3.3.

| $U_t$ | $\mathcal{F}_U$ |
|---|---|
| Hadamard (H) | $0.9506 \pm 1 \times 10^{-3}$ |
| NOT (X) | $0.9679 \pm 1 \times 10^{-3}$ |
| $\left[\frac{3\pi}{2}\right]_y$ | $0.9407 \pm 1 \times 10^{-3}$ |

## 3.5 Performing WQPT on near-term quantum devices using DROPStomo

As described in Sec. 2.7 for state tomography, similarly, DROPStomo [27] can be used to perform Wigner process tomography (WQPT) for single qubit system on a simulator or on a quantum hardware. The package can be installed using the following command:

```
# install the package
pip install DROPStomo
```

Here, we give a code snippet for performing Wigner process tomography for a one-qubit system.

```
# import the required modules
from DROPStomo import WQPT1Q

# ***Input***
# Gate to tomograph.
Up = U3Gate(theta=pi, phi=0, lam=0)
# Resolution for scanning
res_beta= 8
res_alpha = 15
# Define target process matrix
Up = np.matrix([[0,1],[1,0]])

# Prepare quantum circuits for tomography
circ_u = WQPT1Q.WQPT_1Q_circuits(res_theta,Up)

# Provide a simulator or a quantum hardware. For example:
simulator = Aer.get_backend('qasm_simulator')

# Run quantum circuits on a simulator or on a quantum hardware.
WQPT1Q.WQPT_1Q_runner(res_theta, circuits=circ_u, device=simulator,
    shots=8192, inter=1, Ut=Up)
# ***Output***
# Experimental tomographed droplets (non-interactive, if inter=0 and
    interactive, if inter=1).
# Experimental expectation values.
# Experimental process matrix with process fidelity.
```

Chapter

# 4 Wigner Tomography of Unknown Quantum Processes

Building on the theory of the state and process tomography presented in the previous chapters, this chapter presents the extension of the Wigner tomography to unknown quantum processes.

The process tomography presented in Chapter 3 employs a mapping approach (refer to Sec. 3.1) that maps an $N$ qubit unitary process matrix $U^{[N]}$ onto the $N+1$ qubit Hermitian density matrix $\rho^{[N+1]}$, as depicted in the upper panel of Fig. 4.1. This mapping approach uses a controlled process operation $cU^{[N+1]}$ and the experimental implementation of which in general requires the knowledge of $U^{[N]}$ [58, 59], limiting the existing protocol of Wigner process tomography to known processes.

To address this limitation, we propose a novel quantum circuit that overcomes the constraints of the previous approach. This new circuit utilizes an additional set of $N$ ancilla qubits and maps the scaled versions of an *unknown* $N$ qubit process matrix onto $N+1$ qubit density matrices, as depicted in the lower panel of Fig. 4.1. This mapping allows for the experimental tomography of spherical droplets corresponding to scaled process matrices. Subsequently, these experimental tomographed droplets can be combined in a classical post-processing step to extract the unknown process matrix using the 'reconstruction algorithm' introduced herein.

In the following section, we initially discuss the circuit introduced in Sec. 3.1 designed to map a *known* process onto a density matrix. Subsequently, we demonstrate the process of mapping the scaled versions of an *unknown* process $U^{[N]}$ onto density matrices.

## 4.1 Theory for mapping an unknown unitary to density matrix

Here, we first revisit the circuit presented in Sec. 3.1 used for mapping a known process onto a density matrix.

For mapping an $N$ qubit known unitary process $U^{[N]}$ onto an $N+1$ qubit Hermitian density matrix $\rho^{[N+1]}$, a circuit shown in Fig. 4.2 is used. This mapping requires

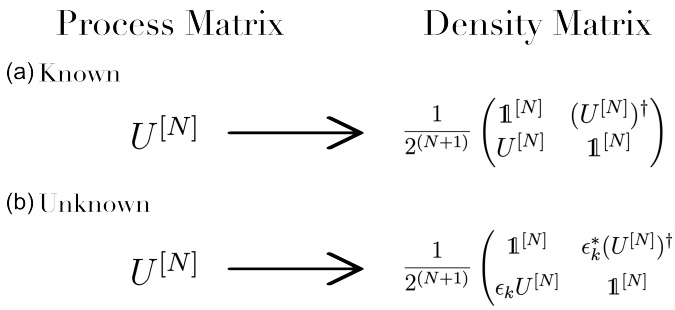


**Figure 4.1:** Schematic representation of mapping an $N$ qubit (a) known and (b) unknown process matrix $U^{[N]}$ onto an $N+1$ qubit density matrix, essential for Wigner tomography of quantum processes. In the case of an unknown process $U^{[N]}$, the scaled versions $\epsilon_k U^{[N]}$ are mapped onto density matrices. The general form of scaling factor $\epsilon_k$ is provided in Eq. 4.13.

preparing the control qubit $q_0$ in the superposition state $\frac{1}{\sqrt{2}}(|0\rangle + |1\rangle)$. Under the operation $cU^{[N+1]}$, the process $U^{[N]}$ only acts on system qubits $q_1 \dots q_N$ if the ancilla qubit $q_0$ is in the state $|1\rangle$. The states $|\psi_0\rangle$ and $|\psi_1\rangle$ in Fig. 4.2 are provided in Table 4.1 considering different initial states $|\psi_{q_0}\rangle$ of the control qubit $q_0$. As mentioned, mapping an *unknown* process matrix onto a density matrix using the circuit shown in Fig. 4.2 is not possible, as the design of the controlled operation $cU^{[N+1]}$ requires prior knowledge of the process $U^{[N]}$ [58, 59].

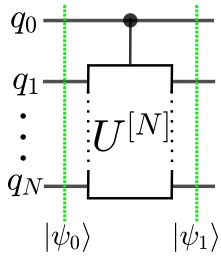


**Figure 4.2:** Schematic representation of the controlled process operation $cU^{[N+1]}$, which is employed to map a process matrix $U^{[N]}$ onto a density matrix $\rho^{[N+1]}$. Here, $q_0$ is an ancilla qubit and $q_1, \dots, q_N$ are system qubits. See Table 4.1 for state $|\psi_0\rangle$ and $|\psi_1\rangle$.

Now, we discuss a new approach to map scaled versions of the unknown process matrix onto density matrices. From here onward, we refer to $U^{[N]}$ as an *unknown* quantum process unless specified otherwise.

We are interested in mapping an unknown quantum process matrix onto a density matrix. To achieve this, we have adopted a circuit discussed in Ref. [60, 59], as illustrated in Fig. 4.3. In this case, for an $N$ qubit system, mapping an unknown process matrix requires additional $N+1$ qubits. Out of these $N+1$ ancillary qubits, $q_0$ is a control qubit. The initial state of system qubits $(q_1, \dots, q_N)$ and the ancilla qubits $(q_1^a, \dots, q_N^a)$ are rep-

**Table 4.1:** Evolution of the state after each block of the quantum circuit presented in Fig. 4.2 with different initial states $|\psi_{q_0}\rangle$ of the control qubit $q_0$. Initially, the system qubits $q_1 \dots q_N$ are in the state $|\psi_s\rangle$.

| $\|\psi\rangle$ | $\|\psi_{q_0}\rangle = \|0\rangle$ | $\|\psi_{q_0}\rangle = \|1\rangle$ | $\|\psi_{q_0}\rangle = \frac{1}{\sqrt{2}}(\|0\rangle + \|1\rangle)$ |
|---|---|---|---|
| $\|\psi_0\rangle$ | $\|0\psi_s\rangle$ | $\|1\psi_s\rangle$ | $\frac{1}{\sqrt{2}}\Big(\|0\psi_s\rangle + \|1\psi_s\rangle\Big)$ |
| $\|\psi_1\rangle$ | $\|0\psi_s\rangle$ | $\|1(U\psi_s)\rangle$ | $\frac{1}{\sqrt{2}}\Big(\|0\psi_s\rangle + \|1(U\psi_s)\rangle\Big)$ |

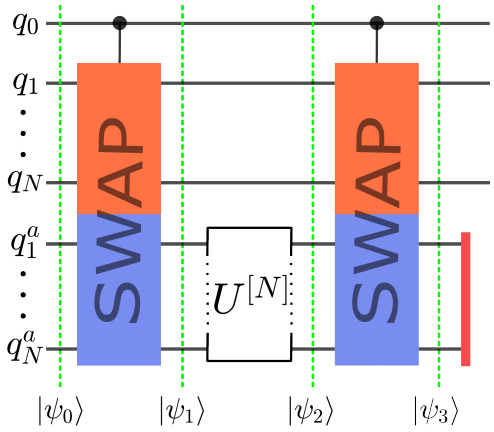


**Figure 4.3:** Schematic representation of a circuit for mapping an unknown unitary $U^{[N]}$ onto a density matrix with the inherent blind spots. Here, $q_1, \dots, q_N$ are system qubits and $q_0$ and $q_1^a, \dots, q_N^a$ are ancilla qubits. The first and third block of the circuit is a controlled-swap gate that swaps the upper (orange or dark gray) with the lower block (blue or light gray) only if the control qubit $q_0$ is in the state $|1\rangle$. The red barrier after the second controlled-swap block indicates partial tracing out of the ancilla qubits $q_1^a, \dots, q_N^a$. See Table 4.2 for the state description after each block for different initial states of the control qubit $q_0$.

resented by $|\psi_s\rangle$ and $|\psi_a\rangle$, respectively. Table 4.2 illustrates how the state evolves after each circuit block, considering three different initial states ($|\psi_{q_0}\rangle$) of the control qubit $q_0$.

Specifically, it demonstrates that when the control qubit $q_0$ is in either $|0\rangle$ or $|1\rangle$, i.e., in a computation basis state (*classical* state), the resulting state $|\psi_4\rangle$, after partially tracing out the ancilla qubits $q_1^a, \dots, q_N^a$, is identical to what would be expected in the case of a controlled process circuit (Fig. 4.2), as outlined in Table 4.1.

Although it is tempting to assume that the block CSWAP–$U^{[N]}(q_1^a, \dots, q_N^a)$–CSWAP shown in Fig. 4.3 implements $cU^{[N+1]}$ for arbitrary $U^{[N]}$, however, this is not the case if qubit $q_0$ is not in a computational basis state [60, 59]. When $q_0$ is in an equal superposition state, i.e., $|\psi_{q_0}\rangle = \frac{1}{\sqrt{2}}(|0\rangle + |1\rangle)$, the state following the second controlled swap gate ($|\psi_3\rangle$) is entangled. In this particular scenario, the partial tracing out of

**Table 4.2:** Evolution of the state after each block of the quantum circuit presented in Fig. 4.3 with different initial states $|\psi_{q_0}\rangle$ of the control qubit ($q_0$). Initially the system qubits $q_1 \dots q_N$ are in state $|\psi_s\rangle$, whereas the ancilla qubits $q_1^a \dots q_N^a$ are in state $|\psi_a\rangle$.

| $\|\psi\rangle$ | $\|\psi_{q_0}\rangle = \|0\rangle$ | $\|\psi_{q_0}\rangle = \|1\rangle$ | $\|\psi_{q_0}\rangle = \frac{1}{\sqrt{2}}(\|0\rangle + \|1\rangle)$ |
|---|---|---|---|
| $\|\psi_0\rangle$ | $\|0\psi_s\psi_a\rangle$ | $\|1\psi_s\psi_a\rangle$ | $\frac{1}{\sqrt{2}}\Big(\|0\psi_s\psi_a\rangle + \|1\psi_s\psi_a\rangle\Big)$ |
| $\|\psi_1\rangle$ | $\|0\psi_s\psi_a\rangle$ | $\|1\psi_a\psi_s\rangle$ | $\frac{1}{\sqrt{2}}\Big(\|0\psi_s\psi_a\rangle + \|1\psi_a\psi_s\rangle\Big)$ |
| $\|\psi_2\rangle$ | $\|0\psi_s(U\psi_a)\rangle$ | $\|1\psi_a(U\psi_s)\rangle$ | $\frac{1}{\sqrt{2}}\Big(\|0\psi_s(U\psi_a)\rangle + \|1\psi_a(U\psi_s)\rangle\Big)$ |
| $\|\psi_3\rangle$ | $\|0\psi_s(U\psi_a)\rangle$ | $\|1(U\psi_s)\psi_a\rangle$ | $\frac{1}{\sqrt{2}}\Big(\|0\psi_s(U\psi_a)\rangle + \|1(U\psi_s)\psi_a\rangle\Big)$ |
| $\|\psi_4\rangle^{\ddagger}$ | $\|0\psi_s\rangle$ | $\|1(U\psi_s)\rangle$ | non-pure state* |

$^{\ddagger}$ The state vector description can only be written when $|\psi_{q_0}\rangle$ is either $|0\rangle$ or $|1\rangle$.
* See Eq. 4.5 for the case of a single-qubit ($N = 1$).

ancilla qubits $q_1^a, \dots, q_N^a$ from the remaining qubits $q_0, q_1, \dots, q_N$ will result in a loss of information. We now focus on a single-qubit ($N = 1$) system to understand the loss of information.

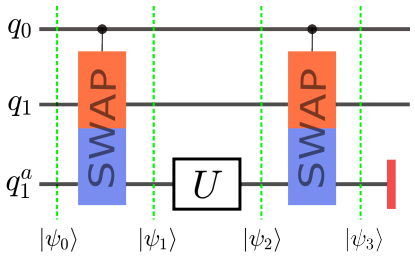


**Figure 4.4:** The redrawn version of circuit in Fig. 4.3 for a single-qubit ($N = 1$) system. In this figure, $q_1$ is the system qubit and $q_0$ and $q_1^a$ are ancilla qubits.

For a single-qubit ($N = 1$) system, a total of three qubits are required in this protocol: $q_0$, $q_1$, and $q_1^a$. We redraw the general circuit presented in Fig. 4.3 for $N = 1$ in Fig. 4.4. To facilitate the mapping of a process matrix onto a density matrix for Wigner process tomography, initially, the control qubit $q_0$ is required to be in an equal superposition state, while the qubits $q_1$ and $q_1^a$ are required to be in a maximally mixed state, i.e., $\rho_s^{[1]} = |\psi_s\rangle\langle\psi_s| = \frac{1}{2}\mathbb{1}^{[1]}$ and $\rho_a^{[1]} = |\psi_a\rangle\langle\psi_a| = \frac{1}{2}\mathbb{1}^{[1]}$, respectively. Hence, the density matrix $\rho_0$ is:

$$\rho_0^{[3]} = \frac{(|0\rangle + |1\rangle)(\langle 0| + \langle 1|)}{2} \otimes \frac{1}{2}\mathbb{1}^{[1]} \otimes \frac{1}{2}\mathbb{1}^{[1]} = \frac{1}{8}\begin{pmatrix} \mathbb{1}^{[2]} & \mathbb{1}^{[2]} \\ \mathbb{1}^{[2]} & \mathbb{1}^{[2]} \end{pmatrix}, \tag{4.1}$$

After the first controlled-swap block, the density matrix $\rho_1 = |\psi_1\rangle\langle\psi_1|$ is:

$$\begin{aligned}\rho_1^{[3]} &= \begin{pmatrix} \mathbb{1}^{[2]} & 0^{[2]} \\ 0^{[2]} & \text{swap}^{[2]} \end{pmatrix} \rho_0^{[3]} \begin{pmatrix} \mathbb{1}^{[2]} & 0^{[2]} \\ 0^{[2]} & \text{swap}^{[2]} \end{pmatrix}^\dagger \\ &= \frac{1}{8} \begin{pmatrix} \mathbb{1}^{[2]} & \text{swap}^{[2]} \\ \text{swap}^{[2]} & \mathbb{1}^{[2]} \end{pmatrix}.\end{aligned} \tag{4.2}$$

The matrix form of the controlled-swap gate is provided in Eq. 1.14. The controlled-swap gate is written as a block diagonal matrix. The matrix form of the lower diagonal block *swap* is given in Eq. 1.12. After the operation $\mathbb{1}^{[2]} \otimes U^{[1]}$ (second block of circuit in Fig. 4.4), one obtains

$$\begin{aligned}\rho_2^{[3]} &= \begin{pmatrix} \mathbb{1}^{[1]} \otimes U^{[1]} & 0^{[2]} \\ 0^{[2]} & \mathbb{1}^{[1]} \otimes U^{[1]} \end{pmatrix} \rho_1^{[3]} \begin{pmatrix} \mathbb{1}^{[1]} \otimes U^{[1]} & 0^{[2]} \\ 0^{[2]} & \mathbb{1}^{[1]} \otimes U^{[1]} \end{pmatrix}^\dagger \\ &= \frac{1}{8} \begin{pmatrix} \mathbb{1}^{[2]} & (\mathbb{1}^{[1]} \otimes U^{[1]})\text{swap}^{[2]}(\mathbb{1}^{[1]} \otimes (U^{[1]})^\dagger) \\ (\mathbb{1}^{[1]} \otimes U^{[1]})\text{swap}^{[2]}(\mathbb{1}^{[1]} \otimes (U^{[1]})^\dagger) & \mathbb{1}^{[2]} \end{pmatrix}.\end{aligned} \tag{4.3}$$

The density matrix after the second controlled-swap block of the circuit in Fig. 4.4 is:

$$\begin{aligned}\rho_3^{[3]} &= \begin{pmatrix} \mathbb{1}^{[2]} & 0^{[2]} \\ 0^{[2]} & \text{swap}^{[2]} \end{pmatrix} \rho_2^{[3]} \begin{pmatrix} \mathbb{1}^{[2]} & 0^{[2]} \\ 0^{[2]} & \text{swap}^{[2]} \end{pmatrix}^\dagger \\ &= \frac{1}{8} \begin{pmatrix} \mathbb{1}^{[2]} & (U^{[1]})^\dagger \otimes U^{[1]} \\ U^{[1]} \otimes (U^{[1]})^\dagger & \mathbb{1}^{[2]} \end{pmatrix}.\end{aligned} \tag{4.4}$$

After tracing out ancilla qubit $q_1^a$ (indicated by the red barrier in the circuit depicted in Fig. 4.4), the density matrix is

$$\tilde{\rho}_4^{[2]} = \frac{1}{4} \begin{pmatrix} \mathbb{1}^{[1]} & c^* \cdot (U^{[1]})^\dagger \\ c \cdot U^{[1]} & \mathbb{1}^{[1]} \end{pmatrix}, \tag{4.5}$$

with scaling factor

$$c = \frac{1}{2} \operatorname{tr}(U^\dagger). \tag{4.6}$$

In Eq. 4.5, $c^*$ is the complex conjugate of $c$. Eq. 4.5 shows that it is possible to map the unknown single-qubit process $U^{[1]}$ onto the density matrix $\tilde{\rho}_4^{[2]}$ using the circuit shown in Fig. 4.4 up to a scaling factor $c = \frac{1}{2}\operatorname{tr}(U^\dagger)$. This scaling factor results from the partial tracing out of the ancilla qubit from the entangled state in Eq. 4.5, leading to a loss of information, as mentioned earlier. For example, in the case of a general

single-qubit rotation with *rotation angle* $\gamma$ and rotation axis $\vec{n} = (n_x, n_y, n_z)$, given by [3]

$$U = \cos\left(\frac{\gamma}{2}\right)\mathbb{1} - i \cdot \sin\left(\frac{\gamma}{2}\right)(n_x\sigma_x + n_y\sigma_y + n_z\sigma_z), \tag{4.7}$$

and since the Pauli matrices $\sigma_x$, $\sigma_y$, and $\sigma_z$ are traceless, the scaling factor is simply

$$c = \cos\left(\frac{\gamma}{2}\right). \tag{4.8}$$

The mapping of a unitary operator $U$ onto the off-diagonal blocks of $\tilde{\rho}_4^{[2]}$ in Eq. 4.5 is lossless (corresponding to $|c| = 1$) only when the rotation angle is a multiple of $2\pi$ (i.e., $\gamma = 2n\pi$ for $n \in \mathbb{Z}$). However, in the general case, the off-diagonal blocks of the density matrix $\tilde{\rho}_4^{[2]}$ are scaled down ($|c|<1$), which would result in a loss of signal-to-noise ratio in the experimental tomography results. For example, for the $\sqrt{\text{NOT}}$ gate (which has a rotation angle of $\gamma = \frac{\pi}{2}$), the scaling factor is only $c = \sqrt{\frac{1}{2}}$. In the case of processes for which $|c|$ approaches 0, the protocol given in Fig. 4.3 has actually *blind spots*, where no information about the process of interest is obtained. This occurs whenever the rotation angle $\gamma$ is close to an odd multiple of $\pi$ (i.e., if $\gamma = (2n+1)\pi$ for $n \in \mathbb{Z}$), which, in fact, is the case for many standard quantum gates like NOT (X), Y, Z, and Hadamard (H) gates. In order to overcome these limitations and remove the blind spots inherent in the approach, we extend the circuit presented in Fig. 4.3 and discuss it in the next section.

## 4.2 Modified circuit for mapping

To remove the *blind spots* caused by the circuit depicted in Fig. 4.3, we propose the extended quantum circuit shown in Fig. 4.5. In this new circuit design, we introduce a controlled rotation denoted as $c\mathcal{G}_k^{[N]}$, which exclusively operates on the ancilla qubits $q_1^a, \ldots, q_N^a$ when the control qubit $q_0$ assumes the state $|1\rangle$.

For a system comprising of $N$ qubits $q_1, \ldots, q_N$, the circuit shown in Fig. 4.5 is reiterated with varying rotations $\mathcal{G}_k^{[N]}$, extending up to $4^N$ repetitions. Here, '$4^N$' refers to the number of elements in the Pauli operator basis for a system consisting of $N$ qubits. For instance, for a single system qubit ($N = 1$), $k$ ranges from 1 to 4, since $\mathcal{G}_k^{[1]} \in \{\sigma_x, \sigma_y, \sigma_z, \mathbb{1}\}$, i.e., $\mathcal{G}_1^{[1]} = \sigma_x$, $\mathcal{G}_2^{[1]} = \sigma_y$, $\mathcal{G}_3^{[1]} = \sigma_z$, and $\mathcal{G}_4^{[1]} = \mathbb{1}$. Similarly, for a system with two qubits ($N = 2$), $k$ spans from 1 to 16, as $\mathcal{G}_k^{[2]} \in \{\sigma_x \otimes \mathbb{1}, \ldots, \mathbb{1} \otimes \sigma_x, \ldots, \sigma_z \otimes \sigma_z, \mathbb{1} \otimes \mathbb{1}\}$. In the general case, $\mathcal{G}_k$ may represent any generic multi-qubit rotation.

Table 4.3 describes the state evolution after each block of the circuit displayed in Fig. 4.5. This analysis is conducted under the initial conditions in which the control qubit $q_0$ is in the state $|\psi_{q_0}\rangle = \frac{1}{\sqrt{2}}(|0\rangle + |1\rangle)$, the system qubits $q_1 \ldots q_N$ are in the state $|\psi_s\rangle$, and the ancilla qubits $q_1^a \ldots q_N^a$ are in the state $|\psi_a\rangle$.

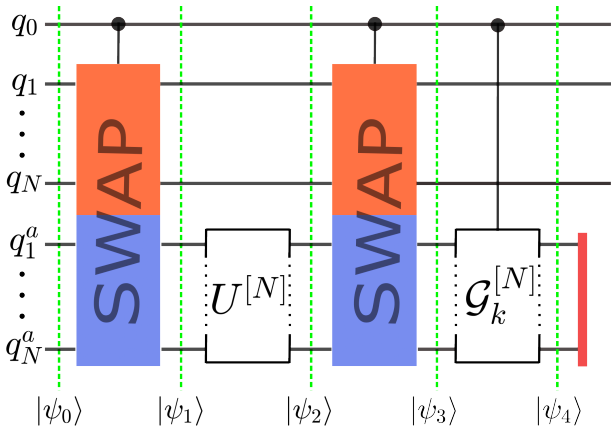


**Figure 4.5:** Circuit for mapping unknown scaled process matrices $\epsilon_k U^{[N]}$ onto density matrices without introducing blind spots by repeating the experiments for different gates $\mathcal{G}_k$. Here, $q_1, \ldots, q_N$ are system qubits and qubits $q_0$ and $q_1^a, \ldots, q_N^a$ are ancilla qubits. See Table 4.3 for the state evolution after each circuit block.

**Table 4.3:** Evolution of a quantum state after each block of a quantum circuit presented in Fig. 4.5. Considering initially the control qubit $q_0$ to be in state $|\psi_{q_0}\rangle = \frac{1}{\sqrt{2}}(|0\rangle + |1\rangle)$, the system qubits $q_1 \ldots q_N$ in the state $|\psi_s\rangle$, and the ancilla qubits $q_1^a \ldots q_N^a$ in the state $|\psi_a\rangle$.

| $\|\psi\rangle$ | $\|\psi_{q_0}\rangle = \frac{1}{\sqrt{2}}(\|0\rangle + \|1\rangle)$ |
|---|---|
| $\|\psi_0\rangle$ | $\frac{1}{\sqrt{2}}\Big(\|0\psi_s\psi_a\rangle + \|1\psi_s\psi_a\rangle\Big)$ |
| $\|\psi_1\rangle$ | $\frac{1}{\sqrt{2}}\Big(\|0\psi_s\psi_a\rangle + \|1\psi_a\psi_s\rangle\Big)$ |
| $\|\psi_2\rangle$ | $\frac{1}{\sqrt{2}}\Big(\|0\psi_s(U\psi_a)\rangle + \|1\psi_a(U\psi_s)\rangle\Big)$ |
| $\|\psi_3\rangle$ | $\frac{1}{\sqrt{2}}\Big(\|0\psi_s(U\psi_a)\rangle + \|1(U\psi_s)\psi_a\rangle\Big)$ |
| $\|\psi_4\rangle$ | $\frac{1}{\sqrt{2}}\Big(\|0\psi_s(U\psi_a)\rangle + \|1(U\psi_s)(\mathcal{G}_k\psi_a)\rangle\Big)$ |

To understand it better, let us look at the density matrix calculations for a single-qubit ($N = 1$) system. We redraw the circuit presented in Fig. 4.5 for a single qubit system in Fig. 4.6. For $N = 1$ system, the circuit in Fig. 4.6 is repeated 4 times which corresponds to rotation $\mathcal{G}_k^{[1]} \in \{\sigma_x, \sigma_y, \sigma_z, \mathbb{1}\}$, i.e., $\mathcal{G}_1^{[1]} = \sigma_x$, $\mathcal{G}_2^{[1]} = \sigma_y$, $\mathcal{G}_3^{[1]} = \sigma_z$, and $\mathcal{G}_4^{[1]} = \mathbb{1}$. Let us see how the additional block $c\mathcal{G}_k$ addresses the limitation of the previous circuit for $N = 1$ in Fig. 4.4.

Under the $c\mathcal{G}_k^{[1]}$ operation, the density matrix $\rho_3$ in Eq. 4.4 (corresponding to the

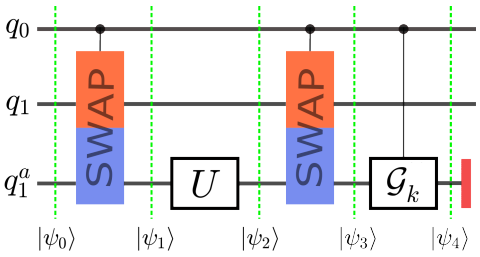


**Figure 4.6:** Redrawing of the circuit depicted in Fig. 4.5 tailored for a single-qubit system ($N = 1$). This circuit maps single-qubit scaled process matrices $\epsilon_k U^{[1]}$ onto density matrices, repeating for $k = 1 : 4$, corresponding to rotations $\mathcal{G}_k^{[1]} \in \{\sigma_x, \sigma_y, \sigma_z, \mathbb{1}\}$, i.e., $\mathcal{G}_1^{[1]} = \sigma_x$, $\mathcal{G}_2^{[1]} = \sigma_y$, $\mathcal{G}_3^{[1]} = \sigma_z$, and $\mathcal{G}_4^{[1]} = \mathbb{1}$. The associated scaling factors $\epsilon_k$ are provided in Table 4.4.

state $|\psi_3\rangle$, i.e., after the second controlled-swap block of Fig. 4.6) is transformed to:

$$\begin{aligned}\rho_4^{[3]} &= \begin{pmatrix} \mathbb{1}^{[2]} & 0^{[2]} \\ 0^{[2]} & \mathbb{1}^{[1]} \otimes \mathcal{G}_k^{[1]} \end{pmatrix} \rho_3^{[3]} \begin{pmatrix} \mathbb{1}^{[2]} & 0^{[2]} \\ 0^{[2]} & \mathbb{1}^{[1]} \otimes \mathcal{G}_k^{[1]} \end{pmatrix}^\dagger \\ &= \frac{1}{8} \begin{pmatrix} \mathbb{1}^{[2]} & (U^{[1]})^\dagger \otimes U^{[1]} (\mathcal{G}_k^{[1]})^\dagger \\ U^{[1]} \otimes \mathcal{G}_k^{[1]} (U^{[1]})^\dagger & \mathbb{1}^{[2]} \end{pmatrix},\end{aligned} \tag{4.9}$$

where $\rho_4 = |\psi_4\rangle\langle\psi_4|$.

The density matrix $\tilde{\rho}_5^{[2]} = |\psi_5\rangle\langle\psi_5|$ after tracing out ancilla qubit $q_1^a$ (indicated by the red barrier in the circuit depicted in Fig. 4.6) is:

$$\tilde{\rho}_5^{[2]} = \frac{1}{4} \begin{pmatrix} \mathbb{1}^{[1]} & \epsilon_k^* (U^{[1]})^\dagger \\ \epsilon_k U^{[1]} & \mathbb{1}^{[1]} \end{pmatrix}, \tag{4.10}$$

which can be rewritten as:

$$\rho_{U_k}^{[2]} = \frac{1}{4} \begin{pmatrix} \mathbb{1}^{[1]} & (U_k^{[1]})^\dagger \\ U_k^{[1]} & \mathbb{1}^{[1]} \end{pmatrix}, \tag{4.11}$$

where

$$U_k^{[1]} = \epsilon_k U^{[1]}, \tag{4.12}$$

and the scaling factor

$$\epsilon_k = \frac{1}{2} \operatorname{tr}((U^{[1]})^\dagger \mathcal{G}_k^{[1]}) = \frac{1}{2} \langle U^{[1]} | \mathcal{G}_k^{[1]} \rangle. \tag{4.13}$$

In Eq. 4.10, $\epsilon_k^*$ represents the complex conjugate of $\epsilon_k$ and $k$ ranges from 1 to 4. Depending on the rotation $\mathcal{G}_k$, different scaled process matrices $U_k^{[1]}$ defined in Eq. 4.12 are

mapped onto the off-diagonal blocks of the density matrix $\rho^{[2]}_{U_k}$ in Eq. 4.11. In the case where $\mathcal{G} = \mathbb{1}$, the density matrix $\rho^{[2]}_{U_k}$ in Eq. 4.11 is identical to $\tilde{\rho}^{[2]}_4$ in Eq. 4.5 and Eq. 4.6.

If the unitary operator $U$ happens to be equal to $\mathcal{G}_k$ for a specific $k$, then $\epsilon_k = 1$, resulting in an exact (lossless) mapping of process $U$ onto a density matrix $\rho^{[2]}_{U_k}$. This is also evident in the state vector formalism provided in Table 4.3. In this context, when $\mathcal{G}_k = U$, the state $|\psi_4\rangle$ modifies to:

$$\begin{aligned} |\psi_4\rangle' &= \frac{1}{\sqrt{2}}(|0\psi_s(U\psi_a)\rangle + |1(U\psi_s)(U\psi_a)\rangle) \\ &= \frac{1}{\sqrt{2}}(|0\psi_s\rangle + |1(U\psi_s)\rangle) \otimes (U|\psi_a\rangle), \end{aligned} \tag{4.14}$$

indicating that the ancilla qubit $q^a_1$ is fully separable from the qubits $q_0$ and $q_1$.

However, in general, where $U$ differs from $\mathcal{G}_k$, the state $|\psi_4\rangle$ remains entangled, leading to the mapping of scaled process matrices $U_k$ onto density matrices. The corresponding scaling factors $\epsilon_k$ for different rotations $\mathcal{G}^{[1]}_k$ are provided in Table 4.4 for a single-qubit special unitary process matrix given as:

$$U^{[1]} = \begin{pmatrix} u_{11} & u_{12} \\ u_{21} & u_{22} \end{pmatrix} = \begin{pmatrix} D + iC & B + iA \\ -B + iA & D - iC \end{pmatrix}. \tag{4.15}$$

Here $U^{[1]}$ is written using the usual representation of quaternions as complex $2 \times 2$ matrices [61], and for this matrix to be special unitary the real components $A, B, C$, and $D$ must satisfy the condition $A^2 + B^2 + C^2 + D^2 = 1$. In Table 4.4, the second column presents the scaling factors in terms of matrix elements $u_{11}$, $u_{12}$, $u_{21}$, and $u_{22}$, while the third column expresses them in terms of quaternions $A$, $B$, $C$, and $D$. The resulting scaled matrices $U^{[1]}_k$ are displayed in the fourth column. For simplicity and to keep a consistent droplet color, the first three scaled process matrices, i.e., $U^{[1]}_{k=1:3}$ are divided by '$(-i)$', resulting in

$$\hat{U}^{[1]}_{k=1:3} = \frac{1}{(-i)}(U^{[1]}_{k=1:3}) = iU^{[1]}_{k=1:3}. \tag{4.16}$$

The new scaled process matrices $\hat{U}^{[1]}_k$ are presented in the last column of Table 4.4.

An example of the scaling factor corresponding to different rotations is depicted in Fig. 4.7, considering $A = 0.15, B = 0.35, C = 0.55$, and $D = 0.7433$. The droplet corresponding to the unknown process $U^{[1]}$ is presented on the left, while the scaled process droplets $\hat{U}^{[1]}_k$ associated with different controlled rotations $c\mathcal{G}$ are displayed on the right of Fig. 4.7.

**Table 4.4:** The table presents the scaling factors ($\epsilon_k$) for a single-qubit system ($N = 1$) corresponding to different controlled rotations with $\mathcal{G}_k^{[1]} \in \{\sigma_x, \sigma_y, \sigma_z, \mathbb{1}\}$ and the resulting scaled process matrices $U_k^{[1]}$. The second column presents the scaling factor in terms of matrix elements $u_{11}$, $u_{12}$, $u_{21}$, and $u_{22}$, while the third column expresses them in terms of quaternions $A$, $B$, $C$, and $D$. The last column presents the scaled matrices $\hat{U}_k^{[1]}$ defined in Eq. 4.16. See Fig. 4.7 for an example.

| $\mathcal{G}_k^{[1]}$ | $\epsilon_k$ | $\epsilon_k$ | $U_k^{[1]} = \epsilon_k U^{[1]}$ | $\hat{U}_k^{[1]}$ |
|---|---|---|---|---|
| $\sigma_x$ | $\frac{1}{2}(u_{12}^* + u_{21}^*)$ | $-(i)A$ | $-(i)AU^{[1]}$ | $AU^{[1]}$ |
| $\sigma_y$ | $\frac{i}{2}(u_{21}^* - u_{12}^*)$ | $-(i)B$ | $-(i)BU^{[1]}$ | $BU^{[1]}$ |
| $\sigma_z$ | $\frac{1}{2}(u_{11}^* - u_{22}^*)$ | $-(i)C$ | $-(i)CU^{[1]}$ | $CU^{[1]}$ |
| $\mathbb{1}$ | $\frac{1}{2}(u_{11}^* + u_{22}^*)$ | $D$ | $DU^{[1]}$ | $DU^{[1]}$ |

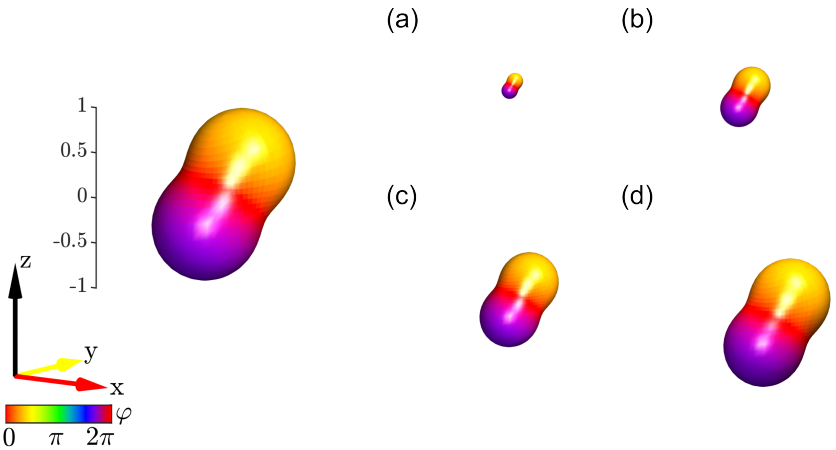


**Figure 4.7:** Spherical droplet representing a process matrix $U^{[1]}$ (on the left) with quaternion components $A = 0.15$, $B = 0.35$, $C = 0.55$, and $D = 0.7433$. The resulting droplets corresponding to scaled process matrices $\hat{U}_1^{[1]} = AU^{[1]}$(a), $\hat{U}_2^{[1]} = BU^{[1]}$(b), $\hat{U}_3^{[1]} = CU^{[1]}$(c), and $\hat{U}_4^{[1]} = DU^{[1]}$(d) associated with different controlled rotations $c\mathcal{G}$, with $\mathcal{G} = \sigma_x$, $\sigma_y$, $\sigma_z$, and $\mathbb{1}$ respectively, are displayed on the right. Refer to Table 4.4 for scaling factors $\epsilon_k$ corresponding to different rotations $\mathcal{G}_k^{[1]}$ and the resulting process matrices $\hat{U}_k^{[1]}$.

In general, for a system consisting of $N$ qubits, Eq. 4.10 can be generalized to:

$$\rho_{U_k}^{[N+1]} = \frac{1}{2^{(N+1)}} \begin{pmatrix} \mathbb{1}^{[N]} & \epsilon_k^* (U^{[N]})^\dagger \\ \epsilon_k U^{[N]} & \mathbb{1}^{[N]} \end{pmatrix}, \tag{4.17}$$

with scaling factor

$$\epsilon_k = \frac{1}{2^N} \langle U^{[N]} | \mathcal{G}_k^{[N]} \rangle. \tag{4.18}$$

A proof of this generalization is provided in supplementary Sec. C.1. In this general

case, $k$ ranges from 1 to $2^N$.

Now, using the quantum circuit shown in Fig. 4.5, the scaled process matrices $U_k^{[N]} = \epsilon_k U^{[N]}$ of an $N$ qubit unknown process matrix $U^{[N]}$ are mapped onto the $N+1$ qubit density matrices $\rho_{U_k}^{[N+1]}$ (see Eq. 4.17). The following section formalizes the Wigner process tomography, aiming to experimentally tomograph the droplets corresponding to the scaled process matrices $U_k^{[N]}$.

## 4.3 Theory of Wigner tomography of unknown processes

We first extend the Wigner tomography algorithm presented in Ref. [28] to unknown processes and then explain each step individually. A schematic of the algorithm is shown in Fig. 4.8. A spherical droplet function $f_{j,k}^{(\ell)}$ representing a scaled quantum process $U_k^{[N]}$ can be experimentally tomographed using the following steps:

1. **Preparation ($\mathcal{P}$)**: Prepare ancilla qubit $q_0$ in the superposition state $\frac{1}{\sqrt{2}}(|0\rangle + |1\rangle)$ and effectively create the remaining qubits $q_1, \ldots, q_N, q_1^a, \ldots, q_N^a$ in a fully mixed state.

2. **Mapping ($\mathcal{M}$)**: Implement the circuit presented in Fig. 4.5 to map the *scaled* unknown operators $U_k^{[N]}$ onto density matrices $\rho_{U_k}^{[N+1]}$ for different $k$.

3. **Rotation ($\mathcal{R}$)**: Rotate the system qubits $q_1, \ldots, q_N$ inversely for scanning.

4. **Detection-associated rotations ($\mathcal{D}$)**: Apply local unitary operations to measure the required expectation values of axial tensor operators $T_{j0}^{(\ell)[N]}$ (see Table 2.1) that are not directly measurable.

These four steps are repeated for a set of polar $\beta \in [0, \pi]$ and azimuthal $\alpha \in [0, 2\pi]$ angles and for different $n$, rank $j$, label $\ell$, and controlled rotations ($c\mathcal{G}_k$). Now we explain each step of the algorithm.

*Step 1:* Considering the algorithm starts with the state $\rho_i = |00\ldots0\rangle\langle00\ldots0|$, qubit $q_0$ is prepared in the equal superposition state $\frac{1}{\sqrt{2}}(|0\rangle+|1\rangle)$ by applying a Hadamard gate. A maximally mixed state of qubits $q_1, \ldots, q_N, q_1^a, \ldots, q_N^a$ can be effectively created by temporally averaging the results of experiments conducted on all possible computational basis states [28] (see supplementary Sec. B.2). This can be achieved by appropriately utilizing local NOT gates. We discuss this for the case of a single system qubit in Sec. 4.6.

*Step 2:* The circuit presented in Fig. 4.5 is implemented to map the scaled process matrices $U_k^{[N]}$ onto the density matrices $\rho_{U_k}^{[N+1]}$ (refer to Eq. 4.17).

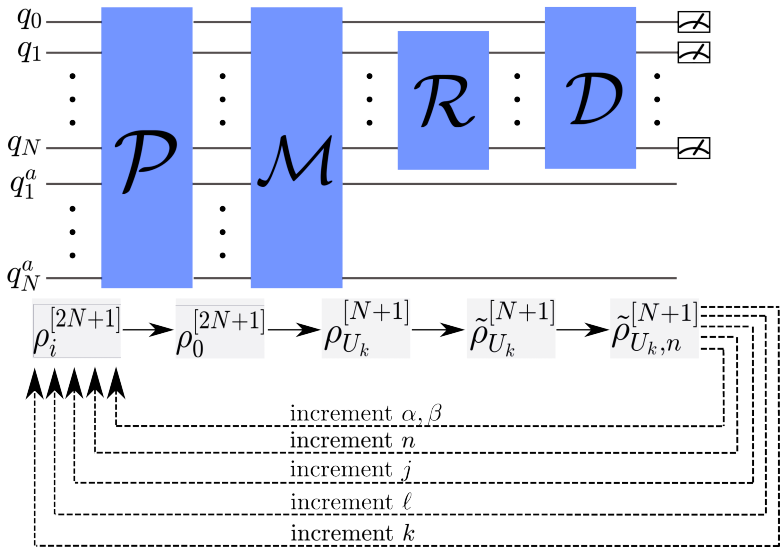


**Figure 4.8:** Schematic for the Wigner tomography for unknown processes. The algorithm consists of four key blocks: Preparation ($\mathcal{P}$), Mapping ($\mathcal{M}$), Rotation ($\mathcal{R}$), and Detection-associated rotations ($\mathcal{D}$) followed by measurements. The $\mathcal{M}$ block is replaced with the circuit presented in Fig. 4.5. The lower part of the figure shows the evolution of the density matrix after each block. The algorithm is repeated for different parameters.

*Step 3:* Here, we are interested in measuring a droplet function $f_{j,k}^{(\ell)}$ representing a scaled process matrix $U_k^{[N]}$. In this case, Eq. 3.6, takes the form:

$$f_{j,k}^{(\ell)}(\beta,\alpha) = s_j \langle \sigma^+ \otimes T_{j,\alpha\beta}^{(\ell)[N]} \rangle_{\rho_{U_k}^{[N+1]}}. \tag{4.19}$$

Now, instead of rotating the axial tensor operators $T_{j0}^{(\ell)[N]}$, we equivalently rotate the density matrix of the system qubits $q_1, \ldots, q_N$ inversely, such that:

$$f_{j,k}^{(\ell)}(\beta,\alpha) = s_j \langle \sigma^+ \otimes T_{j0}^{(\ell)[N]} \rangle_{\tilde{\rho}_{U_k}^{[N+1]}}, \tag{4.20}$$

where

$$\tilde{\rho}_{U_k}^{[N+1]} = (R_{\alpha\beta}^{[N+1]})^{-1} \rho_{U_k}^{[N+1]} R_{\alpha\beta}^{[N+1]}, \tag{4.21}$$

and $R_{\alpha\beta}^{[N+1]} = \mathbb{1}^{[1]} \otimes R_{\alpha\beta}^{[N]}$, i.e., the rotation operator $R_{\alpha\beta}^{[N]}$ acts only on the system qubits $q_1, \ldots, q_N$. The rotation operator $R_{\alpha\beta}^{[N]}$ is the same as shown in Eq. 2.2. Using the relation $\sigma^+ = \frac{1}{2}(\sigma_x + i\sigma_y)$, Eq. 4.20 can be rewritten in terms of Pauli operators as:

$$f_{j,k}^{(\ell)}(\beta,\alpha) = \frac{s_j}{2}\Big( \langle \sigma_x \otimes T_{j0}^{(\ell)[N]} \rangle_{\tilde{\rho}_{U_k}^{[N+1]}} + i \langle \sigma_y \otimes T_{j0}^{(\ell)[N]} \rangle_{\tilde{\rho}_{U_k}^{[N+1]}} \Big). \tag{4.22}$$

*Step 4:* Similar to the Wigner state and known-process tomography, the expectation values of Pauli operators, which can not be observed directly, can be measured with the

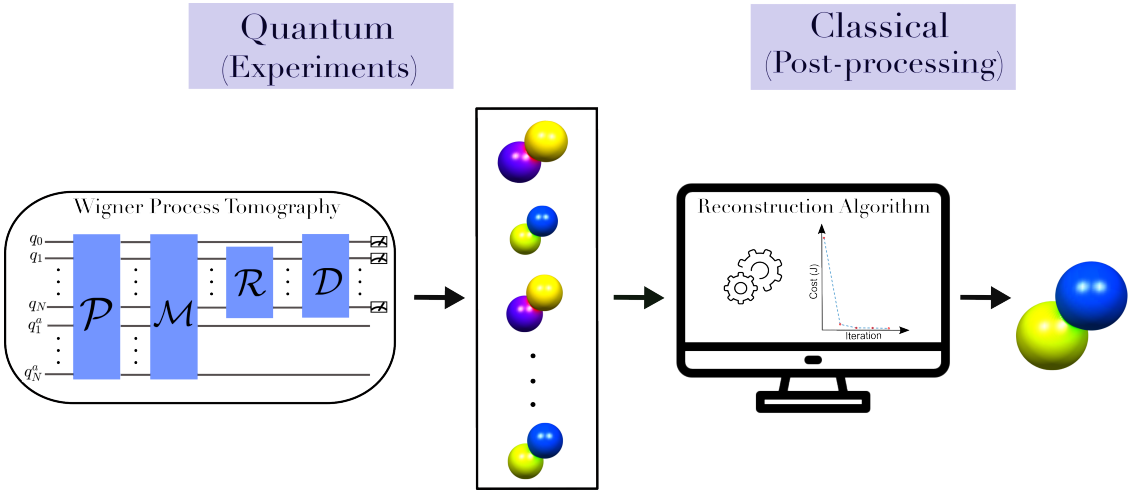


**Figure 4.9:** Schematic of the approach of Wigner process tomography of unknown processes. The Wigner process tomography approach experimentally tomographs the spherical droplets $f_{j,k}^{(\ell)}$ corresponding to the scaled versions of an unknown process $U_k^{[N]}$ (on the left). Subsequently, the experimental droplets are combined using a reconstruction algorithm to estimate a droplet corresponding to the unknown process $U$ with a high signal-to-noise ratio in the post-processing step (on the right).

help of local unitary operations $u_n$ (detection-associated rotations). Refer to Sec. 2.2 for an example.

By employing Eq. 4.22, we can experimentally tomograph the droplet functions $f_{j,k}^{(\ell)}$ corresponding to the scaled matrices $U_k^{[N]}$. This method provides information about the scaled unknown matrices $U_k^{[N]}$, and we have developed a methodology to combine these experimentally tomographed scaled droplets to reconstruct an unknown process $U^{[N]}$ with high signal-to-noise ratio. Consequently, the entire Wigner tomography approach for an unknown process comprises of two integral components: a quantum aspect (corresponds to experiments) and a classical aspect (concerning the post-processing of experimental data), as illustrated in the schematic in Fig. 4.9.

## 4.4 Reconstruction of an unknown process from scaled process droplets

In this section, we present a methodology to reconstruct an unknown process $U$ from the experimentally tomographed droplet functions $f_{j,k}^{(\ell)}$ corresponding to the scaled processes $U_k^{[N]}$ for a single system qubit ($N = 1$).

Let us first rewrite the Eq. 4.22 for a single system qubit $N = 1$. For $N = 1$, the possible values of rank $j$ are: $j = 0$ for label $\ell = \emptyset$, and $j = 1$ for label $\ell = 1$ (refer to

Table 2.1). Hence, single qubit scaled processes $U_k^{[1]}$ represented by spherical functions $f_{0,k}^{(\emptyset)}$ and $f_{1,k}^{(1)}$ can be experimentally tomographed using:

$$\begin{aligned} f_{0,k}^{(\emptyset)}(\beta,\alpha) &= \frac{1}{2}\sqrt{\frac{1}{4\pi}}\Big(\langle\sigma_x \otimes T_{00}^{(\ell)[1]}\rangle_{\tilde{\rho}_{U_k}^{[2]}} + i\langle\sigma_y \otimes T_{00}^{(\ell)[1]}\rangle_{\tilde{\rho}_{U_k}^{[2]}}\Big), \\ f_{1,k}^{(1)}(\beta,\alpha) &= \frac{1}{2}\sqrt{\frac{3}{4\pi}}\Big(\langle\sigma_x \otimes T_{10}^{(1)[1]}\rangle_{\tilde{\rho}_{U_k}^{[2]}} + i\langle\sigma_y \otimes T_{10}^{(1)[1]}\rangle_{\tilde{\rho}_{U_k}^{[2]}}\Big). \end{aligned} \tag{4.23}$$

Substituting the explicit values of spherical tensor operators in terms of Pauli operators from Table 2.1 simplifies the above equation as:

$$\begin{aligned} f_{0,k}^{(\emptyset)}(\beta,\alpha) &= \frac{1}{4}\sqrt{\frac{1}{2\pi}}\Big(\langle\sigma_{0x}\rangle_{\tilde{\rho}_{U_k}^{[2]}} + i\langle\sigma_{0y}\rangle_{\tilde{\rho}_{U_k}^{[2]}}\Big), \\ f_{1,k}^{(1)}(\beta,\alpha) &= \frac{1}{4}\sqrt{\frac{3}{2\pi}}\Big(\langle\sigma_{0x}\sigma_{1z}\rangle_{\tilde{\rho}_{U_k}^{[2]}} + i\langle\sigma_{0y}\sigma_{1z}\rangle_{\tilde{\rho}_{U_k}^{[2]}}\Big), \end{aligned} \tag{4.24}$$

where, $\sigma_{0x} = \sigma_x \otimes \mathbb{1}$ and $\sigma_{0x}\sigma_{1z} = \sigma_x \otimes \sigma_z$, for example.

### 4.4.1 Reconstruction algorithm

Before proceeding further, for clarity and consistency, we present a set of important terms and their corresponding explicit and shorthand descriptions in Table 4.5. These terms will be consistently used in the text from now on. The table also cross-references equations for corresponding definitions.

As discussed in Sec. 4.2, in the case of a single-qubit system ($N = 1$), the index $k$ ranges from 1 to 4, representing the different rotations: $\mathcal{G}_1^{[1]} = \sigma_x$, $\mathcal{G}_2^{[1]} = \sigma_y$, $\mathcal{G}_3^{[1]} = \sigma_z$, and $\mathcal{G}_4^{[1]} = \mathbb{1}$. The resulting rank $j = 0$ and $j = 1$ droplet functions corresponding to the scaled process $U_k^{[1]}$ are experimentally measured using Eq. 4.24. For simplicity, we combine these two droplet functions, i.e.,

$$f_k = f_{0,k}^{(\emptyset)} + f_{1,k}^{(1)}. \tag{4.25}$$

For simplicity and to keep a consistent droplet color, we use $\hat{U}_k^{[1]}$ defined in Eq. 4.16 (also see Table 4.4) which modifies the experimental droplet functions as follows:

$$\begin{aligned} \hat{f}_1 &= i(f_{0,1}^{(\emptyset)} + f_{1,1}^{(1)}) = if_1 \longleftrightarrow \hat{U}_1^{[1]} \approx AU_a^{[1]} \\ \hat{f}_2 &= i(f_{0,2}^{(\emptyset)} + f_{1,2}^{(1)}) = if_2 \longleftrightarrow \hat{U}_2^{[1]} \approx BU_a^{[1]} \\ \hat{f}_3 &= i(f_{0,3}^{(\emptyset)} + f_{1,3}^{(1)}) = if_3 \longleftrightarrow \hat{U}_3^{[1]} \approx CU_a^{[1]} \\ \hat{f}_4 &= f_{0,4}^{(\emptyset)} + f_{1,4}^{(1)} = f_4 \longleftrightarrow \hat{U}_4^{[1]} \approx DU_a^{[1]}, \end{aligned} \tag{4.26}$$

**Table 4.5:** Table containing essential terms with their explicit description, shorthand names, and symbols for the terminology used in the reconstruction algorithm (see Algo. 4.1). The table also cross-references equations for corresponding definitions.

| Explicit Description | Shorthand Name | Symbol |
|---|---|---|
| Matrix form of actual unitary process | Actual process | $U_a$ |
| Droplet of actual unitary process $U_a$ | Actual process droplet | $f_a$ |
| $\mathcal{G}$-dependent scaled process matrices. Where $\mathcal{G}_k^{[1]} \in \{\sigma_x, \sigma_y, \sigma_z, \mathbb{1}\}$, with $k = 1:4$. See Eq. 4.16 and Table 4.4. | Scaled matrices | $\hat{U}_k$ |
| $\mathcal{G}$-dependent experimental scaled process droplets of $\hat{U}_k$. See Eq. 4.26 | Scaled droplets | $\hat{f}_k$ |
| Weighted process droplets using matched filtering. See step 3 of Algo. 4.1. | Weighted droplets | $\hat{f}_{w,k}$ |
| Combined weighted process droplets. See step 4 of Algo. 4.1. | Combined droplets | $\hat{f}_{\text{comb}}$ |
| Estimated unitary process matrix form of $\hat{f}_{\text{comb}}$. See Sec. C.2 | Estimated process matrix | $U_{\text{est}}$ |
| Droplet of estimated unitary process matrix $U_{\text{est}}$ | Estimated process droplet | $f_{\text{est}}$ |
| Guess unitary process matrix | Guess process | $U_{\text{gue}}$ |
| Droplet of guess unitary process matrix | Guess process droplet | $f_{\text{gue}}$ |

where $U_a^{[1]}$ is the actual (experimental) unknown process composed of quaternions $A$, $B$, $C$, and $D$ as described in Eq. 4.15.

Now, the goal here is to reconstruct a spherical droplet with a high signal-to-noise ratio corresponding to an unknown process from the scaled droplets $\hat{f}_k$ described in Eq. 4.26. Let's consider the example shown in Fig. 4.10. The actual process matrix $U_a$ is composed of the quaternions $A = -0.5198$, $B = 0.3462$, $C = 0.7424$, and $D = -0.2425$. The corresponding droplet $f_a$ is depicted in the left panel of Fig. 4.10. The middle panel of Fig. 4.10 shows the tomographed scaled droplets: (a) $\hat{f}_1$, (b) $\hat{f}_2$, (c) $\hat{f}_3$, and (d) $\hat{f}_4$. A naive way to combine the scaled droplets $\hat{f}_k$ to reconstruct an estimate of

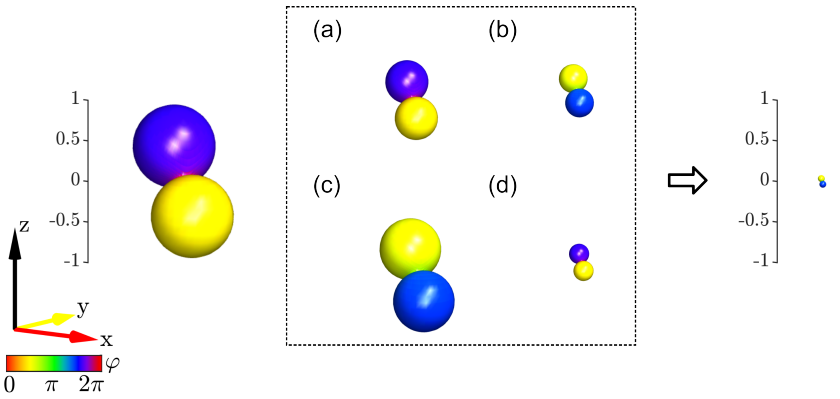


**Figure 4.10:** The illustration demonstrates a naive approach to reconstruct the unknown process droplet $\hat{f}_a$ from scaled process droplets $\hat{f}_k$ by calculating an average of the scaled droplets. The left panel displays a spherical droplet $f_a$ representing a process matrix $U_a^{[1]}$ with quaternion components $A = 0.5198$, $B = -0.3462$, $C = -0.7424$, and $D = 0.2425$. The middle panel exhibits the resulting tomographed scaled process droplets: (a) $\hat{f}_1$, (b) $\hat{f}_2$, (c) $\hat{f}_3$, and (d) $\hat{f}_4$. The right panel shows a combined droplet $\hat{f}_{\text{comb}}$ obtained by computing an average of the scaled process droplets in the middle panel. This naive approach does not lead to a droplet with a high signal-to-noise ratio.

actual spherical droplet function $f_a$ is by simply computing the average of the scaled droplets $\hat{f}_k$, such that $\hat{f}_{\text{comb}} = \frac{1}{4}(\hat{f}_1 + \hat{f}_2 + \hat{f}_3 + \hat{f}_4)$. The resulting combined droplet $\hat{f}_{\text{comb}}$ is illustrated in the right panel of Fig. 4.10.

However, this naive approach does not lead to a droplet with a high signal-to-noise ratio. This is due to the opposite signs of the scaled droplets $\hat{f}_k$, which results in partial cancellation of droplet functions. Hence, a more sophisticated approach is required to effectively combine the scaled process droplets $\hat{f}_k$ to reconstruct the unknown process with a high signal-to-noise ratio. To address this, we adopt the principle of matched filtering [62, 63]. This technique maximizes the signal-to-noise ratio of the reconstructed droplet by combining scaled droplets with different weights. Specifically, it assigns a higher weight to the droplet with a larger signal (size) and a lower weight to the

droplet with a smaller signal (size). This allows a combination of droplets with different weights, resulting in a reconstructed droplet with a significantly improved signal-to-noise ratio compared to the naive equal-weighted droplet combination approach depicted in Fig. 4.10. Here, we present an approach to estimate quaternions $A$, $B$, $C$, and $D$ from experimental scaled droplets $\hat{f}_k$ to reconstruct the unknown process with high signal-to-noise ratio. We first outline the steps of the algorithm for a single system qubit ($N = 1$) and subsequently elaborate on them through an example.

**Algorithm 4.1** Estimation of quaternions from experimental scaled droplets $\hat{f}_k$. See Table 4.5 for descriptions of the symbols used here.

**Aim**: To estimate quaternions $A$, $B$, $C$, and $D$ corresponding to an actual unknown process $U_a^{[1]}$ from experimental scaled droplets $\hat{f}_k$.

**Input**: Experimentally tomographed droplet functions $\hat{f}_k$ representing scaled processes $\hat{U}_k^{[1]}$, with $k = 1 : 4$.

1: Compute a correlation matrix $M$.
2: Estimate zero-order (i.e., iteration number $i = 0$) values of quaternions $A_i$, $B_i$, $C_i$, and $D_i$ from the correlation matrix $M$.
3: Compute weighted droplets: $\hat{f}_{w,1}^{[i]} = A_i\hat{f}_1$, $\hat{f}_{w,2}^{[i]} = B_i\hat{f}_2$, $\hat{f}_{w,3}^{[i]} = C_i\hat{f}_3$, and $\hat{f}_{w,4}^{[i]} = D_i\hat{f}_4$.
4: Combine the weighted droplet functions: $\hat{f}_{\text{comb}}^{[i]} = \hat{f}_{w,1}^{[i]} + \hat{f}_{w,2}^{[i]} + \hat{f}_{w,3}^{[i]} + \hat{f}_{w,4}^{[i]}$.
5: Estimate a unitary matrix $U_{\text{est},i}$ from the combined droplet function $\hat{f}_{\text{comb}}^{[i]}$.
6: Estimate new quaternions $A_{i+1}$, $B_{i+1}$, $C_{i+1}$, and $D_{i+1}$ from $U_{\text{est},i}$.
7: Input new values of quaternions $A_{i+1}$, $B_{i+1}$, $C_{i+1}$, and $D_{i+1}$ into Step 3.

**Termination**: Repeat Steps 3 to 7 until the change in quaternion values over iterations is not significant.

**Output**: Estimated droplet function $f_{\text{est}}$ representing a unitary process $U_{\text{est}}$.

Before delving into the algorithm itself, we first discuss the key steps it involves: computing a correlation matrix (step 2) and performing a weighted combination of droplets (step 4).

#### Correlation matrix

Given the experimental scaled droplet functions $\hat{f}_1$, $\hat{f}_2$, $\hat{f}_3$, and $\hat{f}_4$, the correlation matrix $M$ can be computed as follows:

$$M = \begin{bmatrix} \langle\hat{f}_1|\hat{f}_1\rangle & \langle\hat{f}_1|\hat{f}_2\rangle & \langle\hat{f}_1|\hat{f}_3\rangle & \langle\hat{f}_1|\hat{f}_4\rangle \\ \langle\hat{f}_2|\hat{f}_1\rangle & \langle\hat{f}_2|\hat{f}_2\rangle & \langle\hat{f}_2|\hat{f}_3\rangle & \langle\hat{f}_2|\hat{f}_4\rangle \\ \langle\hat{f}_3|\hat{f}_1\rangle & \langle\hat{f}_3|\hat{f}_2\rangle & \langle\hat{f}_3|\hat{f}_3\rangle & \langle\hat{f}_3|\hat{f}_4\rangle \\ \langle\hat{f}_4|\hat{f}_1\rangle & \langle\hat{f}_4|\hat{f}_2\rangle & \langle\hat{f}_4|\hat{f}_3\rangle & \langle\hat{f}_4|\hat{f}_4\rangle \end{bmatrix}. \tag{4.27}$$

Here, each element of the matrix can be computed using Eq. 2.16. The matrix $M$ provides correlations between different droplet functions, allowing for the zero-order (i.e., iteration $i = 0$) estimation of the quaternions. The absolute values of zero-order ($i = 0$) estimates of quaternions $A$, $B$, $C$, and $D$ can be determined from the diagonal elements of $M$:

$$\begin{aligned} |A_0| &= \sqrt{M(1,1)}, \\ |B_0| &= \sqrt{M(2,2)}, \\ |C_0| &= \sqrt{M(3,3)}, \\ |D_0| &= \sqrt{M(4,4)}. \end{aligned} \tag{4.28}$$

The relative signs of the zero-order ($i = 0$) quaternions $A_0, B_0, C_0$, and $D_0$ can be determined based on the signs of the off-diagonal elements of the matrix $M$. For example, one possible case of $M$ could be:

$$M = \begin{bmatrix} \langle \hat{f}_1 | \hat{f}_1 \rangle & \langle \hat{f}_1 | \hat{f}_2 \rangle & \langle \hat{f}_1 | \hat{f}_3 \rangle & \langle \hat{f}_1 | \hat{f}_4 \rangle \\ \langle \hat{f}_2 | \hat{f}_1 \rangle & \langle \hat{f}_2 | \hat{f}_2 \rangle & \langle \hat{f}_2 | \hat{f}_3 \rangle & \langle \hat{f}_2 | \hat{f}_4 \rangle \\ \langle \hat{f}_3 | \hat{f}_1 \rangle & \langle \hat{f}_3 | \hat{f}_2 \rangle & \langle \hat{f}_3 | \hat{f}_3 \rangle & \langle \hat{f}_3 | \hat{f}_4 \rangle \\ \langle \hat{f}_4 | \hat{f}_1 \rangle & \langle \hat{f}_4 | \hat{f}_2 \rangle & \langle \hat{f}_4 | \hat{f}_3 \rangle & \langle \hat{f}_4 | \hat{f}_4 \rangle \end{bmatrix}.$$

Here, the color of each matrix element corresponds to its respective sign. The red color indicates a positive sign, whereas the green color indicates a negative sign. In the presented case, assuming $D_0$ is positive, the quaternions $A_0$ and $B_0$ are positive, while $C_0$ is negative. Using the approach developed based on these conditions, the signs of the quaternions can be determined.

**Weighted combination of droplets**

Computing a weighted combination of experimental droplets $\hat{f}_k$ in step 3 is based on the principle of matched filtering [62, 63], as discussed before and is a key step of the reconstruction algorithm. In this step, for an iteration $i$, the weighted scaled droplet functions $\hat{f}_k$ are combined as described in Step 4 of Algo. 4.1, such that

$$\begin{aligned} \hat{f}^{[i]}_{\text{comb}} &= \hat{f}^{[i]}_{w,1} + \hat{f}^{[i]}_{w,2} + \hat{f}^{[i]}_{w,3} + \hat{f}^{[i]}_{w,4} \\ &= A_i \hat{f}_1 + B_i \hat{f}_2 + C_i \hat{f}_3 + D_i \hat{f}_4. \end{aligned} \tag{4.29}$$

Where $A_i$, $B_i$, $C_i$, and $D_i$ are the estimated quaternions in iteration $i$. The actual unknown process $U_a$ is composed of quaternions $A$, $B$, $C$, and $D$ (see Eq. 4.15), and $f_a$ is the spherical droplet corresponding to it, such that, $\hat{f}_1 = Af_a$, $\hat{f}_2 = Bf_a$, $\hat{f}_3 = Cf_a$, and $\hat{f}_4 = Df_a$ (see Eq. 4.26). After substituting these transformation, Eq. 4.29 takes the form:

$$\hat{f}^{[i]}_{\text{comb}} = A_i(Af_a) + B_i(Bf_a) + C_i(Cf_a) + D_i(Df_a), \tag{4.30}$$

Now, for a specific iteration $i$, if $A_i = A$, $B_i = B$, $C_i = C$, and $D_i = D$, the above equation becomes:

$$\hat{f}_{\text{comb}}^{[i]} = f_a, \tag{4.31}$$

where $A^2 + B^2 + C^2 + D^2 = 1$. Therefore, a combination of experimental droplets $\hat{f}_k$ with varying weights $A_i$, $B_i$, $C_i$, and $D_i$ provides a highly accurate estimate of the actual droplet function $f_a$. Additionally, if these weights are the same as the actual quaternions, the resulting combined droplet $\hat{f}_{\text{comb}}^{[i]}$ equals the actual droplet function $f_a$, as shown in Eq. 4.31. In the next section, we present some examples of the reconstruction algorithm.

### 4.4.2 Examples of the reconstruction algorithm

**Example 1**

Here, we demonstrate the algorithm with a simulated example without noise with the quaternion values $A = 0.15$, $B = 0.35$, $C = 0.55$, and $D = 0.7433$. These specific quaternion values were deliberately chosen to illustrate scaling factors in Fig. 4.7. The algorithm takes the tomographed droplets $\hat{f}_k$ (see Eq. 4.26) representing scaled processes $\hat{U}_k^{[1]}$ as input, illustrated on the left panel of Fig 4.11.

In the first step, the algorithm computes a correlation matrix described in Eq. 4.27. The corresponding correlation matrix for this example is shown on the left side of the middle panel in Fig. 4.11. The color of the matrix describes the signs corresponding to the matrix elements, as indicated by the color bar. In this case, all the matrix elements have positive signs (i.e., color between yellowish-red and red), indicating that all the quaternions have the same signs. Assuming $D_0$ is to be positive, the quaternions $A_0$, $B_0$, and $C_0$ are also positive. The zero estimations (corresponding to iteration $i = 0$) computed using Eq. 4.28 are: $A_0 = 0.1498$, $B_0 = 0.3496$, $C_0 = 0.5493$, and $D_0 = 0.7424$.

In the third step, the zero estimations are multiplied with the input droplet functions, such that, $\hat{f}_{w,1}^{[0]} = A_0\hat{f}_1$, $\hat{f}_{w,2}^{[0]} = B_0\hat{f}_2$, $\hat{f}_{w,3}^{[0]} = C_0\hat{f}_3$, and $\hat{f}_{w,4}^{[0]} = D_0\hat{f}_4$. These *weighted* droplets $\hat{f}_{w,k}^{[0]}$ (shown on the right side of the middle panel in Fig 4.11) are combined in the fourth step, such that: $\hat{f}_{\text{comb}}^{[0]} = A_0\hat{f}_1 + B_0\hat{f}_2 + C_0\hat{f}_3 + D_0\hat{f}_4$. In the fifth step, a unitary process matrix $U_{\text{est},0}$ is estimated from the droplet function $\hat{f}_{\text{comb}}^{[0]}$ using the method described in Sec. C.2.

In the sixth step, we derive new quaternion estimates $A_1$, $B_1$, $C_1$, and $D_1$ from unitary matrix $U_{\text{est},0}$. The resulting output droplet, depicted in the rightmost panel of Fig. 4.11, represents the system just after one iteration ($i = 1$). After $i = 1$, the quaternion values are $A_1 = 0.15$, $B_1 = 0.35$, $C_1 = 0.55$, and $D_1 = 0.7433$, which matches with the target values up to numerical accuracy.

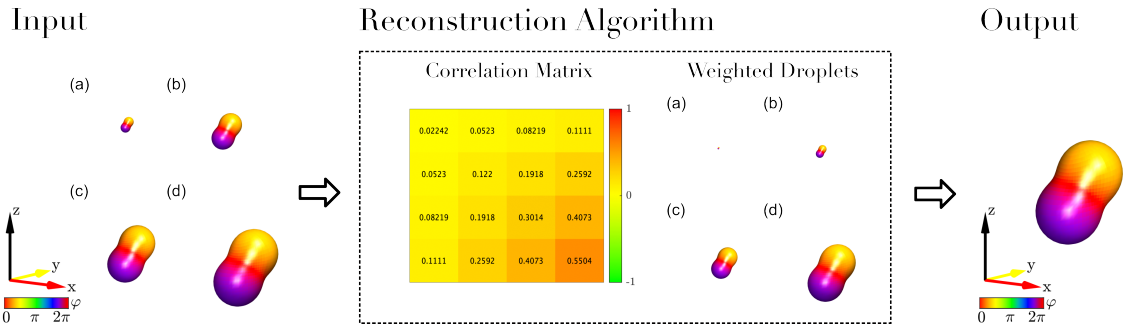


**Figure 4.11:** Illustration of the reconstruction of an unknown process droplet using the algorithm described in Algo. 4.1. In this example, no noise was considered. The algorithm takes as input tomographed scaled process droplets: (a)$\hat{f}_1$, (b)$\hat{f}_2$, (c)$\hat{f}_3$, and (d)$\hat{f}_4$ (see Eq. 4.26), displayed on the left panel. Inside the reconstruction algorithm (middle panel): first, a correlation matrix is computed (see Eq. 4.27), providing the zero-order estimates of quaternions $A_0$, $B_0$, $C_0$, and $D_0$ (see Eq. 4.28). These zero-order estimates are then multiplied with droplet functions, resulting in the weighted droplet functions: $\hat{f}^{[0]}_{w,1} = A_0\hat{f}_1$, $\hat{f}^{[0]}_{w,2} = B_0\hat{f}_2$, $\hat{f}^{[0]}_{w,3} = C_0\hat{f}_3$, and $\hat{f}^{[0]}_{w,4} = D_0\hat{f}_4$. The resulting droplet shown on the rightmost panel is obtained after the first iteration of the algorithm, and the corresponding quaternions match with the target values up to numerical accuracy.

### Example 2

In the above example, all the quaternions were positive. Now, we present an example with quaternion values $A = 0.5198$, $B = -0.3462$, $C = -0.7424$, and $D = 0.2425$, which was also discussed in Fig. 4.10. In this simulated example, no noise was considered. The corresponding reconstruction results are shown in Fig. 4.12.

In this case, the non-positive elements in the correlation matrix indicate that quaternions $B_0$ and $C_0$ are negative, assuming $D_0$ is positive. This is also evident from the input droplets, where the droplets of $\hat{f}_2$ and $\hat{f}_3$ are inverted compared to those of $\hat{f}_1$ and $\hat{f}_4$. The zero-order estimates of the quaternions are: $A_0 = 0.5192$, $B_0 = -0.3458$, $C_0 = -0.7415$, and $D_0 = 0.2422$. These zero-order estimates are then multiplied with droplet functions, resulting in the weighted droplets $\hat{f}^{[0]}_{w,1} = A_0\hat{f}_1$, $\hat{f}^{[0]}_{w,2} = B_0\hat{f}_2$, $\hat{f}^{[0]}_{w,3} = C_0\hat{f}_3$, and $\hat{f}^{[0]}_{w,4} = D_0\hat{f}_4$. The corresponding droplets are displayed on the right side of the middle panel in Fig. 4.12. Here, the droplets of (b) $\hat{f}^{[0]}_{w,2}$ and (c) $\hat{f}^{[0]}_{w,3}$ are inverted due to the sign of the estimated quaternions $B_0$ and $C_0$. These weighted droplets $\hat{f}^{[0]}_{w,k}$ are combined to form $\hat{f}^{[0]}_{\text{comb}} = A_0\hat{f}_1 + B_0\hat{f}_2 + C_0\hat{f}_3 + D_0\hat{f}_4$. In the next step, a unitary process matrix $U_{\text{est},0}$ is estimated from $\hat{f}^{[0]}_{\text{comb}}$, from which the quaternions $A_1$, $B_1$, $C_1$, and $D_1$ are derived. The resulting output droplet shown in the rightmost panel of Fig. 4.12 is obtained after one iteration, i.e., $i = 1$, with corresponding quaternion values of $A_1 = 0.5198$, $B_1 = -0.3462$, $C_1 = -0.7424$, and $D_1 = 0.2425$. These final

values match the target values up to numerical accuracy.

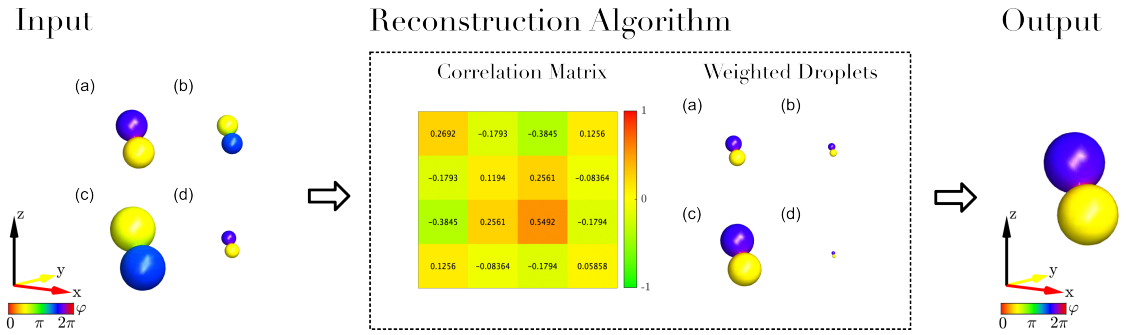


**Figure 4.12:** Illustration of the reconstruction of an unknown process droplet from scaled process droplets with different quaternion signs. The algorithm takes as input tomographed scaled process droplets: (a)$\hat{f}_1$, (b)$\hat{f}_2$, (c)$\hat{f}_3$, and (d)$\hat{f}_4$ (see Eq. 4.26), displayed on the left panel. The zero-order estimate of the quaternions is obtained from the correlation matrix, and these are multiplied with droplet functions, resulting in weighted droplets: $\hat{f}^{[0]}_{w,1} = A_0\hat{f}_1$, $\hat{f}^{[0]}_{w,2} = B_0\hat{f}_2$, $\hat{f}^{[0]}_{w,3} = C_0\hat{f}_3$, and $\hat{f}^{[0]}_{w,4} = D_0\hat{f}_4$. The resulting output droplet shown on the rightmost panel is obtained after the first iteration of the algorithm.

Now, we present an example that contains noise in the tomographed (input) droplets. In this example, we considered noise due to the limited number of shots (shot noise).

**Example 3**

Here, we illustrate the reconstruction algorithm with an example that includes shot noise. The initial configuration for this example is the same as the one presented in example 1 (see Fig. 4.11), i.e., $A = 0.15$, $B = 0.35$, $C = 0.55$, and $D = 0.7433$, but it is simulated with $N_s = 500$ shots to introduce shot noise. The reconstruction results are displayed in Fig. 4.13. The zero-order estimates of quaternions from the correlation matrix, in this case, are $A_0 = 0.1899$, $B_0 = 0.3627$, $C_0 = 0.5575$, and $D_0 = 0.7440$. The algorithm was terminated after $i = 3$ iterations, as the change in the values of quaternions over iterations was not significant, as shown in the left panel of Fig. 4.14. The resultant quaternion values after termination are: $A_3 = 0.1502$, $B_3 = 0.3414$, $C_3 = 0.5504$, and $D_3 = 0.7423$. The corresponding reconstructed droplet is presented in the rightmost panel of Fig. 4.13.

In these simulations, since we know the actual unknown process $U_a$, we can quantify the closeness of the reconstructed process to the actual process using the process fidelity definition in Eq. 3.11. The fidelity of the reconstructed process is plotted with respect to iterations in the right panel of Fig. 4.14. The fidelity of the reconstructed process droplet, as shown in the right panel of Fig. 4.13, is 0.9999. Note that in these examples an equiangular grid of 25 polar angles $\beta \in \{0, \frac{\pi}{24}, \ldots, \pi\}$ and 49 azimuthal angles $\alpha \in \{0, \frac{2\pi}{48}, \ldots, 2\pi\}$ was chosen for scanning, resulting in very high reconstructed fidelity.

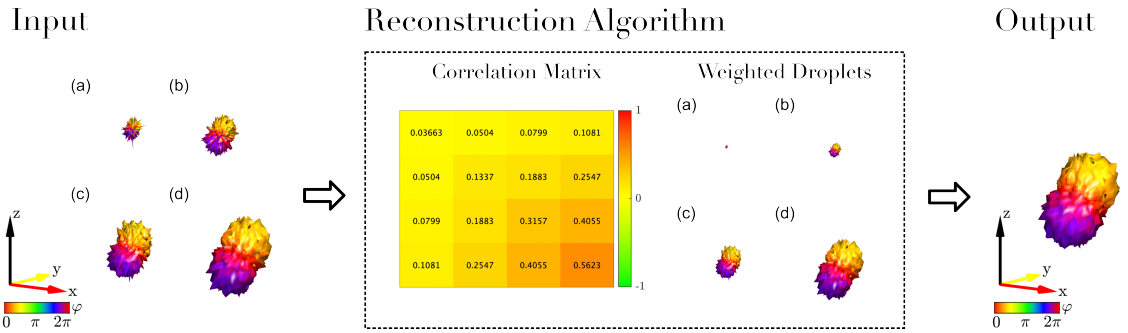


**Figure 4.13:** Illustration of the reconstruction of an unknown process from the tomographed droplets with shot noise. The tomographed scaled process droplets: (a) $\hat{f}_1$, (b) $\hat{f}_2$, (c) $\hat{f}_3$, and (d) $\hat{f}_4$ are displayed on the left panel. The zero-order estimates of quaternions are obtained from the correlation matrix, and these are multiplied with droplet functions $\hat{f}_k$ to obtain weighted droplets shown on the right of the middle panel. The resulting output droplet on the rightmost panel corresponds to the process with quaternions $A_3 = 0.1502$, $B_3 = 0.3414$, $C_3 = 0.5504$, and $D_3 = 0.7423$, obtained after $i = 3$ iterations with a fidelity of 0.9999.

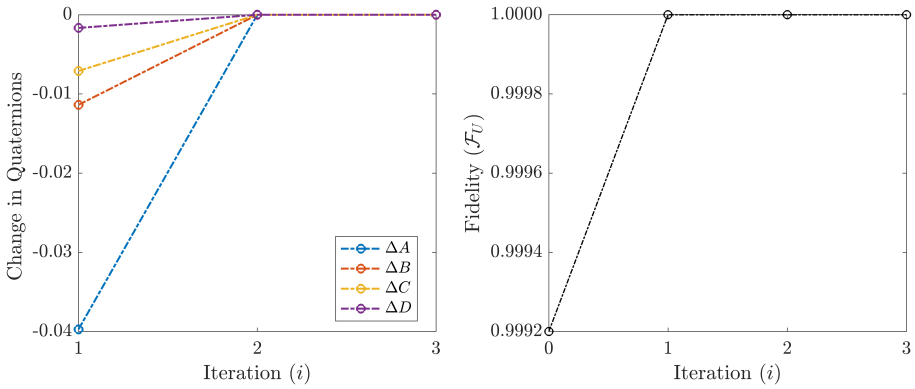


**Figure 4.14:** Plot of change in the values of quaternions with iteration (on the left panel) and fidelity ($\mathcal{F}_U$) with iteration (on the right panel) for the reconstruction example illustrated in Fig. 4.13. The change in quaternion values over iteration is computed using $\Delta A = A_{i+1} - A_i$, for example.

A study of fidelity as a function of different numbers of shots is also performed, and the results are discussed in Sec. 4.5.

### Example 4

We demonstrate the reconstruction algorithm with another example containing shot noise in Fig. 4.15. Here, the initial configuration is the same as the one presented in example 2 (see Fig. 4.12), but it is simulated with $N_s = 300$. In this case, the non-positive elements of the correlation matrix indicate that the quaternions $B_0$ and

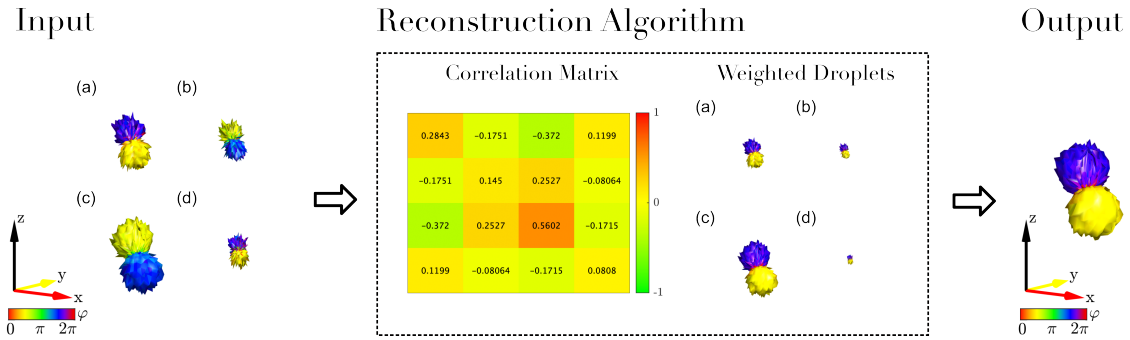


**Figure 4.15:** Illustration of reconstruction of an unknown process from the tomographed droplets with shot noise using the algorithm presented in Algo. 4.1. The tomographed scaled process droplets: (a) $\hat{f}_1$, (b) $\hat{f}_2$, (c) $\hat{f}_3$, and (d) $\hat{f}_4$ are shown on the left. The zero-order estimates are obtained from the correlation matrix, which is used to compute the weighted droplets. The resulting output droplet on the rightmost panel corresponds to the process with quaternions $A_3 = 0.5196$, $B_3 = -0.3443$, $C_3 = -0.7416$, and $D_3 = 0.2479$, obtained after $i = 3$ iterations with a fidelity of 0.9999.

$C_0$ are negative. The zero-order ($i = 0$) estimates are: $A_0 = 0.5272$, $B_0 = -0.3765$, $C_0 = -0.7401$, and $D_0 = 0.2811$. These zero-order estimates are multiplied with droplet functions $\hat{f}_k$ to obtain weighted droplets $\hat{f}^{[0]}_{w,1} = A_0\hat{f}_1$, $\hat{f}^{[0]}_{w,2} = B_0\hat{f}_2$, $\hat{f}^{[0]}_{w,3} = C_0\hat{f}_3$, and $\hat{f}^{[0]}_{w,4} = D_0\hat{f}_4$. The resultant weighted droplets are plotted on the right of the middle panel.

The algorithm was terminated after $i = 3$ iterations due to a non-significant change in the values of quaternions over iterations, as shown in the left panel of Fig. 4.16. The resulting quaternions obtained after termination are: $A_3 = 0.5196$, $B_3 = -0.3443$, $C_3 = -0.7416$, and $D_3 = 0.2479$, with a process fidelity of 0.9999. The plot of process fidelity $\mathcal{F}_U$ with iteration $i$ is shown in the right panel of Fig. 4.16.

### 4.4.3 Reconstruction algorithm with optimization

As demonstrated using the examples above, the reconstruction algorithm offers a reliable estimate of the quaternions. However, while this approach is powerful, it does not ensure the optimal solution. In this section, we elaborate on combining the reconstruction algorithm with an optimization routine and discuss the benefits gained from this integrated approach.

We use the zero-order estimates (corresponding to $i = 0$) of quaternions $A_0$, $B_0$, $C_0$, and $D_0$ obtained from the correlation matrix as an initial guess for the optimization to minimize the following cost function:

$$J = ||\hat{U}_1 - A_i U_{\text{est},i}||^2 + ||\hat{U}_2 - B_i U_{\text{est},i}||^2 + ||\hat{U}_3 - C_i U_{\text{est},i}||^2 + ||\hat{U}_4 - D_i U_{\text{est},i}||^2. \quad (4.32)$$

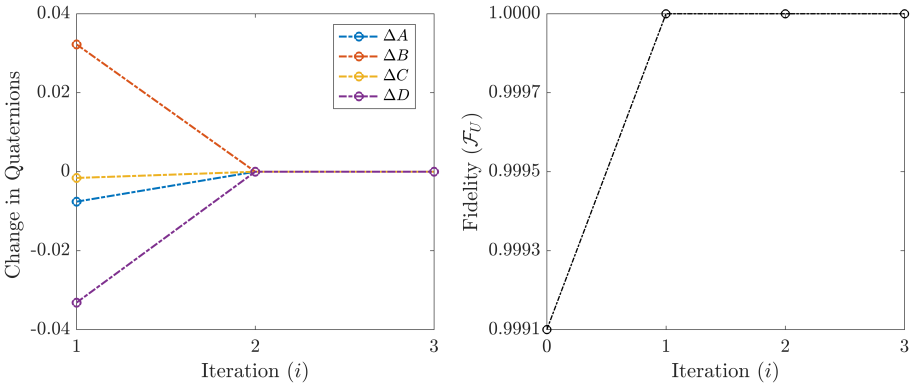


**Figure 4.16:** Plot of change in the values of quaternions with iteration (on the left panel) and plot of fidelity ($\mathcal{F}_U$) with iteration (on the right panel) for the reconstruction example illustrated in Fig. 4.15. Where change in quaternion value over iteration is computed using $\Delta A = A_{i+1} - A_i$, for example.

Here, $\hat{U}_1$, $\hat{U}_2$, $\hat{U}_3$, and $\hat{U}_4$ are scaled matrices, i.e., the matrix representations of the scaled droplet functions $\hat{f}_1$, $\hat{f}_2$, $\hat{f}_3$, and $\hat{f}_4$, respectively, as described in Table 4.5. The process matrix estimation from the droplet functions can be derived using the approach described in Sec. 3.3. $A_i$, $B_i$, $C_i$, and $D_i$ are the quaternions estimated in iteration $i$. The operator $U_{\text{est},i}$ represents the estimated unitary process matrix for iteration $i$, composed of quaternions $A_i$, $B_i$, $C_i$, and $D_i$, as defined in Eq. 4.15. The cost function $J$ quantifies the closeness of the estimated process matrix to the experimentally obtained scaled process matrices. To minimize this cost function, we utilize the gradient-based optimization function, `fminunc` in Matlab.

Here, we provide an example to showcase the reconstruction algorithm with optimization and compare it with the one without optimization. We chose an example with quaternions $A = 1$ and $B = C = D = 0$. The scaled tomographed droplets depicted in the left panel of Fig. 4.17 are obtained after $N_s = 500$ shots. The zero-order estimates computed from the correlation matrix, assuming $D_0$ is positive, are $A_0 = 0.9899$, $B_0 = -0.1305$, $C_0 = -0.1230$, and $D_0 = 0.1211$. These zero-order estimates are used as an initial guess for the optimization. The fidelity ($\mathcal{F}_U$) per iteration is shown in the right panel of Fig. 4.17 for both approaches, i.e., with and without optimization.
The quaternions estimated after the final iteration ($i = 5$) without optimization are: $A_5 = 0.99998$, $B_5 = 0.0017$, $C_5 = 0.0042$, and $D_5 = 0.0038$. Whereas, the quaternions estimated after the final iteration ($i = 21$) with optimization are: $A_{21}^{\text{opt}} = 0.99999$, $B_{21}^{\text{opt}} = 0.0005$, $C_{21}^{\text{opt}} = 0.0011$, and $D_{21}^{\text{opt}} = 0.0022$. The optimization terminated after 21 iterations following the defined tolerance limit. However, in Fig. 4.17, only fidelity up to 5 iterations is displayed because the change in fidelity with iteration is not accurately visible in this scale. The process fidelity after the termination of the algorithm without optimization is 0.99998, whereas with optimization is 0.99999. The cost function with

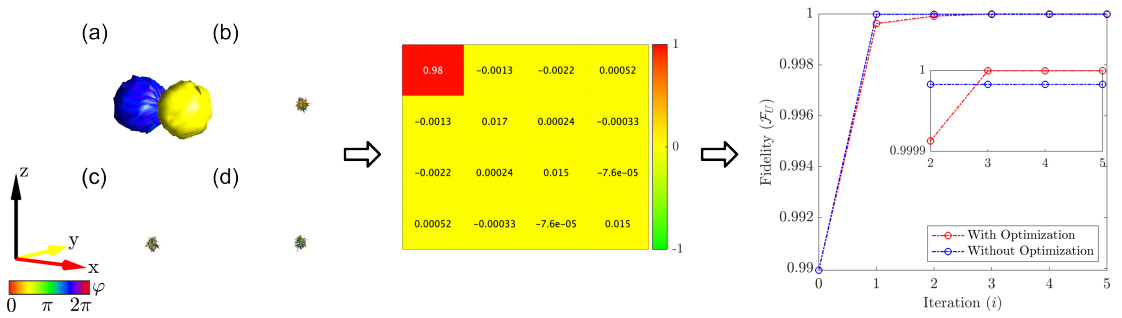


**Figure 4.17:** Illustration of the reconstruction algorithm with and without optimization. The algorithms take as input tomographed scaled process droplets: (a) $\hat{f}_1$, (b) $\hat{f}_2$, (c) $\hat{f}_3$, and (d) $\hat{f}_4$ (see Eq. 4.26), displayed on the left panel. The zero-order estimates of the quaternions are used as an initial guess to minimize the cost function $J$ given in Eq. 4.32. The fidelity with and without optimizations are shown in the right panel. The inset figure shows the variation of fidelity for iterations 2 to 5 between 0.9999 and 1. The plot of cost for this case is shown in the Fig. 4.18.

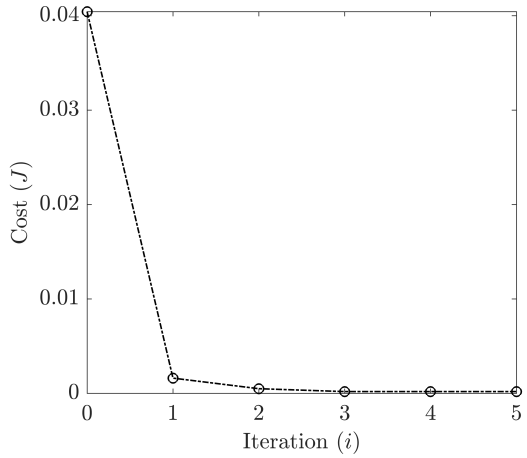


**Figure 4.18:** Illustration of cost function ($J$) used in the optimization (See Eq. 4.32) with iteration ($i$) for the case considered in Fig. 4.17.

iteration for optimization is shown in Fig. 4.18. Although the gain in fidelity in this case is very small, this shows that optimization does improve the estimation of the quaternions. In the following section, we provide the result of an extensive numerical study to compare both approaches.

## 4.5 Numerical study of reconstruction algorithm

To evaluate the performance of the reconstruction algorithm with and without optimization, we conducted a numerical study. In this study, we compared the process

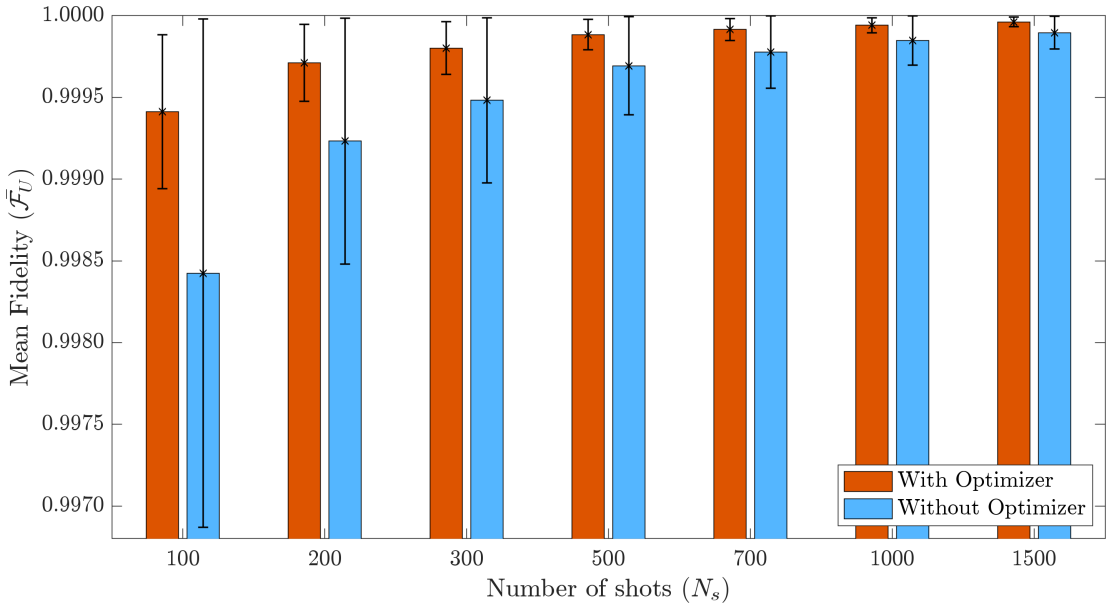


**Figure 4.19:** Plot of mean fidelity $\bar{\mathcal{F}}_U$ with different number of shots $N_s$ for reconstruction algorithm approach with and without optimizer. The mean is computed over 50 noise instances for 100 random gates for each $N_s$. The standard deviation for each $N_s$ is represented by the vertical bars.

fidelity $\mathcal{F}_U$ (see Eq. 3.11) of the reconstructed process matrix with the target process matrix for different numbers of shots, denoted as $N_s$. The Lebedev sampling scheme with 50 grid points [34] was employed for scanning purposes, and this same scheme was utilized in the experiments presented in the next section. For each value of $N_s$, 100 random gates were generated, and for each of these gates, 50 different noise instances were created. The mean and standard deviation of the process fidelity were computed using both approaches. The plot depicting the mean fidelity ($\bar{\mathcal{F}}_U$) for both approaches with different numbers of shots ($N_s$), is shown in Fig. 4.19. The plot also includes the standard deviation for each approach, represented by vertical bars across varying numbers of shots. The plot indicates that the approach with the optimization provides a gain in the reconstructed fidelity, and the standard deviation for the approach using optimization is smaller in comparison to the approach without optimization. This study only considered noise due to the limited number of shots.

## 4.6 Experimental implementation of Wigner tomography for unknown processes

In this section, we describe the details for experimentally implementing Wigner process tomography for unknown processes. We present experimental results for a single system qubit, i.e., $N = 1$ performed on an IBM quantum device for a pure state on an individual,

well-defined quantum system. The quantum circuits presented here are general and can be directly used on any circuit-based quantum computer.

### 4.6.1 Single qubit

For the Wigner tomography of a single-qubit unknown process, three qubits are required ($q_0$, $q_1$, $q_1^a$). Here, $q_1$ is a system qubit, and $q_0$ and $q_1^a$ are ancilla qubits. The spherical droplet functions $f_{0,k}^{(\emptyset)}$ and $f_{1,k}^{(1)}$ corresponding to scaled process matrices $U_k^{[1]}$ for different controlled rotations $\mathcal{G}_k \in \{\mathbb{1}, \sigma_x, \sigma_y, \sigma_z\}$, can be tomographed by combining the experimentally measured expectation values for a set of scanning angles $\beta$ and $\alpha$, as expressed in Eq. 4.24. The general quantum circuits for performing Wigner tomography are shown in Fig. 4.20. This figure explicitly highlights the four steps of the algorithm discussed in Sec. 4.3. Now, we explain these steps.

In the preparation step ($\mathcal{P}$), we initiate the control qubit $q_0$ in an equal superposition state using the Hadamard gate (H). To prepare qubits $q_1$ and $q_1^a$ in a maximally mixed state ($\rho_{mm}^{[2]} = \frac{1}{4}\mathbb{1}^{[2]}$), we employ the temporal averaging approach [56, 57] introduced in Sec. 4.6. This approach was initially introduced for a single qubit, and here, we extend it to prepare qubits $q_1$ and $q_1^a$ in a maximally mixed state. This extension involves repeating the experiment for the four computational basis states ($|00\rangle$, $|01\rangle$, $|10\rangle$, and $|11\rangle$) and averaging the measurement outcomes:

$$\rho_{mm}^{[2]} = \frac{1}{4}\mathbb{1}^{[2]} = \frac{1}{4}(|00\rangle\langle 00|) + \frac{1}{4}(|01\rangle\langle 01|) + \frac{1}{4}(|10\rangle\langle 10|) + \frac{1}{4}(|11\rangle\langle 11|). \tag{4.33}$$

The different computational basis states are created by applying NOT (X) gates in the circuits shown in Fig. 4.20, assuming that the initial state of all qubits is $|\psi_i\rangle = |000\rangle$. In these circuits, the state of qubits $q_1$ and $q_1^a$ after the preparation step is (a) $|00\rangle$, (b) $|01\rangle$, (c) $|10\rangle$, and (d) $|11\rangle$. Therefore, the (temporally) averaged expectation values of the circuits presented in Fig. 4.20 provide $\langle\sigma_{0x}\rangle$ and $\langle\sigma_{0x}\sigma_{1z}\rangle$ for a controlled rotation $\mathcal{G}_k$. The temporal averaging is discussed in detail in supplementary Sec. B.2.

In the mapping step ($\mathcal{M}$), we substitute the circuit presented in Fig. 4.5 for $N = 1$. For the scanning purpose in the rotation step ($\mathcal{R}$), the $U_3$ gate is employed to rotate the system qubit $q_1$ by an angle $\beta$ around the $y$ axis followed by a rotation of $\alpha$ around the $z$ axis. The $U_3$ gate used in these circuits is discussed in Sec. 1.1.3.

The circuits shown in Fig. 4.20 provide expectation values $\langle\sigma_{0x}\rangle$ and $\langle\sigma_{0x}\sigma_{1z}\rangle$ for a controlled rotation $\mathcal{G}_k$. The other required expectation values (see Eq. 4.24), $\langle\sigma_{0y}\rangle$ and $\langle\sigma_{0y}\sigma_{1z}\rangle$, are computed similarly by replacing $U_3(-\frac{\pi}{2}, 0, 0)$ with $U_3(\frac{\pi}{2}, 0, \frac{\pi}{2})$ in the detection-associated rotations step ($\mathcal{D}$). These additional circuits are not shown here. Hence, there are eight quantum circuits for each of the four rotations $\mathcal{G}_k \in \{\mathbb{1}, \sigma_x, \sigma_y, \sigma_z\}$, making it a total of 32 ($= 8 \times 4$) quantum circuits for tomography, which are evaluated

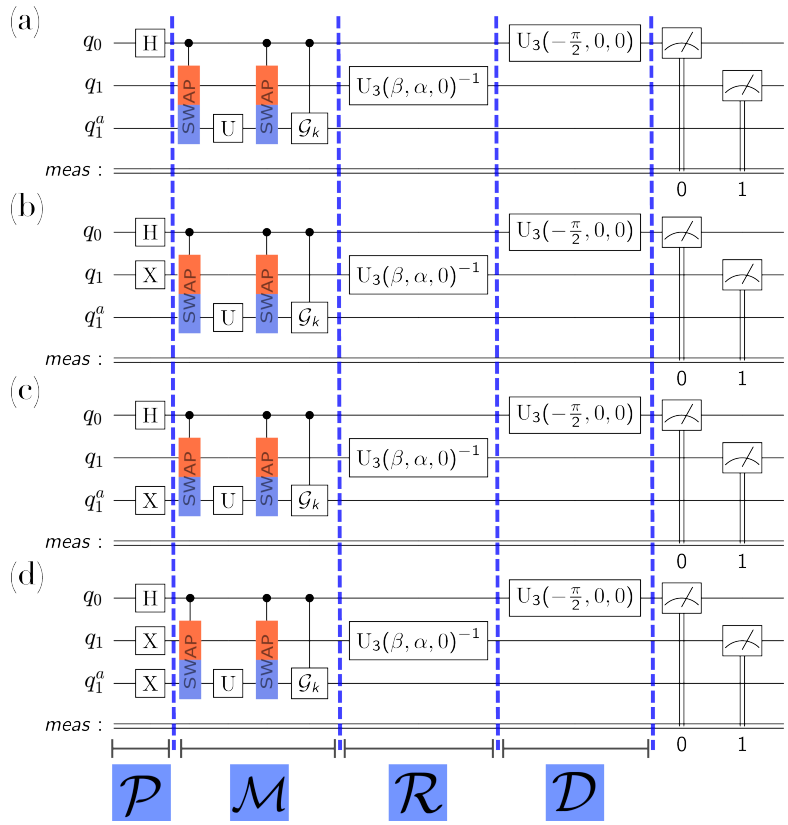


**Figure 4.20:** Quantum circuit set for performing tomography of a single qubit unknown process $U$. The initial state of the qubits is $|\psi_i\rangle = |000\rangle$. The four blocks of algorithm namely preparation ($\mathcal{P}$), mapping ($\mathcal{M}$), rotation ($\mathcal{R}$), and detection-associated rotations ($\mathcal{D}$) are shown here explicitly. The circuits shown here only measure expectation values $\langle\sigma_{0x}\rangle$ and $\langle\sigma_{0x}\sigma_{1z}\rangle$, therefore the number of circuit extends by replacing $\mathrm{U_3}(-\frac{\pi}{2},0,0)$ with $\mathrm{U_3}(\frac{\pi}{2},0,\frac{\pi}{2})$ to measure $\langle\sigma_{0y}\rangle$ and $\langle\sigma_{0y}\sigma_{1z}\rangle$. Each circuit is then repeated for different rotations $\mathcal{G}_k \in \{\mathbb{1},\sigma_x,\sigma_y,\sigma_z\}$ and scanning angles $\beta$ and $\alpha$. The $\mathrm{U_3}$ gate used in these circuits is discussed in Sec. 1.1.3.

for a set of scanning angles $\beta$ and $\alpha$. Now we discuss the implementation of these quantum circuits on an experimental device.

### Calibration experiments

Noise poses a critical challenge in the field of quantum computing, leading to errors that can significantly impact the performance and reliability of quantum computers. For implementing a quantum circuit on an experimental device, each quantum gate is decomposed into hardware native gates, which are then implemented using control pulses. Compared to the tomography experiments of known processes (c.f. Sec. 3.4.1), we observed two major experimental problems in the first implementations of the

tomography experiments for unknown processes:

(A) The experimentally measured expectation values were scaled down uniformly by about 50% compared to the simulated expectation values, resulting in a corresponding scaling of experimental droplet functions. (The experimental scaling mentioned here should not be confused with the scaling factor $\epsilon$ presented in Sec. 4.2.)

(B) Preliminary experiments showed a high fidelity of the (rescaled) tomographed droplet functions except for a relatively large rotation of the rank $j = 1$ droplet (which is not rotational symmetric) by about 20° around the $z$ axis, independent of the process of interest that was tomographed.

Problem (A) results from decoherence during the pair of relatively long CSWAP gates and experimental imperfections of a large number of single-qubit and two-qubit gates needed to implement the CSWAP gates. For instance, on IBM devices, a single CSWAP gate has an overall duration of several microseconds. It consists of about ten controlled two-qubit gates and about thirty single-qubit gates (the actual numbers depend on the actual device properties). The resulting uniform scaling of the experimentally measured droplet function is automatically taken into account by the normalization steps of the reconstruction algorithm (see Sec. 4.4.1). However, this additional scaling of the droplet reduces the signal-to-noise ratio of the tomography experiments, at least for noisy near-term quantum devices.

Problem (B) is also a result of the long duration of the CSWAP gates, which amplifies the effect of small detunings of the ancilla qubit $q_0$. In general, phase errors arise from the frequency detuning of the drive during the physical implementation of single and two-qubit gates, as discussed in Ref. [64]. This effect can be mitigated through calibration experiments. Preceding experiments of unknown processes with a simplified tomography experiment of an X (NOT) gate can be performed, which enables precise determination of this phase error by fitting phase-shifted sine and cosine functions to the data; see Figs. 4.21 and 4.22.

For quantifying the unwanted additional phase shift of qubit $q_0$, we used the calibration circuits shown in Fig. 4.21. These circuits are derived from the tomography circuits presented in Fig. 4.20, with $U = \mathrm{X}$ (NOT) gate, $c\mathcal{G} = c\mathrm{X}$ in the mapping block $\mathcal{M}$, scanning angles $\beta = \frac{\pi}{2}$ and $\alpha = 0$ in rotation block $\mathcal{R}$. An additional calibration block $\mathcal{C}$ is introduced here which consist of $\mathrm{U}_3(0, 0, \lambda)$ (corresponds to $RZ(\lambda)$) on qubit $q_0$. The $\mathcal{C}$ block is followed by a detection-associated rotation block $\mathcal{D}$ to experimentally estimate $\langle\sigma_{0x}\sigma_{1z}\rangle$ and $\langle\sigma_{0y}\sigma_{1z}\rangle$ from circuits (a) and (b), respectively. In this case where $U = \mathrm{X}$, the rank $j = 0$ droplet is zero, therefore, the expectation values $\langle\sigma_{0x}\rangle$ and $\langle\sigma_{0y}\rangle$ are zero for all scanning angles $\beta$ and $\alpha$. The preparation block $\mathcal{P}$ of both circuits in Fig. 4.21 corresponds to the preparation block shown in Fig. 4.20, i.e., applying

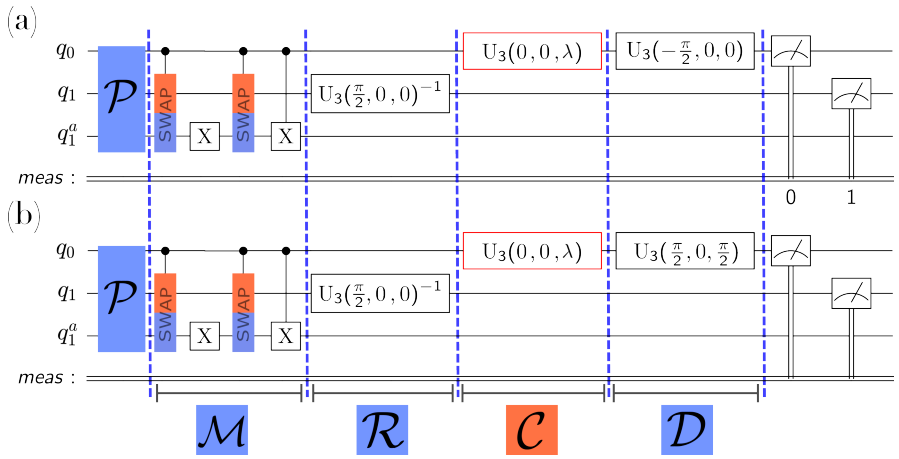


**Figure 4.21:** Circuits for performing calibration experiments to quantify the phase shift in qubit $q_0$. These circuits are adapted from the tomography circuits presented in Fig. 4.20. For both circuits, the $\mathcal{P}$ block is identical to the preparation block shown in Fig. 4.20. In comparison to the circuits shown in Fig. 4.20, here the mapping block $\mathcal{M}$ contains $U = \mathrm{X}$ (NOT) gate, $c\mathcal{G} = c\mathrm{X}$, and rotation block $\mathcal{R}$ has values $\beta = \frac{\pi}{2}$ and $\alpha = 0$. An additional calibration block $\mathcal{C}$ is introduced here, which consists of $\mathrm{U}_3(0,0,\lambda)$ (corresponds to $RZ(\lambda)$) on qubit $q_0$, followed by a detection-associated rotation block $\mathcal{D}$ to estimate $\langle\sigma_{0x}\sigma_{1z}\rangle$ and $\langle\sigma_{0y}\sigma_{1z}\rangle$ from circuits (a) and (b), respectively. See Fig. 4.22 for measurement results.

the Hadamard gate to prepare qubit $q_0$ in an equal superposition state and applying suitable NOT gates to prepare qubits $q_1$ and $q_1^a$ in a maximally mixed state using temporal averaging.

The calibration circuits shown in Fig. 4.21 are repeated for $RZ(\lambda)$ with $\lambda \in [0, 2\pi]$. The plot of the expectation values $\langle\sigma_{0x}\sigma_{1z}\rangle$ and $\langle\sigma_{0y}\sigma_{1z}\rangle$ as a function of angle $\lambda$ is shown in Fig. 4.22. The simulated plot in the bottom panel shows the ideal values of expectation values, whereas the expectation values in the top panel are obtained experimentally using `ibmq_mumbai` device. A plot of normalized experimental values is shown in the middle panel to provide a direct visual comparison with the experimental values in the bottom panel. The experimental expectation values have a phase shift of $\lambda_{\text{corr}} = 0.3473 (\approx 20°)$ radians compared to the simulated values. This phase shift corresponds to the unwanted extra rotation of qubit $q_0$. We compensate for this extra rotation of qubit $q_0$ in the tomography experiments by applying $-RZ(\lambda_{\text{corr}})$ on qubit $q_0$ right before the $\mathcal{D}$ (detection-associated rotation) block of circuits in Fig. 4.20.

### Experimental results

We experimentally implemented the tomography circuits depicted in Fig. 4.20 with an additional $-RZ(\lambda_{\text{corr}})$ rotation with $\lambda_{\text{corr}} = 0.3473$ radians, applied to qubit $q_0$ just before the $\mathcal{D}$ (detection-associated rotation) block on the `ibmq_mumbai` device. During

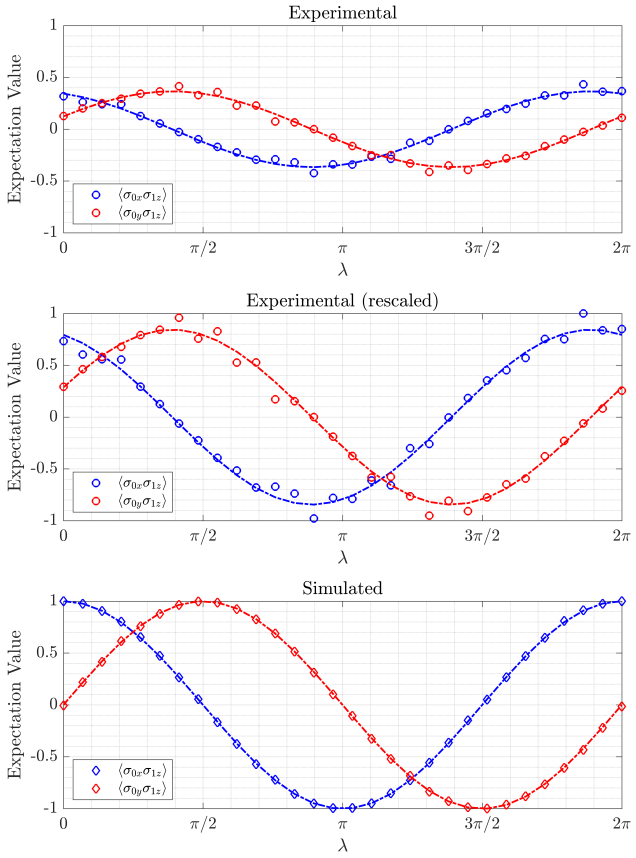


**Figure 4.22:** Experimental (top panel), rescaled experimental (middle panel), and simulated (bottom panel) plot of the expectation values $\langle\sigma_{0x}\sigma_{1z}\rangle$ and $\langle\sigma_{0y}\sigma_{1z}\rangle$ as a function of rotation around the $z$ axis with a rotation angle $\lambda$. The plot is an outcome of the calibration circuits presented in Fig. 4.21. The expectation values in the top panel are obtained experimentally using `ibmq_mumbai` device. The rescaled experimental values in the middle panel are plotted for a direct visual comparison with the simulated values.

these experiments, we employed a Lebedev $n = 50$ grid for scanning angles $\beta$ and $\alpha$, and each experiment was repeated for each grid point for $N_s = 4096$ shots.

The experimental results presented in Fig. 4.23 focus on the "unknown" process $U = \mathrm{X}$ (NOT) gate. The quaternion values associated with a NOT gate are $A = 1$ and $B = C = D = 0$. According to Table 4.4, ideally there is only one non-zero scaled process matrix $\hat{U}_k = \epsilon_k U$ for $k = 1$, corresponding to $\mathcal{G} = \sigma_x$ rotation. The actual droplet corresponding to the NOT gate and the reconstructed droplet from the experimental scaled droplets $\hat{f}_k$ are shown in **A** of Fig. 4.23. The simulated and experimental scaled process droplets $\hat{f}_k$ are shown in **B**, where (a) $\hat{f}_1$, (b) $\hat{f}_2$, (c) $\hat{f}_3$, and (d) $\hat{f}_4$. We show the corresponding expectation values in **C** of Fig. 4.23.

The reconstructed droplet shown in Fig. 4.23 is derived through the application of the reconstruction algorithm to the experimental scaled droplets $\hat{f}_k$. The initial estimations computed from the correlation matrix (see Fig. C.1) are $A_0 = 0.5802$, $B_0 = -0.1672$, $C_0 = 0.1075$, and $D_0 = 0.0631$. After employing the reconstruction algorithm with optimization, the final quaternion values are $A_{16}^{\text{opt}} = 0.9991$, $B_{16}^{\text{opt}} = 0.0090$, $C_{16}^{\text{opt}} = -0.0407$, and $D_{16}^{\text{opt}} = -0.0110$. The process fidelity achieved using the reconstruction algorithm with and without optimization is 0.9991 and 0.9935, respectively. The plot illustrating the cost and non-fidelity with optimization iterations, along with the correlation matrix, is presented in Fig. C.1.

Similarly, the experimental result for a $U = \text{Z}$ gate is presented in Fig. 4.24. The quaternion values associated with a Z gate are $C = 1$ and $A = B = D = 0$. Similar to the NOT gate, there is only one non-zero scaled scaled process matrix $\hat{U}_k$ for $k = 3$, corresponding to $\mathcal{G} = \sigma_z$ rotation (see Table 4.4). The reconstructed droplet shown in Fig. 4.24 is derived through the application of the reconstruction algorithm to the experimental scaled droplets $\hat{f}_k$. The initial estimations computed from the correlation matrix (see Fig. C.1) are $A_0 = 0.0543$, $B_0 = 0.0920$, $C_0 = 0.7886$, and $D_0 = 0.0740$. The quaternions obtained after employing reconstruction algorithm with optimization are $A_{15}^{\text{opt}} = -0.0023$, $B_{15}^{\text{opt}} = 0.0794$, $C_{15}^{\text{opt}} = 0.9966$, and $D_{15}^{\text{opt}} = 0.0210$. The process fidelity achieved using the reconstruction algorithm with and without optimization is 0.9966 and 0.9971, respectively. See Fig. C.2 for the plot illustrating the cost and non-fidelity with optimization iterations, along with the correlation matrix.

The experimental result for the $U = \text{H}$ (Hadamard) gate is presented in Fig. 4.25. The quaternion values associated with a Hadamard gate are $A = C = -0.7071$ and $B = D = 0$. In this case, there are two non-zero scaled process matrices $\hat{U}_k$ for $k = 1$ and $k = 3$ corresponding to $\mathcal{G} = \sigma_x$ and $\mathcal{G} = \sigma_z$, respectively (see Table 4.4). For the reconstruction algorithm, the initial guess computed from the correlation matrix is $A_0 = 0.3937$, $B_0 = 0.1868$, $C_0 = 0.4035$, and $D_0 = 0.0581$. The optimized quaternions after reconstruction algorithm are $A_{11}^{\text{opt}} = 0.6566$, $B_{11}^{\text{opt}} = 0.0172$, $C_{11}^{\text{opt}} = 0.7540$, and $D_{11}^{\text{opt}} = 0.089$. The process fidelity achieved using the reconstruction algorithm with and without optimization is 0.9974 and 0.9934, respectively. See Fig. C.3 for the plot illustrating the cost and non-fidelity with optimization iterations, along with the correlation matrix.

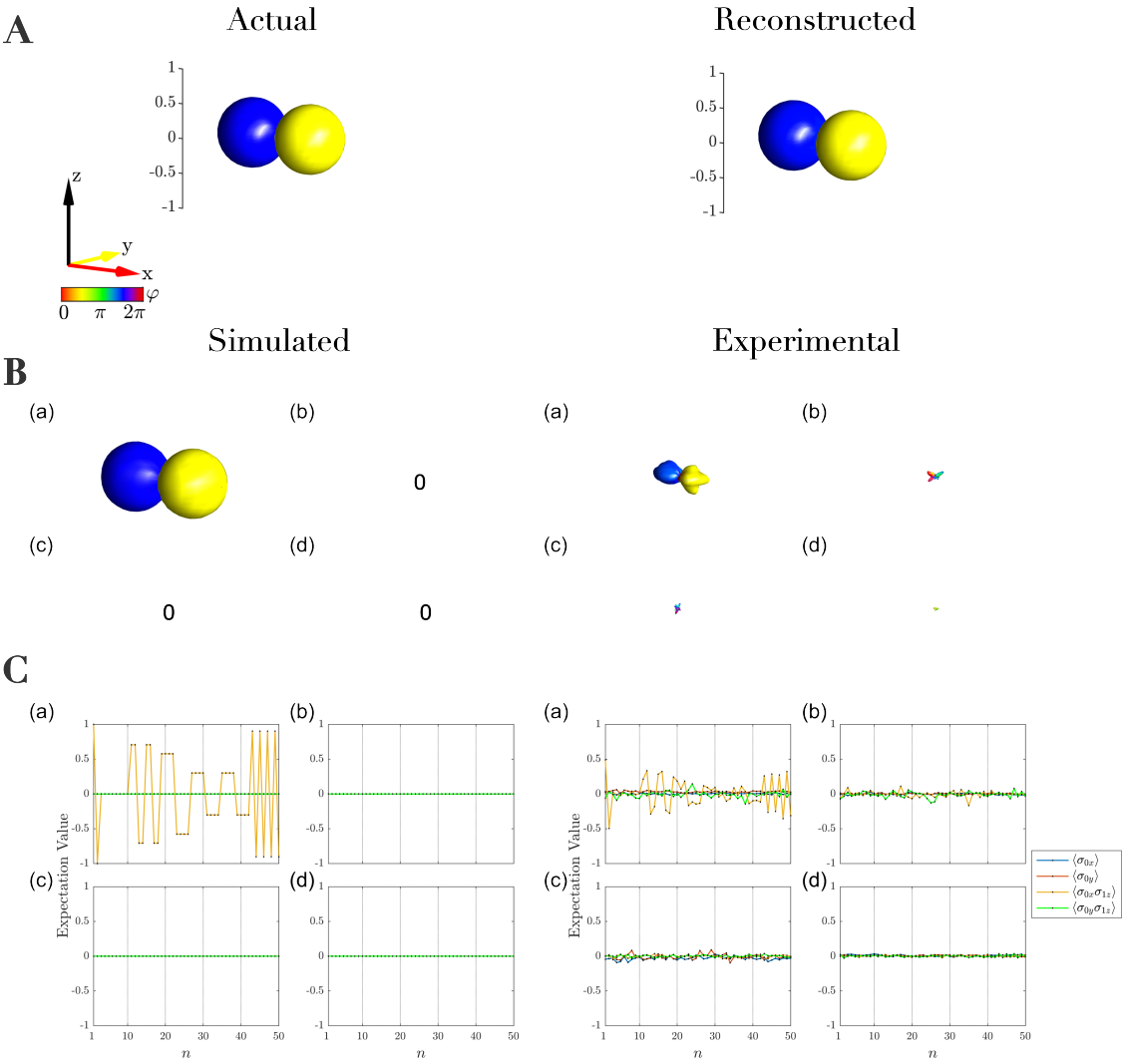


**Figure 4.23:** The figure presents the simulated and the experimental results for the Wigner tomography of the $U = \mathrm{X}$ (NOT) gate. Quaternions corresponding to a NOT gate are $A = 1$ and $B = C = D = 0$. The actual droplet and the reconstructed droplet from the experimental droplets are depicted in **A**. The simulated and experimental droplets corresponding to scaled process droplets (a) $\hat{f}_1$, (b) $\hat{f}_2$, (c) $\hat{f}_3$, and (d) $\hat{f}_4$ are shown in **B**. Panel **C** shows the corresponding expectation values, which were computed for the Lebedev 50 grid (depicted as black dots). The reconstructed droplet consists of optimized quaternions $A_{16}^{\mathrm{opt}} = 0.9991$, $B_{16}^{\mathrm{opt}} = 0.0090$, $C_{16}^{\mathrm{opt}} = -0.0407$, and $D_{16}^{\mathrm{opt}} = -0.0110$, obtained after employing the reconstruction algorithm with optimization. See Fig. C.1 for additional details on optimization results.

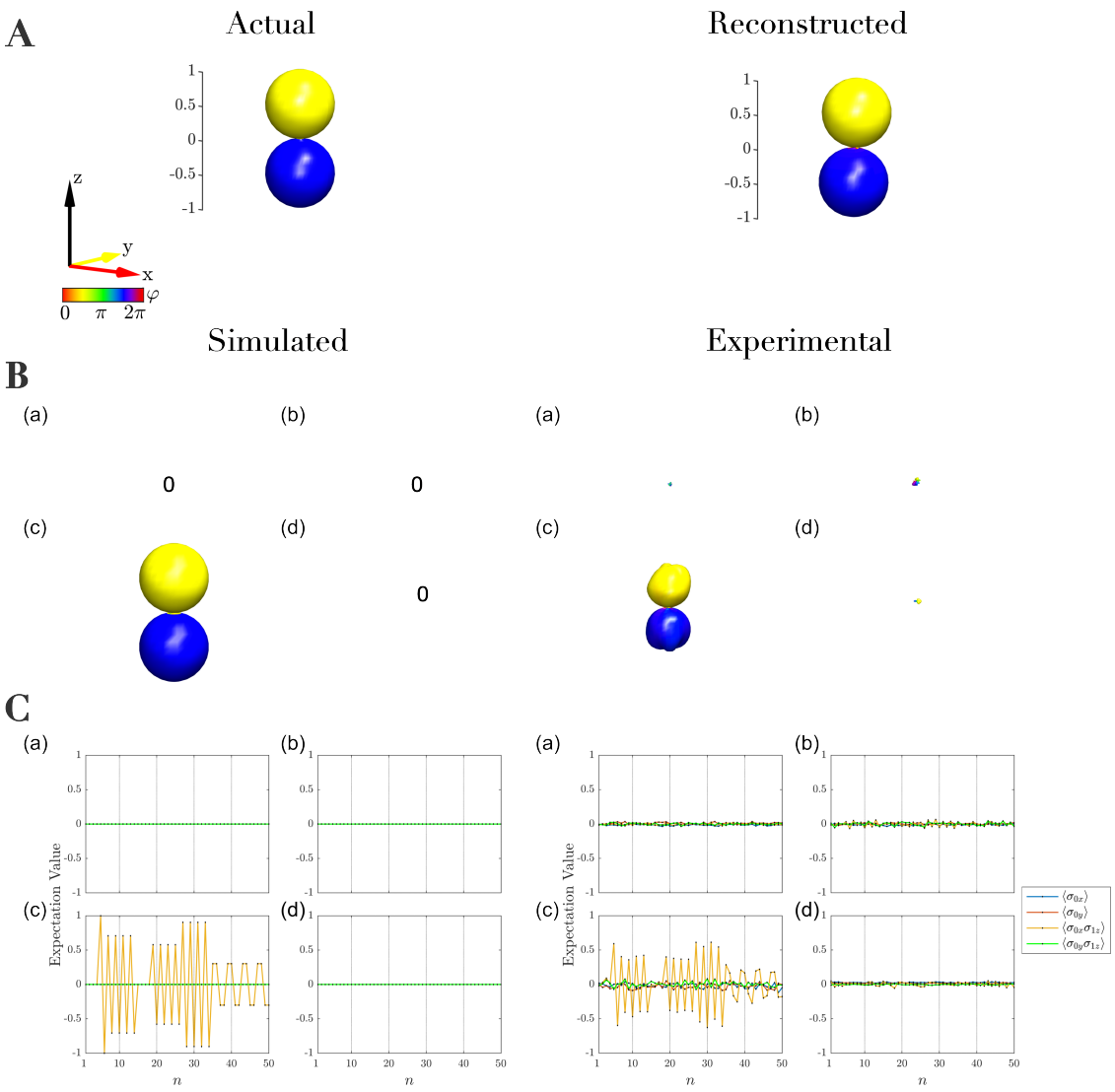


**Figure 4.24:** Figure presents the simulated and the experimental results for the Wigner tomography of the $U = \mathrm{Z}$ gate. Quaternions corresponding to a Z gate are $C = 1$ and $A = B = D = 0$. Similar to Fig. 4.23, actual and reconstructed droplets are presented in **A**. The simulated and experimental scaled process droplets (a) $\hat{f}_1$, (b) $\hat{f}_2$, (c) $\hat{f}_3$, and (d) $\hat{f}_4$ are shown in **B**, and the corresponding expectation values are shown in **C**. The values of quaternions after employing the reconstruction algorithm with optimization are: $A_{15}^{\mathrm{opt}} = -0.0023$, $B_{15}^{\mathrm{opt}} = 0.0794$, $C_{15}^{\mathrm{opt}} = 0.9966$, and $D_{15}^{\mathrm{opt}} = 0.0210$. See Fig. C.2 for additional details on optimization results.

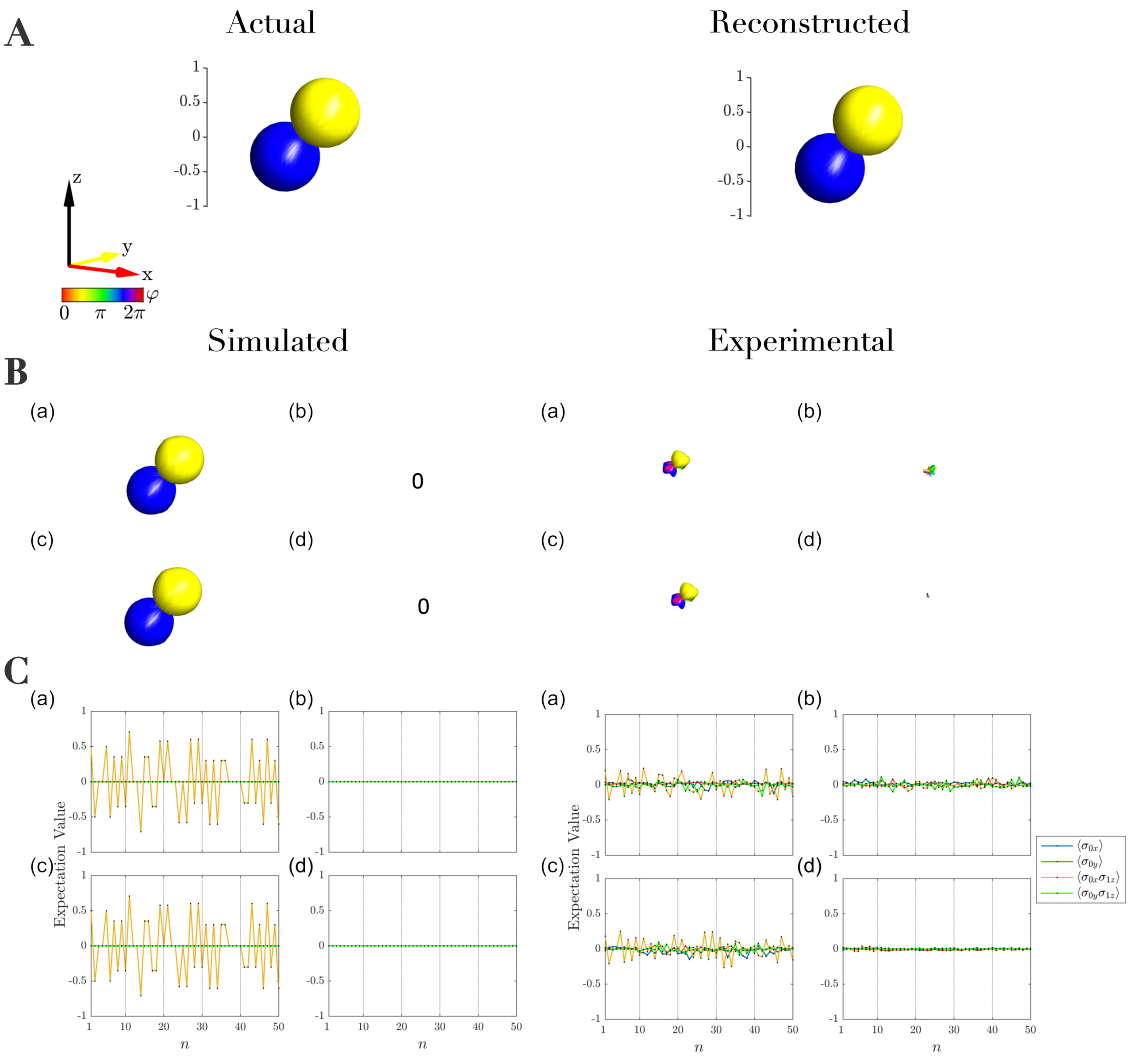


**Figure 4.25:** Figure shows the simulated and the experimental results for the Wigner tomography of the $U = \mathrm{H}$ (Hadamard) gate. Quaternions corresponding to a Hadamard gate are $A = C = -0.7071$ and $B = D = 0$. Similar to Fig. 4.23, actual and reconstructed droplets are presented in **A**. The simulated and experimental scaled process droplets (a) $\hat{f}_1$, (b) $\hat{f}_2$, (c) $\hat{f}_3$, and (d) $\hat{f}_4$ are shown in **B**, and the corresponding expectation values are shown in **C**. The values of quaternions after employing the reconstruction algorithm with optimization are: $A_{11}^{\mathrm{opt}} = 0.6566$, $B_{11}^{\mathrm{opt}} = 0.0172$, $C_{11}^{\mathrm{opt}} = 0.7540$, and $D_{11}^{\mathrm{opt}} = 0.089$ See Fig. C.3 for additional details on optimization results.

Chapter

# 5 Adaptive Approach for Wigner Process Tomography

The approach discussed in Chapter 3 for the tomography of *known* processes requires an implementation of a controlled-U operation $cU^{[N+1]}$, to map a given $N$ qubit unitary process matrix, $U^{[N]}$ onto a $N+1$ qubit Hermitian density matrix, $\rho^{[N+1]}$. Experimentally, implementing a controlled version of a unitary process matrix $U$ differs from implementing the unitary process $U$ itself. Therefore, the information obtained through process tomography pertains to the controlled version of $U$ rather than process matrix $U$.

The process tomography approach discussed in Chapter 4 acknowledges this limitation and provides a generalized approach for tomography of *unknown* processes. An essential step for this approach is the circuit illustrated in Fig. 4.5, which is designed to map $N$ qubit scaled unknown process matrices, $U_k^{[N]} = \epsilon_k U^{[N]}$ onto $N+1$ qubit Hermitian density matrices $\rho_{U_k}^{[N+1]}$ (see Eq. 4.17). This is achieved by iteratively applying the circuit $k$ times for different rotations $\mathcal{G}_k^{[N]}$. An explicit form of the scaling factors $\epsilon_k$ is given in Eq. 4.18. In general, if the unitary process $U^{[N]}$ is completely unknown, i.e., no prior partial information is available, the circuit may be repeated up to $4^N$ times, with $\mathcal{G}_k^{[N]}$ encompassing all elements of the Pauli operator basis, as discussed in Sec. 4.2. However, if partial information about the process $U$ is given, it can be used to design an appropriate rotation $\mathcal{G}$, thereby reducing the number of circuit repetitions, $k$.

For example, for a single-qubit ($N=1$) system, presented in Sec. 4.6.1, the number of circuit repetitions is $k=4$, with rotations $\mathcal{G}_1^{[1]} = \sigma_x$, $\mathcal{G}_2^{[1]} = \sigma_y$, $\mathcal{G}_3^{[1]} = \sigma_z$, and $\mathcal{G}_4^{[1]} = \mathbb{1}$, which can be reduced to a few repetitions in this adapted approach if a reasonable guess of the process is available. For example, if a desired target gate $U_{\text{tar}}$ is to be implemented, a reasonable guess for the actually realized gate $U_a$ by a circuit will be the $U_{\text{tar}}$. We illustrate the adaptive approach in Fig. 5.1 using noise-less examples and an iterative version of the adaptive approach in Fig. 5.2 using noisy data.

In figure Fig. 5.1, the first column shows the guess process droplet $f_{\text{gue}}$ corresponding to the guessed process, $U_{\text{gue}} = \text{X(NOT)}$ gate in all the three examples. The second column displays the actual process droplet $f_a$ corresponding to the actual process $U_a$

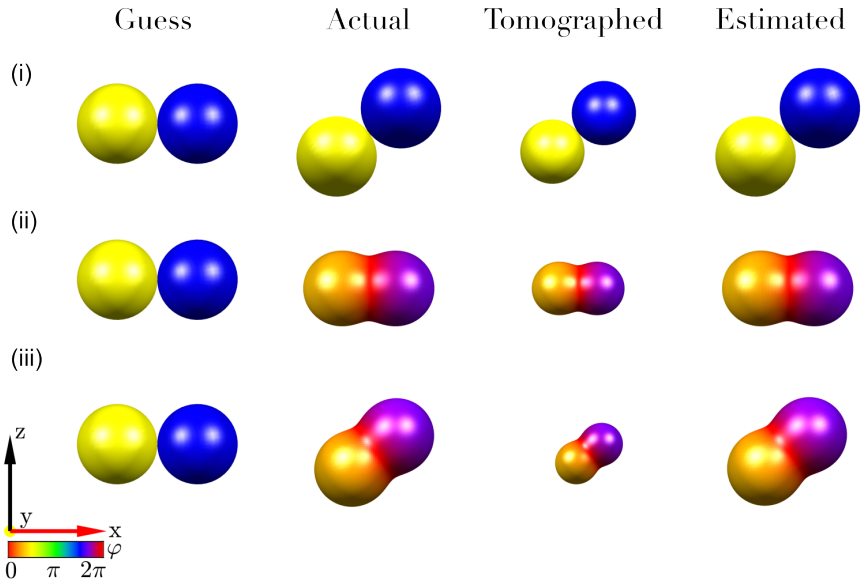


**Figure 5.1:** Examples of the reconstruction of unknown actual processes using the adapted approach. The first column shows the droplets corresponding to the presumed (guess) process $U_{\text{gue}} = \text{NOT}$. The second column illustrates the droplet corresponding to the actual experimental process $U_a$, showcasing variations in rotation axis and angle (see main text) compared to the $U_{\text{gue}}$. The third column presents the tomographed droplet, and the fourth column displays the reconstructed actual droplet estimated from the tomographed droplet.

realized experimentally. The third column exhibits the tomographed scaled process droplet $\hat{f}$ corresponding to the scaled process matrix $\hat{U} = \epsilon U_a$, with

$$\epsilon = \frac{1}{2}\,\text{tr}((U_a)^\dagger U_{\text{gue}}). \tag{5.1}$$

In this adaptive approach, the circuits are performed only once with $\mathcal{G} = U_{\text{gue}}$. Finally, the last column shows the estimated droplet ($f_{\text{est}}$) after reconstruction, which involves estimating the process matrix of tomographed droplet $\hat{f}$ and normalizing it (the approach discussed in supplementary Sec. C.2 can be directly employed by replacing $\hat{f}_{\text{comb}}$ by $\hat{f}$).

Now, we discuss different examples presented in Fig. 5.1. As stated earlier, the guess process $U_{\text{gue}}$ in all three examples is a NOT gate, with rotation angle $\gamma = \pi$ and rotation axis $\vec{n} = (1, 0, 0)$ (refer to Eq. 4.7). However, in the first example, showcased in the top row of Fig. 5.1, the actual process ($U_a$) has a different rotation axis $\vec{n} = (0.8, 0, 0.6)$, but the same rotation angle, i.e., $\gamma = \pi$. This discrepancy in the rotation axis is evident from the orientation of the actual droplet $f_a$ shown in the second column compared to the guess droplet $f_{\text{gue}}$ shown in the first column. The tomographed scaled process droplet $\hat{f} = \epsilon f_a$, with $\epsilon = 0.8$ (computed using Eq. 5.1) is shown in the third column. Finally, the fourth column shows the estimated droplet $f_{\text{est}}$, which reconstructs the actual unknown process droplet $f_a$ precisely (compare the actual process droplet

and reconstructed process droplet shown in the second and fourth columns, respectively).

Similarly, in the second example, showcased in the middle row of Fig. 5.1, the actual process ($U_a$) has a different rotation angle $\gamma = 0.5\pi$, but the same rotation axis, i.e., $\vec{n} = (1, 0, 0)$. The discrepancy in the rotation angle $\gamma$ is evident by the shape of the actual droplet $f_a$ shown in the second column compared to the guess droplet $f_{\text{gue}}$ shown in the first column. In this case, the tomographed droplet shown in the third column is scaled by $\epsilon = 0.7071$ compared to the actual droplet $f_a$ in the second column. The fourth column shows the estimated droplet $f_{\text{est}}$, which reconstructs the actual unknown process droplet $f_a$ precisely (compare droplets of the second and fourth columns).

In the third example, showcased in the last row of Fig. 5.1, the actual process ($U_a$) has a difference in both the rotation axis ($\vec{n} = (0.8, 0, 0.6)$) as well as the rotation angle ($\gamma = 0.5\pi$). This discrepancy is evident by the orientation and the shape of the actual droplet $f_a$ shown in the second column compared to the guess droplet $f_{\text{gue}}$ shown in the first column. Here, the tomographed droplet shown in the third column is scaled by a factor of $\epsilon = 0.5657$ compared to the actual droplet $f_a$ in the second column. The fourth column shows the estimated droplet $f_{\text{est}}$, which reconstructs the actual unknown process droplet $f_a$ precisely (compare droplets of the second and fourth columns).

The examples in Fig. 5.1 showcase the efficacy of the adapted approach to estimate the unknown process $U_a$ from the tomographed droplet, utilizing only a single repetition of the tomography circuits with $\mathcal{G} = U_{\text{gue}}$. In this noise-less example, only one iteration is sufficient to obtain the actual process droplet $U_a$ from the tomographed droplet $\hat{f}$ due to its high signal-to-noise ratio. However, in the presence of noise, this might not be possible. In the next section, we introduce an iterative approach to estimate the actual process droplet from noisy tomographed droplet.

## 5.1 Iterative version of the adaptive approach

Here, we present an example in Fig. 5.2 to demonstrate an iterative version of the adaptive method for Wigner process tomography. Similar to the examples depicted in Fig. 5.1, the initial guess process $U_{\text{gue}}$ is a NOT gate, with a rotation angle $\gamma = \pi$ and a rotation axis $\vec{n} = (1, 0, 0)$. However, the actual process $U_a$ deviates from the guess process $U_{\text{gue}}$, having a rotation angle $\gamma = 0.5\pi$ and a rotation axis $\vec{n} = (0.8, 0, 0.6)$. Here, we employ two iterations (marked as **1** and **2** in the figure) to reconstruct the actual process with a high signal-to-noise ratio from the tomographed droplets.

In the first iteration (top panel), the tomographed droplet $\hat{f}^{[1]}$ corresponding to the scaled process $\hat{U}_1 = \epsilon_1 U_a$, obtained by choosing the gate $\mathcal{G} = U_{\text{gue}}$, resulting in a scaling factor of $\epsilon_1 = 0.5657$. This results in a tomographed droplet with a low signal-to-noise ratio and estimates the process droplet $\hat{f}^{[1]}_{\text{est}}$ with a fidelity of 0.9864. Here, we employ

a second iteration (shown in the bottom panel), where the tomographed droplet $\hat{f}^{[2]}$ corresponding to the scaled process $\hat{U}_2 = \epsilon_2 U_a$ is obtained by choosing the estimated process droplet $\hat{f}^{[1]}_{\text{est}}$ from iteration **1** as the $\mathcal{G}$ gate. This results in a tomographed droplet with an improved signal-to-noise ratio from which the process droplet $\hat{f}^{[2]}_{\text{est}}$ is estimated with a fidelity of 0.9981.

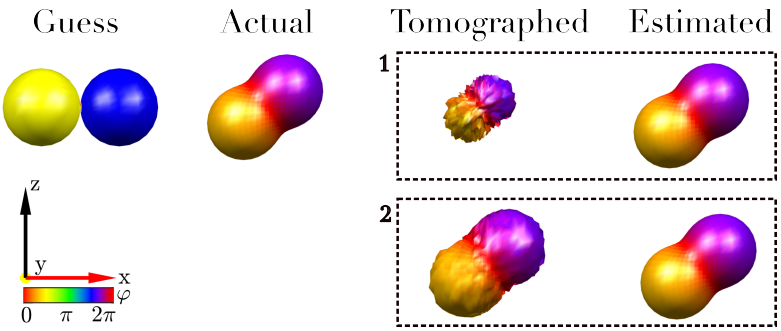


**Figure 5.2:** Demonstration of the reconstruction of the actual unknown process from noisy tomographed droplets using the iterative adapted approach. The first column displays the droplet corresponding to the guessed process, $U = \text{NOT}$ gate. The second column illustrates the droplet corresponding to the actual experimental process $U_a$. The third column presents the tomographed droplets for iterations **1** and **2**, along with the estimated droplets from the tomographed data.

The adapted approach, in general, is experimentally less resource intensive in comparison to the general approach presented in Fig. 4.8, particularly in terms of circuit repetitions $k$. Despite this efficiency, it still provides sufficient information about the actual unknown process, as demonstrated by single-qubit examples in Fig. 5.1 and Fig. 5.2. The adaptive approach can also be extended to multi-qubit unknown gates, where prior partial information, i.e., guess process, can be leveraged to design the $\mathcal{G}$ gate to efficiently estimate the actual process $U_a$ while requiring fewer repetitions $k$.

Chapter 6

# Discussion and Outlook

The aim of this thesis has been two-fold: first, to develop a general approach for Wigner tomography of quantum states and *known* quantum processes for pure-state quantum devices, and second, to extend this tomography approach to *unknown* quantum processes.

Chapter 1 established the groundwork of this thesis by discussing some fundamental concepts of quantum computing and the visualization approach for quantum operators. Chapter 2 and Chapter 3 of this thesis adopts the methodology described in Ref. [14, 16] to enable Wigner tomography on pure-state quantum devices. We demonstrated the experimental implementation of these tomography approaches on IBM quantum devices. The experimentally measured droplet shapes provide a unique, vivid visual representation of abstract quantum operators, which reflects their essential features. For example, for a single-qubit, the droplet orientation provides the same information as the Bloch vector representation. However, the DROPS representation is not limited to single-qubit systems but can also be used to visualize states and processes in multi-qubit systems, where different droplets provide information about the expectation values of multi-qubit operators, such as $\sigma_{1x}\sigma_{2x}$ or $\sigma_{1x}\sigma_{2z}\sigma_{2y}$, etc.

Chapter 4 extended the Wigner tomography to unknown unitary quantum processes by addressing the limitation of mapping an unknown process matrix onto a density matrix. The study provides a novel approach to map scaled versions of the unknown unitary process matrix onto density matrices, which enables the tomography of corresponding scaled process droplets. We showed how these scaled process droplets can be combined to reconstruct the unknown process for a single-qubit system. We also demonstrated the reconstruction approach using the experimental results obtained from the IBM quantum devices. We also discuss an adaptive approach for performing Wigner process tomography in Chapter 5, resulting in a resource-efficient approach compared to the general approach presented in Chapter 4.

In this thesis, the following points have been explicitly addressed and discussed:

1. We discussed the visualization of quantum operators using the DROPS representation with examples in Sec. 1.2.

2. The description of DROPS tomography was rewritten in the language of quantum

information processing instead of the language of NMR. A simple example is the consistent use of Pauli operators $\sigma_x$, $\sigma_y$, and $\sigma_z$ instead of corresponding spin operators $I_x$, $I_y$, and $I_z$, which are not only unfamiliar outside the NMR community but also differs by a factor of two. Another example is the description of quantum operations in terms of elementary quantum gates using the quantum assembly language (QASM) nomenclature instead of their descriptions in terms of rotations and pulse sequences.

3. Whereas it is natural to measure expectation values directly on ensemble quantum processors, in pure-state quantum processors, expectation values are typically estimated by averaging the outcomes of projective measurements for many repetitions of the experiment. The measurement of expectation values of single-qubit and multiqubit operators necessary for DROPS tomography is explicitly discussed. See relevant Sec. 2.4 and Sec. A.3.

4. The fact that DROPS tomography of unitary processes requires an ancilla qubit to be prepared in the *maximally mixed state* could create the false impression that it cannot be applied to pure-state quantum processors. We removed this hurdle by explaining (see Sec. B.2) and demonstrating (see Sec. 3.4.1 and Sec. 4.6.1) how the concept of temporal averaging can be used to circumvent this problem.

5. We also showed how to implement discretized scalar products between droplet functions defined on a finite number of sampling points (see Sec. A.2) and how to use them to extract the standard matrix representation (see Sec. 2.3 and Sec. 3.3) and the fidelity of states and processes based on experimentally measured droplets.

6. We presented the results of a numerical study on the effect of different sampling schemes on the fidelity with which states can be experimentally tomographed in Sec. 2.5.

7. For a convenient adaptation of the Wigner tomography of state and known quantum processes, we provide a Python package `DROPStomo` [27] for a direct implementation using Qiskit. These packages can also be adapted to other frameworks in a straightforward way.

8. We developed an approach to perform Wigner tomography for unknown unitary quantum processes by overcoming the existing limitation of mapping an unknown process onto a density matrix.

9. We discussed the existing naive circuit in Sec. 4.1 and identified its limitations (blindspots) in providing a complete mapping of an unknown process matrix onto a density matrix using a simple state vector and density matrix formalism.

10. We developed an extended version of the circuit in Sec. 4.2, which removed the blindspots and enabled the mapping of scaled versions of the unknown process

matrix onto density matrices. This allowed us to experimentally tomograph the scaled versions of the unknown processes.

11. We developed a reconstruction algorithm, an approach to rebuilding an unknown unitary quantum process from the experimentally tomographed scaled process droplets. We demonstrated the potential of the reconstruction algorithm to rebuild the process matrix from noisy droplets using several numerical examples in Sec. 4.4.1.

12. We demonstrated how the reconstruction algorithm can be combined with an optimization routine and discussed the benefits gained from this integrated approach (see Sec. 4.4.3 and Sec. 4.5).

13. During the experimental implementation of the Wigner process tomography approach on IBM devices, we detected the phase shift in qubit $q_0$. We quantified and corrected it using the calibration approach discussed in Sec. 4.6.1.

14. We experimentally demonstrated the Wigner tomography approach for unknown processes on IBM devices and showcased the results using the reconstruction algorithm in Sec. 4.6.1.

15. We discussed a resource-efficient adaptive approach for Wigner process tomography and showcased it using examples in Chapter 5.

The state and the *known* process tomography approaches presented in Chapter 2 and Chapter 3, respectively, have limitations similar to conventional tomography methods with respect to the number of qubits due to the exponential growth of the Hilbert space dimension. However, for a small number of qubits, Wigner-type DROPS tomography forms an easily implementable alternative approach with additional benefits and without any extra cost in terms of experimental time and signal-to-noise ratio. In particular, the DROPS visualization allows one to see the type of errors present in a given realization of quantum states and processes directly.

The Wigner tomography approach for *unknown* processes presented in Chapter 4 fills a gap in the general theory work of Wigner tomography but is resource-intensive in comparison to the conventional tomography approaches [3] both in terms of a number of qubits and the number of experiments. In general, for the Wigner tomography of an $N$ qubit unknown process, $2N + 1$ qubits are required. The total number of experiments required for different system qubits $N$ is dependent on the number of expectation values to be estimated along with the circuit repetitions for different controlled-$\mathcal{G}$ operations. Although the total number of experiments in terms of the number of controlled-$\mathcal{G}$ operations can be significantly cut down by employing an adaptive approach discussed in Chapter 5. In the near term, for devices with a limited number of qubits, where the scalable error correction is not viable, the long experimental implementation time of

the CSWAP gates used in this approach also results in a loss of signal-to-noise ratio of the tomographed droplets.

The unknown process tomography approach can be used as a tool for "quality check" of the unknown gates. For example, consider a scenario where a particular quantum computer can execute all the gates necessary for the tomography approach with very high fidelity. Suppose we are given a target random gate to evaluate its performance on this particular device. We can plug this target gate directly into our tomography circuits and perform the full unknown process tomography to extract information about the performance of the random gate. Alternatively, we can also do this using the adaptive approach, assuming that the controlled version of the target gate can also be executed with high fidelity. In this case, only a few experiments can provide information about the random target gate. This kind of "quality check" would not have been possible with the existing tomography approach of known processes, which provides information about the controlled version of the process rather than the process itself.

In the near future, the Wigner state tomography approach and the Python package associated with it can be directly used to tomograph the multi-qubit states to visually demonstrate the classical and non-classical correlations that are being developed in our research group. The Python packages will also be developed further for an extended number of qubits. We have observed that the effect of relaxation channels, such as amplitude damping and phase damping, can be directly visualized using the droplet representing a quantum state of a system. We are, therefore, brainstorming ideas of how to experimentally tomograph these effects using the Wigner tomography approach.

The tomography approaches presented here are entirely general and can be tested on different types of qubits, such as neutral atoms and superconducting, which are developed within the framework of Munich Quantum Valley to compare and benchmark the performance of different quantum computers.

Appendix

# A Appendix of Chapter 2

## A.1 Generating basis droplets

Here, we present the transformation from Pauli operators to complex spherical harmonics to generate the basis droplets for one and two qubits. The general basis transformation from Pauli to tensor operators is taken from Ref. [1]. The basis droplets can be generated for a chosen set of angles $\alpha$ and $\beta$.

### A.1.1 One qubit

Basis droplet functions ($f_{\sigma_k}$) for $k \in \{0, 1, 2, 3\}$ in terms of complex spherical harmonics ($Y_{jm}$) for one qubit are:

$$\begin{aligned} f_{\sigma_0}(\beta, \alpha) &= \sqrt{2} Y_{00}(\beta, \alpha) \\ f_{\sigma_x}(\beta, \alpha) &= Y_{1-1}(\beta, \alpha) - Y_{11}(\beta, \alpha) \\ f_{\sigma_y}(\beta, \alpha) &= i(Y_{1-1}(\beta, \alpha) + Y_{11}(\beta, \alpha)) \\ f_{\sigma_z}(\beta, \alpha) &= \sqrt{2} Y_{10}(\beta, \alpha). \end{aligned} \tag{A.1}$$

Where $\sigma_0$ corresponds to identity.

### A.1.2 Two qubit

Basis droplet functions ($f_{\sigma_k}$) for $k \in \{0, 1, \ldots, 15\}$ in terms of complex spherical harmonics ($Y_{jm}$) for two qubit are:

$$
\begin{aligned}
f_{\sigma_0}(\beta,\alpha) &= Y_{00}(\beta,\alpha)\\
f_{\sigma_{1x}}(\beta,\alpha) &= \frac{1}{\sqrt{2}}(Y_{1-1}(\beta,\alpha) - Y_{11}(\beta,\alpha))\\
f_{\sigma_{1y}}(\beta,\alpha) &= \frac{i}{\sqrt{2}}(Y_{1-1}(\beta,\alpha) + Y_{11}(\beta,\alpha))\\
f_{\sigma_{1z}}(\beta,\alpha) &= Y_{10}(\beta,\alpha)\\
f_{\sigma_{2x}}(\beta,\alpha) &= \frac{1}{\sqrt{2}}(Y_{1-1}(\beta,\alpha) - Y_{11}(\beta,\alpha))\\
f_{\sigma_{2y}}(\beta,\alpha) &= \frac{i}{\sqrt{2}}(Y_{1-1}(\beta,\alpha) + Y_{11}(\beta,\alpha))\\
f_{\sigma_{2z}}(\beta,\alpha) &= Y_{10}(\beta,\alpha)\\
f_{\sigma_{1x2x}}(\beta,\alpha) &= \frac{1}{\sqrt{3}}Y_{00}(\beta,\alpha) + \frac{1}{2}Y_{2-2}(\beta,\alpha) - \frac{1}{\sqrt{6}}Y_{20}(\beta,\alpha) + \frac{1}{2}Y_{22}(\beta,\alpha)\\
f_{\sigma_{1x2y}}(\beta,\alpha) &= \frac{1}{\sqrt{2}}Y_{10}(\beta,\alpha) + \frac{i}{2}Y_{2-2}(\beta,\alpha) - \frac{i}{2}Y_{22}(\beta,\alpha)\\
f_{\sigma_{1x2z}}(\beta,\alpha) &= -\frac{i}{2}Y_{1-1}(\beta,\alpha) - \frac{i}{2}Y_{11}(\beta,\alpha) + \frac{1}{2}Y_{2-1}(\beta,\alpha) - \frac{1}{2}Y_{21}(\beta,\alpha)\\
f_{\sigma_{1y2x}}(\beta,\alpha) &= -\frac{1}{\sqrt{2}}Y_{10}(\beta,\alpha) + \frac{1}{2}Y_{2-2}(\beta,\alpha) - \frac{i}{2}Y_{22}(\beta,\alpha)\\
f_{\sigma_{1y2y}}(\beta,\alpha) &= \frac{1}{\sqrt{3}}Y_{00}(\beta,\alpha) - \frac{1}{2}Y_{2-2}(\beta,\alpha) - \frac{1}{\sqrt{6}}Y_{20}(\beta,\alpha) - \frac{1}{2}Y_{22}(\beta,\alpha)\\
f_{\sigma_{1y2z}}(\beta,\alpha) &= \frac{1}{2}Y_{1-1}(\beta,\alpha) - \frac{1}{2}Y_{11}(\beta,\alpha) + \frac{i}{2}Y_{2-1}(\beta,\alpha) + \frac{i}{2}Y_{21}(\beta,\alpha)\\
f_{\sigma_{1z2x}}(\beta,\alpha) &= \frac{i}{2}Y_{1-1}(\beta,\alpha) + \frac{i}{2}Y_{11}(\beta,\alpha) + \frac{1}{2}Y_{2-1}(\beta,\alpha) - \frac{1}{2}Y_{21}(\beta,\alpha)\\
f_{\sigma_{1z2y}}(\beta,\alpha) &= -\frac{1}{2}Y_{1-1}(\beta,\alpha) + \frac{1}{2}Y_{11}(\beta,\alpha) + \frac{i}{2}Y_{2-1}(\beta,\alpha) + \frac{i}{2}Y_{21}(\beta,\alpha)\\
f_{\sigma_{1z2z}}(\beta,\alpha) &= \frac{1}{\sqrt{3}}Y_{00}(\beta,\alpha) + \sqrt{\frac{2}{3}}Y_{20}(\beta,\alpha).
\end{aligned}
\tag{A.2}
$$

Where $\sigma_0$ corresponds to identity.

## A.2 Scalar product for tensor operators and spherical functions

The scalar product between two tensor operators $T_A$ and $T_B$ is defined as

$$\langle T_A | T_B \rangle = \mathrm{tr}(T_A^\dagger T_B), \tag{A.3}$$

where $T_A^\dagger$ is the adjoint (conjugate transpose) of operator $T_A$. The tensor operators $T_A$ and $T_B$ can be mapped to spherical droplet functions $f_A(\theta,\phi)$ and $f_B(\theta,\phi)$ using Eq. 1.15. The scalar product of Eq. A.3 is by construction identical to the scalar product of the droplet functions defined as [14]

$$\langle f_A(\theta,\phi)|f_B(\theta,\phi)\rangle = \int_{\theta=0}^{\pi}\int_{\phi=0}^{2\pi} f_A^*(\theta,\phi)f_B(\theta,\phi)\sin(\theta)d\theta d\phi. \tag{A.4}$$

This definition corresponds to the following simple procedure: for each point on the surface of a sphere, the complex conjugate value of the spherical function $f_A$ is multiplied by the value of the spherical function $f_B$ and the integration of the resulting product $f_A^* f_B$ over the surface of the sphere is the value of the desired scalar product $\langle f_A|f_B\rangle$.

If the spherical functions are only known at a finite number of sample points ($\theta_i$,$\phi_i$) the scalar product can be approximated by a corresponding discretized scalar product of the form

$$\langle f_A|f_B\rangle' = \sum_i \mathrm{w}_i f_A^*(\theta_i,\phi_i)f_B(\theta_i,\phi_i) \approx \langle f_A(\theta,\phi)|f_B(\theta,\phi)\rangle. \tag{A.5}$$

## A.3 Calculation of expectation values

A single qubit general state is given by,

$$|\psi\rangle = c_0|0\rangle + c_1|1\rangle \tag{A.6}$$

the probability of the state in $|0\rangle$ is $p_0 = |c_0|^2$ and for state in $|1\rangle$ is $p_1 = |c_1|^2$, and where $p_0 + p_1 = 1$. A quantum circuit is repeated several times (depending on the number of shots $N_s$) to generate a probability statistics for the state ($|c_0|$ or $|c_1|$) of quantum system. The density matrix corresponding to state $|0\rangle$ and $|1\rangle$ is,

$$\sigma_0 = |0\rangle\langle 0| = \begin{pmatrix} 1 & 0 \\ 0 & 0 \end{pmatrix}, \sigma_1 = |1\rangle\langle 1| = \begin{pmatrix} 0 & 0 \\ 0 & 1 \end{pmatrix} \tag{A.7}$$

and the operator $\sigma_z$ is given by,

$$\sigma_z = \begin{pmatrix} 1 & 0 \\ 0 & -1 \end{pmatrix} \tag{A.8}$$

which can also be written as,

$$\sigma_z = \sigma_0 - \sigma_1 \tag{A.9}$$

and hence the expectation value of $\sigma_z$ is given by

$$\begin{aligned} \langle\sigma_z\rangle &= \langle\sigma_0\rangle - \langle\sigma_1\rangle \\ \langle\sigma_z\rangle &= p_0 - p_1. \end{aligned} \tag{A.10}$$

Similarly the expectation value of $\mathbb{1}$ is,

$$\langle \mathbb{1} \rangle = p_0 + p_1 = 1. \tag{A.11}$$

For a two-qubit system, the general quantum state is

$$|\psi\rangle = c_{00}|00\rangle + c_{01}|01\rangle + c_{10}|10\rangle + c_{11}|11\rangle, \tag{A.12}$$

the expectation value of operator $\sigma_{1z}\sigma_{2z}$ is

$$\begin{aligned} \langle \sigma_{1z}\sigma_{2z} \rangle &= \langle \sigma_{00} \rangle - \langle \sigma_{01} \rangle - \langle \sigma_{10} \rangle + \langle \sigma_{11} \rangle \\ \langle \sigma_{1z}\sigma_{2z} \rangle &= p_{00} - p_{01} - p_{10} + p_{11}. \end{aligned} \tag{A.13}$$

where $\sigma_{ab}$, and $p_{ab}$ for $a, b \in \{0, 1\}$ are the density matrices and probabilities corresponding to state $|ab\rangle$. The other expectation values such as $\langle \sigma_{1x} \rangle$, $\langle \sigma_{1x}\sigma_{2x} \rangle$, etc. can be calculated by using the local unitary operations ($u^{(\ell,n)}$) as the detection-associated rotation step.

## A.4 Plot of the mean fidelity as a function of the total number of shots

Here, the plot of the mean fidelities $\bar{\mathcal{F}}_s$ for four different sampling schemes and the standard state tomography method as a function of the total number of shots $N_{tot}$ is presented. Fig. A.1 shows the same data as in Fig. 2.9 and in addition, provides the standard deviations. Fig. A.2 shows results for the same numerical study for an equal superposition state $|\psi\rangle = \frac{1}{\sqrt{2}}(|0\rangle + |1\rangle)$.

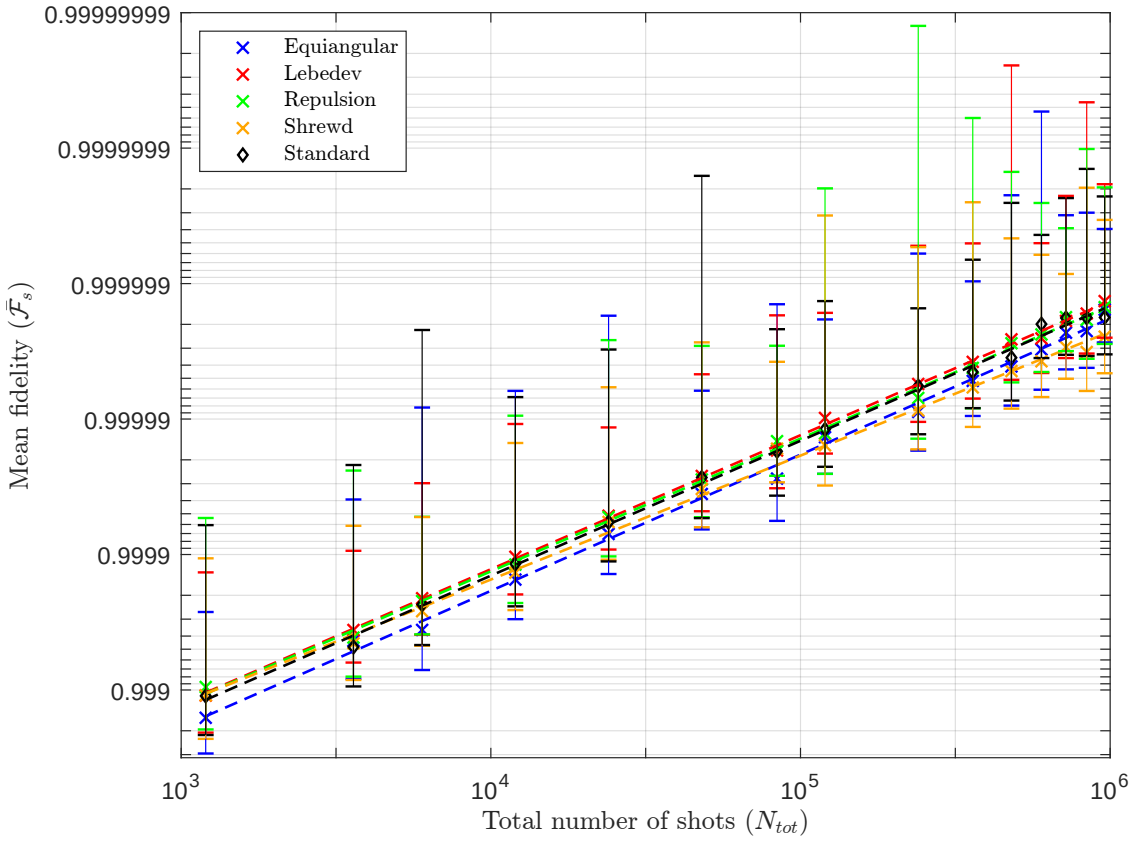


**Figure A.1:** Plot of the mean fidelity ($\bar{\mathcal{F}}_s$) as a function of the total number of shots ($N_{tot}$) for different sampling techniques and for the standard state tomography method applied to the quantum state $|\psi\rangle = (-0.69 - 0.098i)|0\rangle + (0.66 + 0.30i)|1\rangle$. The mean fidelity is calculated by repeating the simulation 100 times for each data point. In the simulation, only the noise due to a limited number of shots is considered. The standard deviations are shown by the vertical bars for each point.

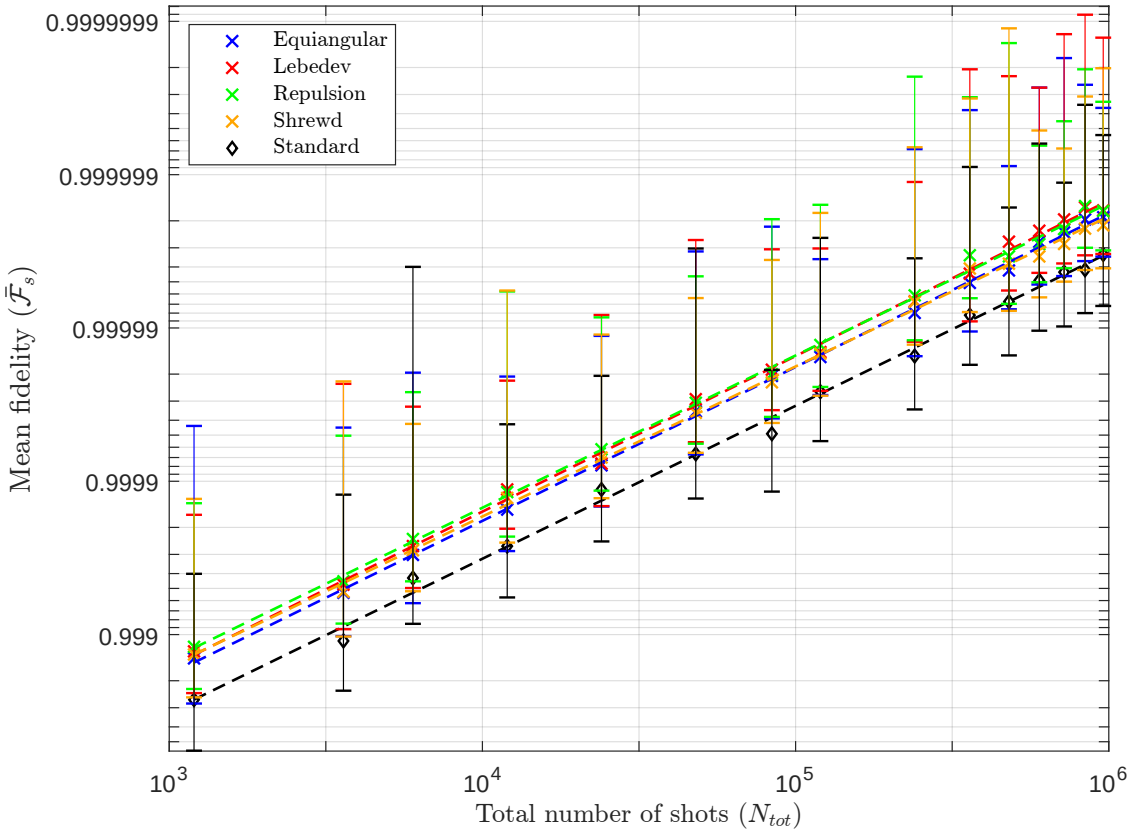


**Figure A.2:** Plot of the mean fidelity ($\bar{\mathcal{F}}_s$) as a function of the total number of shots for different sampling techniques and for the standard state tomography method applied to the quantum state $|\psi\rangle = \frac{1}{\sqrt{2}}(|0\rangle + |1\rangle)$. The mean fidelity is calculated by repeating the simulation 100 times for each data point. In the simulation, only the noise due to a limited number of shots is considered. The standard deviations are shown by the vertical bars for each point.

*Appendix*

# B Appendix of Chapter 3

## B.1 Proof of equivalence of Eq. 3.5 and Eq. 3.6

After the mapping of the process matrix onto the density matrix, the Eq. 3.4 can be written as:

$$\rho_U^{[N+1]} = \frac{1}{2^{N+1}}(\sigma^- \otimes U^{[N]} + \sigma^+ \otimes (U^{[N]})^\dagger + \mathbb{1} \otimes \mathbb{1}^{[N]}), \tag{B.1}$$

where $\sigma^+ = \frac{1}{2}(\sigma_x + i\sigma_y)$, and $\sigma^- = \frac{1}{2}(\sigma_x - i\sigma_y)$. The equivalence of Eq. 3.6 and Eq. 3.5 can be shown by the following steps which transform Eq. 3.6 to Eq. 3.5:

$$\begin{aligned}
s_j\langle\sigma^+ \otimes T_{j,\alpha\beta}^{(\ell)[N]}\rangle_{\rho_U^{[N+1]}} &= s_j \mathrm{tr}[(\sigma^+ \otimes T_{j,\alpha\beta}^{(\ell)[N]})\rho_U^{[N+1]}] \\
&= s_j \mathrm{tr}\left[\begin{pmatrix} 0^{[N]} & T_{j,\alpha\beta}^{(\ell)[N]} \\ 0^{[N]} & 0^{[N]} \end{pmatrix}\begin{pmatrix} \mathbb{1}^{[N]} & (U^{[N]})^\dagger \\ U^{[N]} & \mathbb{1}^{[N]} \end{pmatrix}\right] \\
&= s_j \mathrm{tr}\left[\begin{pmatrix} T_{j,\alpha\beta}^{(\ell)[N]}U^{[N]} & T_{j,\alpha\beta}^{(\ell)[N]} \\ 0^{[N]} & 0^{[N]} \end{pmatrix}\right] \\
&= s_j \mathrm{tr}[T_{j,\alpha\beta}^{(\ell)[N]}U^{[N]}] \\
&= s_j \mathrm{tr}[(T_{j,\alpha\beta}^{(\ell)[N]})^\dagger U^{[N]}] \\
&= s_j\langle T_{j,\alpha\beta}^{(\ell)[N]}|U^{[N]}\rangle.
\end{aligned} \tag{B.2}$$

Note that axial tensor operators are Hermitian, i.e., $(T_{j,\alpha\beta}^{(\ell)[N]})^\dagger = (T_{j,\alpha\beta}^{(\ell)[N]})$ [14].

## B.2 Temporal averaging to create maximally mixed states

For Wigner quantum process tomography, the preparation of the system qubit in a *maximally* mixed state is required (see preparation ($\mathcal{P}$) step in Sec. 3.2). As stated in Sec 3.4.1, in our experimental implementation, a temporal averaging approach [56, 57] was used to prepare the maximally mixed state. A detailed explanation of this approach and alternative methods are provided in the following.

### B.2.1 Creating maximally mixed state from pure states

In general, there is an infinite number of different ways to prepare the "maximally mixed state" $\rho_{mm}$ of a single-qubit ($N = 1$) based on an ensemble of pure single-qubit

states [57]. For example, the maximally mixed state can be realized using an ensemble of two extremal pure states $|\uparrow_{\hat{n}}\rangle$ and $|\downarrow_{\hat{n}}\rangle$ corresponding to two antipodal points on the Bloch sphere:

$$\rho_{mm}^{[1]} = \frac{1}{2}\mathbb{1}^{[1]} = \frac{1}{2}\begin{pmatrix}1 & 0\\ 0 & 1\end{pmatrix} = \frac{1}{2}|\uparrow_{\hat{n}}\rangle\langle\uparrow_{\hat{n}}| + \frac{1}{2}|\downarrow_{\hat{n}}\rangle\langle\downarrow_{\hat{n}}|. \tag{B.3}$$

Hence, for the single-qubit case, the preparation of a maximally mixed state $\rho_{mm}^{[1]}$ can be realized by simply repeating the experiment twice and averaging the measurement results (which we refer to as *temporal* averaging here): once by starting with the pure-state $|0\rangle$ (corresponding to the density operator $|0\rangle\langle 0| = \left(\begin{smallmatrix}1 & 0\\ 0 & 0\end{smallmatrix}\right)$) and once by starting with the pure-state $|1\rangle$ (corresponding to the density operator $|1\rangle\langle 1| = \left(\begin{smallmatrix}0 & 0\\ 0 & 1\end{smallmatrix}\right)$). Note that the average density operator of the two experiments is identical to the desired maximally mixed state $\rho_{mm}^{[1]}$.

A relatively straightforward alternative approach to preparing the system qubit in the maximally mixed state would be to prepare it in the state $|0\rangle$ and to repeat each experiment multiple times, where, in each repetition, it is randomly decided (with 50% probability) whether to flip the qubit using a NOT gate. However, the standard deviation of the average population of state $|1\rangle$ from the expected value of 0.5 decreases only with the inverse of the square root of the number of repetitions in this probabilistic approach. Hence, a large number of repetitions would be required to minimize this additional noise source due to the imperfect realization of the completely mixed state. For example, to achieve a standard deviation of less than 0.005, about 8000 repetitions would be necessary, even in the case of perfect gate operation.

Another alternative way to create a maximally mixed state is by creating a maximal entanglement between the system and an ancilla qubit and partially tracing out of the ancilla qubit. However, this approach requires additional resources (both in a number of qubits and gates) compared to the scheme presented here.

### B.2.2 Creating the maximally mixed state of a two-qubit system by temporal averaging

For the case of a two-qubit ($N = 2$) system, the maximally mixed state $\rho_{mm}^{[2]}$ is of the form

$$\rho_{mm}^{[2]} = \frac{1}{4}\mathbb{1}^{[2]} = \frac{1}{4}\begin{pmatrix}1 & 0 & 0 & 0\\ 0 & 1 & 0 & 0\\ 0 & 0 & 1 & 0\\ 0 & 0 & 0 & 1\end{pmatrix} = \frac{1}{4}|00\rangle\langle 00| + \frac{1}{4}|01\rangle\langle 01| + \frac{1}{4}|10\rangle\langle 10| + \frac{1}{4}|11\rangle\langle 11|. \tag{B.4}$$

In this case, the preparation of $\rho_{mm}^{[2]}$ can be realized by simply repeating the experiment four times (for all the computational basis states) and averaging the measurement

results.

### B.2.3 Creating the state $|+\rangle\langle+| \otimes \frac{1}{2^N}\mathbb{1}^{[N]}$ required for process tomography of unitary gates

This section gives a detailed calculation of the preparation step $\mathcal{P}$ (see Sec. 3.2) for one and two-qubit Wigner process tomography. For single-qubit process tomography, two qubits $q_0$ and $q_1$ are required and the preparation step requires preparing qubit $q_0$ in an equal superposition state $|+\rangle = \frac{1}{\sqrt{2}}(|0\rangle + |1\rangle)$ and $q_1$ in a maximally mixed state $\frac{1}{2}\mathbb{1}^{[1]}$. The corresponding density matrix is given by

$$\rho_0^{[2]} = |+\rangle\langle+| \otimes \frac{1}{2}\mathbb{1}^{[1]} = \frac{1}{2}\begin{pmatrix}1 & 1\\ 1 & 1\end{pmatrix} \otimes \frac{1}{2}\begin{pmatrix}1 & 0\\ 0 & 1\end{pmatrix} = \frac{1}{4}\begin{pmatrix}1 & 0 & 1 & 0\\ 0 & 1 & 0 & 1\\ 1 & 0 & 1 & 0\\ 0 & 1 & 0 & 1\end{pmatrix}, \tag{B.5}$$

This maximally mixed state of qubit $q_1$ is achieved using temporal averaging (see Eq. B.3), i.e., by averaging measurement result of two experiments initialized in states $|\psi_1\rangle = |+\rangle \otimes |0\rangle = |+0\rangle$ and $|\psi_2\rangle = |+\rangle \otimes |1\rangle = |+1\rangle$. The two corresponding density matrices are

$$\rho_1^{[2]} = |\psi_1\rangle\langle\psi_1| = |+0\rangle\langle+0| = \frac{1}{2}\begin{pmatrix}1 & 0 & 1 & 0\\ 0 & 0 & 0 & 0\\ 1 & 0 & 1 & 0\\ 0 & 0 & 0 & 0\end{pmatrix}, \tag{B.6}$$

and

$$\rho_2^{[2]} = |\psi_2\rangle\langle\psi_2| = |+1\rangle\langle+1| = \frac{1}{2}\begin{pmatrix}0 & 0 & 0 & 0\\ 0 & 1 & 0 & 1\\ 0 & 0 & 0 & 0\\ 0 & 1 & 0 & 1\end{pmatrix}. \tag{B.7}$$

Therefore, the density matrix $\rho_0^{[2]}$ can be prepared by averaging the density operators $\rho_1^{[2]}$ and $\rho_2^{[2]}$:

$$\rho_0^{[2]} = \frac{1}{2}\rho_1^{[2]} + \frac{1}{2}\rho_2^{[2]}. \tag{B.8}$$

Similarly, for a two-qubit process tomography, three qubits $q_0$, $q_1$, and $q_2$ are required. The preparation step requires preparing qubit $q_0$ in an equal superposition state $|+\rangle$ and qubits $q_1$ and $q_2$ in a maximally mixed state $\frac{1}{4}\mathbb{1}^{[2]}$. This resultant density matrix $\rho_0^{[3]}$ can be achieved using Eq. B.4 as follows:

$$\rho_0^{[3]} = |+\rangle\langle+| \otimes \frac{1}{4}\mathbb{1}^{[2]} = \frac{1}{8}|+00\rangle\langle+00| + \frac{1}{8}|+01\rangle\langle+01| + \frac{1}{8}|+10\rangle\langle+10| + \frac{1}{8}|+11\rangle\langle+11|. \tag{B.9}$$

This corresponds to performing four different experiments and averaging the output density operators.

### B.2.4 Expectation values for mixed states

Here, we explicitly show that the expectation values for a mixed state can be expressed as an average of the expectation values of pure states. The expectation value of an observable $A$ is given by

$$\langle A \rangle_\rho = \mathrm{tr}(A\rho). \tag{B.10}$$

The density matrix $\rho$ can be written in its spectral decomposition as

$$\rho = \sum_{k=1}^{2^N} p_k |\beta_k\rangle\langle\beta_k|, \tag{B.11}$$

where $p_k$ are non-negative coefficients which add up to one and $|\beta_k\rangle$ are the basis states. Eq. B.10 can be rewritten as:

$$\begin{aligned} \langle A \rangle_\rho &= \mathrm{tr}\left( A \sum_{k=1}^{2^N} p_k |\beta_k\rangle\langle\beta_k| \right) \\ &= \sum_{k=1}^{2^N} p_k \langle A \rangle_{|\beta_k\rangle\langle\beta_k|}. \end{aligned} \tag{B.12}$$

Hence, for the special case where $\rho$ is the completely mixed state with identical coefficients $p_k = \frac{1}{2^N}$, the expectation value $\langle A \rangle_\rho$ is simply the average of the expectation values for the pure states $|\beta_k\rangle$. For example, for a single qubit, the maximally mixed state $\mathbb{1}^{[1]}/2$ can be written as: where $|\beta_1\rangle = |0\rangle$, $|\beta_2\rangle = |1\rangle$, and $p_1 = p_2 = \frac{1}{2}$. This implies that experimentally estimating the expectation value of an observable $A$ for the mixed state $\frac{\mathbb{1}^{[1]}}{2}$ can be realized by averaging the expectation values from two different experiments, one in which the qubit is in the pure state $|0\rangle$, and another in which the qubit is in the pure state $|1\rangle$.

*Appendix*

# C Appendix of Chapter 4

## C.1 Generalization of Eq. 4.10

The density matrix $\rho_0 = |\psi_0\rangle\langle\psi_0|$ corresponding to the state $|\psi_0\rangle$ in Table 4.3 is:

$$\rho_0^{[2N+1]} = \frac{(|0\rangle + |1\rangle)(\langle 0| + \langle 1|)}{2} \otimes \rho_s^{[N]} \otimes \rho_a^{[N]} = \frac{1}{2}\begin{pmatrix} \rho_s^{[N]} \otimes \rho_a^{[N]} & \rho_s^{[N]} \otimes \rho_a^{[N]} \\ \rho_s^{[N]} \otimes \rho_a^{[N]} & \rho_s^{[N]} \otimes \rho_a^{[N]} \end{pmatrix}, \quad \text{(C.1)}$$

where $\rho_s = |\psi_s\rangle\langle\psi_s|$ and $\rho_a = |\psi_a\rangle\langle\psi_a|$) represents the initial density matrix of the system $q_1, \ldots, q_N$ and the ancilla $q_1^a, \ldots, q_N^a$ qubits, respectively. The density matrix $\rho_1 = |\psi_1\rangle\langle\psi_1|$, i.e., after the first controlled-swap block of the circuit presented in Fig. 4.5 is:

$$\begin{aligned} \rho_1^{[2N+1]} &= \begin{pmatrix} \mathbb{1}^{[2N]} & 0^{[2N]} \\ 0^{[2N]} & \text{swap}^{[2N]} \end{pmatrix} \rho_0^{[2N+1]} \begin{pmatrix} \mathbb{1}^{[2N]} & 0^{[2N]} \\ 0^{[2N]} & \text{swap}^{[2N]} \end{pmatrix}^\dagger \\ &= \frac{1}{2}\begin{pmatrix} \rho_s^{[N]} \otimes \rho_a^{[N]} & (\rho_s^{[N]} \otimes \rho_a^{[N]})\text{swap}^{[2N]} \\ \text{swap}^{[2N]}(\rho_s^{[N]} \otimes \rho_a^{[N]}) & \rho_a^{[N]} \otimes \rho_s^{[N]} \end{pmatrix}. \end{aligned} \quad \text{(C.2)}$$

The matrix form of the controlled-swap gate is provided in Eq. 1.14. After operation $\mathbb{1}^{[N+1]} \otimes U^{[N]}$ (second block of circuit in Fig. 4.5) one obtains

$$\begin{aligned} \rho_2^{[2N+1]} &= \begin{pmatrix} \mathbb{1}^{[N]} \otimes U^{[N]} & 0^{[2N]} \\ 0^{[2N]} & \mathbb{1}^{[N]} \otimes U^{[N]} \end{pmatrix} \rho_1^{[2N+1]} \begin{pmatrix} \mathbb{1}^{[N]} \otimes U^{[N]} & 0^{[2N]} \\ 0^{[2N]} & \mathbb{1}^{[N]} \otimes U^{[N]} \end{pmatrix}^\dagger \\ &= \frac{1}{2}\begin{pmatrix} \rho_s^{[N]} \otimes U^{[N]}\rho_a^{[N]}(U^{[N]})^\dagger & (\rho_s^{[N]} \otimes U^{[N]}\rho_a^{[N]})\text{swap}^{[2N]}(\mathbb{1}^{[N]} \otimes (U^{[N]})^\dagger) \\ (\mathbb{1}^{[N]} \otimes U^{[N]})\text{swap}^{[2N]}(\rho_s^{[N]} \otimes \rho_a^{[N]})(U^{[N]})^\dagger) & \rho_a^{[N]} \otimes U^{[N]}\rho_s^{[N]}(U^{[N]})^\dagger \end{pmatrix}. \end{aligned} \quad \text{(C.3)}$$

The density matrix after applying the second controlled-swap block (third block of circuit in Fig. 4.5) is

$$\rho_3^{[2N+1]} = \frac{1}{2}\begin{pmatrix} \rho_s^{[N]} \otimes U^{[N]}\rho_a^{[N]}(U^{[N]})^\dagger & \rho_s^{[N]}(U^{[N]})^\dagger \otimes U^{[N]}\rho_a^{[N]} \\ U^{[N]}\rho_s^{[N]} \otimes \rho_a^{[N]}(U^{[N]})^\dagger & U^{[N]}\rho_s^{[N]}(U^{[N]})^\dagger \otimes \rho_a^{[N]} \end{pmatrix}. \quad \text{(C.4)}$$

After controlled rotation ($c\mathcal{G}_k$) (the last block of circuit in Fig 4.5), the resulting density matrix is

$$\begin{aligned}\rho_4^{[2N+1]} &= \begin{pmatrix} \mathbb{1}^{[2N]} & 0^{[2N]} \\ 0^{[2N]} & \mathbb{1}^{[N]} \otimes \mathcal{G}_k^{[N]} \end{pmatrix} \rho_3^{[2N+1]} \begin{pmatrix} \mathbb{1}^{[2N]} & 0^{[2N]} \\ 0^{[2N]} & \mathbb{1}^{[N]} \otimes \mathcal{G}_k^{[N]} \end{pmatrix}^\dagger \\ &= \frac{1}{2} \begin{pmatrix} \rho_s^{[N]} \otimes U^{[N]} \rho_a^{[N]} (U^{[N]})^\dagger & \rho_s^{[N]} (U^{[N]})^\dagger \otimes U^{[N]} \rho_a^{[N]} (\mathcal{G}_k^{[N]})^\dagger \\ U^{[N]} \rho_s^{[N]} \otimes \mathcal{G}_k^{[N]} \rho_a^{[N]} (U^{[N]})^\dagger & U^{[N]} \rho_s^{[N]} (U^{[N]})^\dagger \otimes \mathcal{G}_k^{[N]} \rho_a^{[N]} (\mathcal{G}_k^{[N]})^\dagger \end{pmatrix}.\end{aligned} \tag{C.5}$$

After tracing out $N$ ancilla qubits $q_1^a, \ldots, q_N^a$ (indicated by the red block in the circuit depicted in Fig. 4.5), the density matrix is

$$\rho_5^{[N+1]} = \frac{1}{2} \begin{pmatrix} \rho_s^{[N]} & \rho_s^{[N]} (U^{[N]})^\dagger \operatorname{tr}(U^{[N]} \rho_a^{[N]} (\mathcal{G}_k^{[N]})^\dagger) \\ U^{[N]} \rho_s^{[N]} \operatorname{tr}(\mathcal{G}_k^{[N]} \rho_a^{[N]} (U^{[N]})^\dagger) & U^{[N]} \rho_s^{[N]} (U^{[N]})^\dagger \end{pmatrix}. \tag{C.6}$$

Here $\operatorname{tr}(\mathcal{G}_k^{[N]} \rho_a^{[N]} (U^{[N]})^\dagger)$ is the scaling factor mentioned before. This factor depnds on unknown process $U^{[N]}$ and rotations $\mathcal{G}_k$ with different values of $k$.

In case when initially, the system $q_1, \ldots, q_N$ and the ancilla qubits $q_1^a, \ldots, q_N^a$ are both in a fully mixed state, i.e., $\rho_s = \rho_a = \frac{1}{2^N} \mathbb{1}^{[N]}$, Eq. C.6 modifies as:

$$\tilde{\rho}_5^{[N+1]} = \frac{1}{2^{(N+1)}} \begin{pmatrix} \mathbb{1}^{[N]} & \epsilon_k^* (U^{[N]})^\dagger \\ \epsilon_k U^{[N]} & \mathbb{1}^{[N]} \end{pmatrix}, \tag{C.7}$$

which can be rewritten as:

$$\rho_{U_k}^{[N+1]} = \frac{1}{2^{N+1}} \begin{pmatrix} \mathbb{1}^{[N]} & (U_k^{[N]})^\dagger \\ U_k^{[N]} & \mathbb{1}^{[N]} \end{pmatrix}, \tag{C.8}$$

with scaling factor

$$\epsilon_k = \frac{1}{2^N} \langle U^{[N]} | \mathcal{G}_k^{[N]} \rangle. \tag{C.9}$$

Here $\epsilon_k^*$ is the complex conjugate of $\epsilon_k$. Eq. C.7 shows the mapping of an $N$ qubit unknown process matrix $U^{[N]}$ onto an $N+1$ qubit density matrix up to a scaling factor $\epsilon_k$.

## C.2 Estimation of unitary process matrix from $\hat{f}_{\text{comb}}$

For estimating a single qubit ($N = 1$) unitary process matrix from the combined process droplet $\hat{f}_{\text{comb}}$ (defined in the step 4 of Algo. 4.1), we use a methodology described in Sec. 3.4.1. As defined in Eq. 3.15, any single-qubit unitary process can be expressed in terms of Pauli operators [3] as

$$U^{[1]} = \sum_{k=0}^{3} c_k \sigma_k \tag{C.10}$$

with in general complex coefficients $c_k$ for $k \in \{0, 1, 2, 3\}$. Where $\sigma_0$ is a 2×2 identity ($\mathbb{1}$) matrix, while $\sigma_1$, $\sigma_2$ and $\sigma_3$ are the standard Pauli matrices $\sigma_x$, $\sigma_y$ and $\sigma_z$, respectively. Using Eq. 2.16, the coefficients $c_k$ are obtained by calculating the scalar product between the basis droplets $f_{\sigma_k}$ (refer to Sec. A.1.1) and the combined droplet $\hat{f}_{\text{comb}}$:

$$\begin{aligned} c_0 &= \langle f_{\sigma_0} | \hat{f}_{\text{comb}} \rangle \\ c_1 &= \langle f_{\sigma_x} | \hat{f}_{\text{comb}} \rangle \\ c_2 &= \langle f_{\sigma_y} | \hat{f}_{\text{comb}} \rangle \\ c_3 &= \langle f_{\sigma_z} | \hat{f}_{\text{comb}} \rangle. \end{aligned} \tag{C.11}$$

In an ideal noise-less scenario, the coefficient $c_0$ is purely real and the coefficients $c_1$, $c_2$, and $c_3$ contains only non-zero imaginary components [3]. But in the case with noise (limited number of grid points, etc.), this generally does not hold, which leads to a non-symmetric matrix. Here, we present two methods to construct unitary matrices from the coefficients $c_k$ and show their equivalence using a numerical example.

**Method 1**

In the first method, to construct a matrix $U_1$, we only consider the imaginary part of the coefficients $c_1$, $c_2$, and $c_3$ and only real part of the coefficient $c_0$. Using this consideration, a process matrix can be formed as follows:

$$U_1 = \text{Re}(c_0)\mathbb{1} + i(\text{Im}(c_1)\sigma_x + \text{Im}(c_2)\sigma_y + \text{Im}(c_3)\sigma_z), \tag{C.12}$$

which results into a symmetric matrix:

$$U_1 = \begin{pmatrix} \text{Re}(c_0) + i\,\text{Im}(c_3) & \text{Im}(c_2) + i\,\text{Im}(c_1) \\ -\text{Im}(c_2) + i\,\text{Im}(c_1) & \text{Re}(c_0) - i\,\text{Im}(c_3) \end{pmatrix}. \tag{C.13}$$

This matrix is not necessarily unitary. The estimated quaternions from $U_1$ (see Eq. 4.15) are:

$$\begin{aligned} A_1 &= \text{Im}(U_1(1,2)) = \text{Im}(U_1(2,1)) = \text{Im}(c_1) \\ B_1 &= \text{Re}(U_1(1,2)) = -\text{Re}(U_1(2,1)) = \text{Im}(c_2) \\ C_1 &= \text{Im}(U_1(1,1)) = -\text{Im}(U_1(1,1)) = \text{Im}(c_3) \\ D_1 &= \text{Re}(U_1(1,1)) = \text{Re}(U_1(1,1)) = \text{Re}(c_0). \end{aligned} \tag{C.14}$$

These quaternions are normalized such that, $N_1 = A_1^2 + B_1^2 + C_1^2 + D_1^2 = 1$, leading to new normalized quaternions: $\tilde{A}_1 = \frac{A_1}{\sqrt{N_1}}$, $\tilde{B}_1 = \frac{B_1}{\sqrt{N_1}}$, $\tilde{C}_1 = \frac{C_1}{\sqrt{N_1}}$, and $\tilde{D}_1 = \frac{D_1}{\sqrt{N_1}}$. These new normalized quaternions result in a special unitary matrix:

$$\tilde{U}_1 = \begin{pmatrix} \tilde{D}_1 + i\tilde{C}_1 & \tilde{B}_1 + i\tilde{A}_1 \\ -\tilde{B}_1 + i\tilde{A}_1 & \tilde{D}_1 - i\tilde{C}_1. \end{pmatrix}. \tag{C.15}$$

### Method 2

In this method, to construct a matrix $U_2$, we take the full contribution of coefficients $c_k$, such that a process matrix can be formed using the general definition of Eq. C.10 as:

$$U_2 = c_0\mathbb{1} + c_1\sigma_x + c_2\sigma_y + c_3\sigma_z, \tag{C.16}$$

which results in a matrix that is not necessarily symmetric, i.e., does not follow the matrix structure of $U_1$ in Eq. C.13. Here, to use the complete information, the estimation of quaternions from the matrix $U_2$ must be computed by taking an average of different matrix elements:

$$\begin{aligned} A_2 &= \frac{1}{2}(\mathrm{Im}(U_2(1,2)) + \mathrm{Im}(U_2(2,1))) \\ B_2 &= \frac{1}{2}(\mathrm{Re}(U_2(1,2)) - \mathrm{Re}(U_2(2,1))) \\ C_2 &= \frac{1}{2}(\mathrm{Im}(U_2(1,1)) - \mathrm{Im}(U_2(2,2))) \\ D_2 &= \frac{1}{2}(\mathrm{Re}(U_2(1,1)) + \mathrm{Re}(U_2(2,2))). \end{aligned} \tag{C.17}$$

These quaternions are normalized such that, $N_2 = A_2^2 + B_2^2 + C_2^2 + D_2^2 = 1$, leading to new normalized quaternions: $\tilde{A}_2 = \frac{A_2}{\sqrt{N_2}}$, $\tilde{B}_2 = \frac{B_2}{\sqrt{N_2}}$, $\tilde{C}_2 = \frac{C_2}{\sqrt{N_2}}$, and $\tilde{D}_2 = \frac{D_2}{\sqrt{N_2}}$. These new normalized quaternions result in a special unitary matrix:

$$\tilde{U}_2 = \begin{pmatrix} \tilde{D}_2 + i\tilde{C}_2 & \tilde{B}_2 + i\tilde{A}_2 \\ -\tilde{B}_2 + i\tilde{A}_2 & \tilde{D}_2 - i\tilde{C}_2. \end{pmatrix}. \tag{C.18}$$

### Example

Here, we consider an example with shot noise for the estimation of the unitary matrix from the droplet $\hat{f}_{\mathrm{comb}}$. The coefficients $c_k$ computed using Eq. C.11 are:

$$\begin{aligned} c_0 &= 0.7470 - i0.0083 \\ c_1 &= -0.0056 + i0.1525 \\ c_2 &= 0.0026 + i0.3479 \\ c_3 &= -0.0010 - i0.5599. \end{aligned} \tag{C.19}$$

### Using Method 1

The matrix $U_1$ computed using Eq. C.12 in method 1 is:

$$U_1 = \begin{pmatrix} 0.7470 - i0.5599 & 0.3679 + i0.1525 \\ -0.3679 + i0.1525 & 0.7470 + i0.5599 \end{pmatrix}. \tag{C.20}$$

The estimated quaternions from the above matrix are: $A_1 = 0.1525$, $B_1 = 0.3679$, $C_1 = -0.5599$, and $D_1 = 0.7470$. The matrix after the normalization of quaternions is:

$$\tilde{U}_1 = \begin{pmatrix} 0.7412 - i0.5555 & 0.3452 + i0.1513 \\ -0.3452 + i0.1513 & 0.7412 + i0.5555 \end{pmatrix}. \tag{C.21}$$

**Using Method 2**

The matrix $U_2$ computed using Eq. C.16 in method 2 is:

$$U_2 = \begin{pmatrix} 0.7460 - i0.5682 & 0.3424 + i0.1499 \\ -0.3535 + i0.1551 & 0.7480 + i0.5516 \end{pmatrix}. \tag{C.22}$$

Note that the above matrix is not symmetric. The estimated quaternions using Eq. C.17 are: $A_2 = 0.1525$, $B_2 = 0.3679$, $C_2 = -0.5599$, and $D_2 = 0.7470$. The matrix after the normalization of quaternions is:

$$\tilde{U}_2 = \begin{pmatrix} 0.7412 - i0.5555 & 0.3452 + i0.1513 \\ -0.3452 + i0.1513 & 0.7412 + i0.5555 \end{pmatrix}. \tag{C.23}$$

Both approaches lead to the same unitary matrix, i.e., $\tilde{U}_1 = \tilde{U}_2$. In our study, we use method 1 to estimate a unitary matrix from the droplet $\hat{f}_{\text{comb}}$.

## C.3 Additional experimental figures

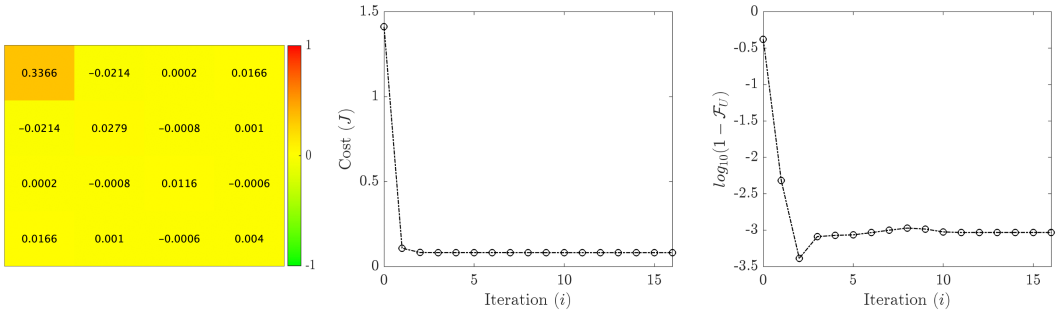


**Figure C.1:** Additional figures for the reconstruction using experimental tomography data of the X gate shown in Fig. 4.23. The figure shows the correlation matrix (left), plot of cost with iteration (middle), and plot of non-fidelity $(1 - \mathcal{F}_U)$ in the logarithmic scale with iteration (right).

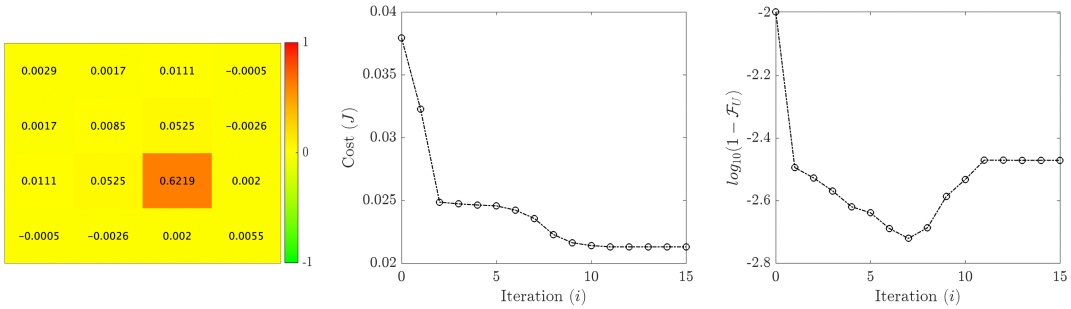


**Figure C.2:** Additional figures for the reconstruction using experimental tomography data of the Z gate shown in Fig. 4.24. The figure shows the correlation matrix (left), plot of cost with iteration (middle), and plot of non-fidelity $(1 - \mathcal{F}_U)$ in the logarithmic scale with iteration (right).

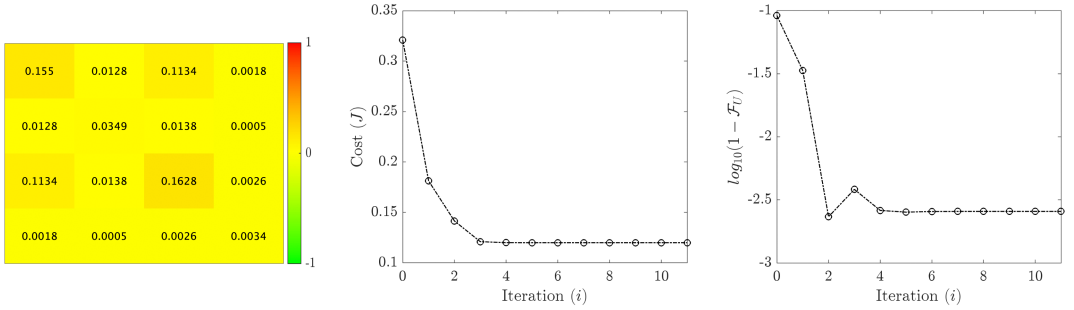


**Figure C.3:** Additional figures for the reconstruction using experimental tomography data of the Hadamard gate shown in Fig. 4.25. The figure shows the correlation matrix (left), plot of cost with iteration (middle), and plot of non-fidelity $(1 - \mathcal{F}_U)$ in the logarithmic scale with iteration (right).

*Appendix*

# D NMR experiments for Wigner tomography of unknown quantum processes

The experiments for Wigner tomography of the unknown process for a single system qubit were also performed on a Nuclear Magnetic Resonance (NMR) quantum information processor. This appendix includes the pulse design for the CSWAP block, which is experimentally crucial, along with some experimental details. These are a progression of experiments performed in our group for the demonstration of scanning-based tomography approach for quantum states [14] and known processes [16] on NMR.

## D.1 The NMR system

In an NMR quantum information processor, nuclear spins ($I$) within a molecule are treated as qubits [65, 66, 25]. Generally, a qubit is associated with a two-level spin-1/2 system. For example, in our demonstration experiments, we used a three-qubit sample, as shown in Fig. D.1. The three distinguishable spins ($^{19}$F, $^{13}$C, and $^{1}$H) can be addressed individually and are coupled by a spin-spin coupling ($J$).

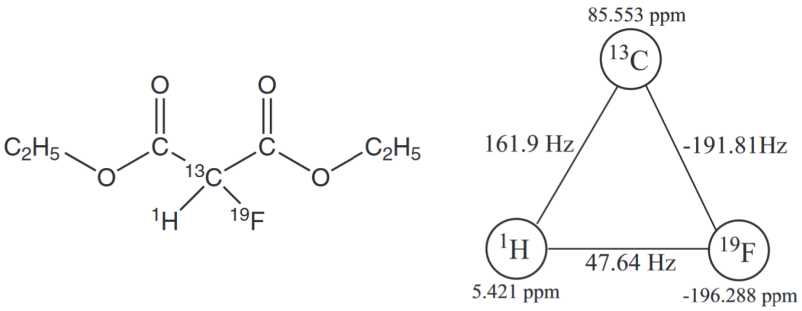


**Figure D.1:** On the right, a schematic of 2-$^{13}$C-2-fluoromalonic-acid-diethyl-ester molecule is shown, which is dissolved in $CD_3CN$ to be used as a three-qubit sample. On the left, a topology of three individual qubits is shown with their chemical shift (in parts per million) and coupling constant between them (in Hertz).

Before proceeding further, we define the product operator basis used in NMR. The four basis operators for a single spin-1/2 system are given by

$$I_x = \frac{1}{2}\begin{pmatrix} 0 & 1 \\ 1 & 0 \end{pmatrix}, \quad I_y = \frac{1}{2}\begin{pmatrix} 0 & -i \\ i & 0 \end{pmatrix}, \quad I_z = \frac{1}{2}\begin{pmatrix} 1 & 0 \\ 0 & -1 \end{pmatrix}, \quad I_0 = \frac{1}{2}\begin{pmatrix} 1 & 0 \\ 0 & 1 \end{pmatrix}. \tag{D.1}$$

These product operators form a complete basis for a single spin system. The basis can be extended to a $N$ spin system by computing the tensor products. For example, $I_{ka} = \mathbb{1} \otimes \cdots \otimes \mathbb{1} \otimes I_a \otimes \mathbb{1} \otimes \cdots \otimes \mathbb{1}$, where $I_{ka}$ corresponds to basis operator $I_a$ of $k^{th}$ spin and $a \in \{x, y, z, 0\}$.

In NMR, a system Hamiltonian ($H_{tot}$) can be written down as a summation of a natural Hamiltonian $H_0$ and a control Hamiltonian $H_c$ [67]. The natural Hamiltonian is given by

$$H_0 = \sum_k 2\pi\nu_{0k} I_{kz} + \sum_{j<k} 2\pi J_{jk} I_{jz} I_{kz}. \tag{D.2}$$

Where $2\pi\nu_0 = \omega_0 = -\gamma B_0$ is the Larmor frequency of a nucleus, $\gamma$ is a gyromagnetic ratio and $B_0$ is a static magnetic field. $J_{jk}$ is a spin-spin coupling constant between nucleus $j$ and $k$. The control or radiofrequency ($rf$) Hamiltonian is give by

$$H_c = \sum_k 2\pi\nu_{1k}[\cos(\alpha_k) I_{kx} + \sin(\alpha_k) I_{ky}]. \tag{D.3}$$

Where $2\pi\nu_1 = \omega_1$ and $\alpha$ are the frequency and phase of $B_1$ (radiofrequency) field, respectively. The $B_1$ field acts from the $xy$ plane with phase angle varying between 0 to $2\pi$. Unitary rotation can be achieved by varying the control Hamiltonian ($H_c$) with time $t$. A time evolution propagator under the effect of $H_c$ is given by

$$U_c = \exp\left( -i\left\{ \sum_k 2\pi\nu_{1k}[\cos(\alpha_k) I_{kx} + \sin(\alpha_k) I_{ky}] \right\} t \right). \tag{D.4}$$

Where $\omega_1 t = \theta$ is the rotation or flip angle, for example, a rotation around $x$ axis with $\pi$ angle can be simply written as $\exp(-i\pi I_x)$. These varying $rf$ fields are commonly known as *pulses* and can be designed in such a way to implement a particular process or gate experimentally.

As described in Sec. 4.6, for a single qubit system, performing an unknown process tomography in the context of finite-dimensional Wigner representation requires a total of three qubits. Each block of the quantum circuit (see Fig. 4.20) can be achieved by the application of suitable radio frequency pulses in NMR. One of the blocks of this quantum circuit is a Controlled-SWAP (CSWAP) gate, and implementing it on NMR with high precision is a crucial part of this experimental work. In the next section, we describe the design of this gate.

## D.2 Design of CSWAP gate

The CSWAP gate is a three-qubit quantum gate that swaps the information between two qubits if the control qubit is in a state $|1\rangle$. The matrix representation of the CSWAP gate is given by

$$U_{\text{cswap}} = \begin{pmatrix} 1 & 0 & 0 & 0 & 0 & 0 & 0 & 0 \\ 0 & 1 & 0 & 0 & 0 & 0 & 0 & 0 \\ 0 & 0 & 1 & 0 & 0 & 0 & 0 & 0 \\ 0 & 0 & 0 & 1 & 0 & 0 & 0 & 0 \\ 0 & 0 & 0 & 0 & 1 & 0 & 0 & 0 \\ 0 & 0 & 0 & 0 & 0 & 0 & 1 & 0 \\ 0 & 0 & 0 & 0 & 0 & 1 & 0 & 0 \\ 0 & 0 & 0 & 0 & 0 & 0 & 0 & 1 \end{pmatrix}.$$

A pulse sequence corresponding to this gate can be designed by using average Hamiltonian theory [62]. The time evolution propagator for the CSWAP gate be written as

$$U_{\text{cswap}} = \exp(-iH_{\text{eff}}t), \tag{D.5}$$

where $H_{\text{eff}}$ is the effective Hamiltonian [67] which effectively acts on nuclear spins when a pulse or $B_1$ field is applied. Considering $t = 1$, the equation can be rewritten as

$$\frac{H_{\text{eff}}}{2\pi} = \frac{-\log(U_{\text{cswap}})}{i2\pi}. \tag{D.6}$$

The resulting effective Hamiltonian in terms of product operators is

$$\frac{H_{\text{eff}}}{2\pi} = \frac{1}{8}(I_{1z} + 2I_{2x}I_{3x} + 2I_{2y}I_{3y} + 2I_{2z}I_{3z} - 4I_{1z}I_{2x}I_{3x} - 4I_{1z}I_{2y}I_{3y} - 4I_{1z}I_{2z}I_{3z}). \tag{D.7}$$

Using Eq.D.5 the operator $U_{\text{cswap}}$ can be written in terms of product operators as

$$\begin{aligned} U_{\text{cswap}} = \exp\left(-i\frac{\pi}{4}I_{1z}\right)\exp\left(-i\frac{\pi}{4}2I_{2x}I_{3x}\right)\exp\left(-i\frac{\pi}{4}2I_{2y}I_{3y}\right)\exp\left(-i\frac{\pi}{4}2I_{2z}I_{3z}\right) \\ \exp\left(i\frac{\pi}{4}4I_{1z}I_{2x}I_{3x}\right)\exp\left(i\frac{\pi}{4}4I_{1z}I_{2y}I_{3y}\right)\exp\left(i\frac{\pi}{4}4I_{1z}I_{2z}I_{3z}\right). \end{aligned} \tag{D.8}$$

Hence, a CSWAP gate can be realized experimentally by implementing a pulse sequence corresponding to each term in the above equation. Now, we discuss the transformation of these terms into pulse sequences.

Implementing a rotation of $\frac{\pi}{4}$ around $I_{1z}$ axis can be achieved directly by using a *hard* (full power and short duration) pulse. Bilinear terms can be realized by decomposing them into hard pulses and delays:

$$\begin{aligned} \exp\left(-i\frac{\pi}{4}2I_{2z}I_{3z}\right) = \exp\left(-i\frac{H_0}{16J_{23}}\right)\exp(-i\pi I_{1x})\exp\left(-i\frac{H_0}{16J_{23}}\right)\exp(i\pi(I_{2x}+I_{3x})) \\ \exp\left(-i\frac{H_0}{16J_{23}}\right)\exp(i\pi I_{1x})\exp\left(-i\frac{H_0}{16J_{23}}\right)\exp(-i\pi(I_{2x}+I_{3x})), \end{aligned} \tag{D.9}$$

where $J_{23}$ is the coupling constant between spin 2 and 3. The term $\exp\Big(-i\frac{H_0}{16J_{23}}\Big)$ is a delay term that corresponds to a free precession of spins under the influence of natural Hamiltonian $H_0$, without any rf pulse. The other bilinear terms can be implemented by transforming them as follows:

$$\exp\Big(-i\frac{\pi}{4}2I_{2x}I_{3x}\Big) = \exp\Big(-i\frac{\pi}{2}(I_{2y}+I_{3y})\Big)\exp\Big(-i\frac{\pi}{4}2I_{2z}I_{3z}\Big)\exp\Big(i\frac{\pi}{2}(I_{2y}+I_{3y})\Big), \tag{D.10}$$

and

$$\exp\Big(-i\frac{\pi}{4}2I_{2y}I_{3y}\Big) = \exp\Big(-i\frac{\pi}{2}(I_{2x}+I_{3x})\Big)\exp\Big(-i\frac{\pi}{4}2I_{2z}I_{3z}\Big)\exp\Big(i\frac{\pi}{2}(I_{2x}+I_{3x})\Big). \tag{D.11}$$

The trilinear terms can be realized by decomposing them into bilinear terms [68, 69] as follows:

$$\exp\Big(i\frac{\pi}{4}4I_{1z}I_{2z}I_{3z}\Big) = \exp\Big(-i\frac{\pi}{2}2I_{1z}I_{2x}\Big)\exp\Big(i\frac{\pi}{4}2I_{2y}I_{3z}\Big)\exp\Big(i\frac{\pi}{2}2I_{1z}I_{2x}\Big). \tag{D.12}$$

Similarly, other trilinear terms can be decomposed as follows:

$$\exp\Big(i\frac{\pi}{4}4I_{1z}I_{2x}I_{3x}\Big) = \exp\Big(-i\frac{\pi}{2}(I_{2y}+I_{3y})\Big)\exp\Big(i\frac{\pi}{4}4I_{1z}I_{2z}I_{3z}\Big)\exp\Big(i\frac{\pi}{2}(I_{2y}+I_{3y})\Big), \tag{D.13}$$

and

$$\exp\Big(i\frac{\pi}{4}4I_{1z}I_{2y}I_{3y}\Big) = \exp\Big(-i\frac{\pi}{2}(I_{2x}+I_{3x})\Big)\exp\Big(i\frac{\pi}{4}4I_{1z}I_{2z}I_{3z}\Big)\exp\Big(i\frac{\pi}{2}(I_{2x}+I_{3x})\Big). \tag{D.14}$$

Using this decomposition, we designed a pulse sequence to experimentally implement a CSWAP gate.

An NMR system is prone to different kinds of experimental errors. One of the most common errors is a pulse amplitude error, which directly reflects in the flip angle $\theta$ (as $\theta = \omega_1 t$). This can occur due to $B_1$ (rf) inhomogeneity in the sample. The other reason could also be an error in the pulse calibration. Another common error is an offset error, which corresponds to a movement of the chemical shift of a spin, resulting in pulses being off-resonance. Ideally, a pulse sequence should be robust to these two errors for a good experimental performance. In Fig. D.2, we show the error profile of the pulse sequence corresponding to the CSWAP gate.

Fig. D.2 shows that the error ($log_{10}(1-\mathcal{F}_U)$) of the CSWAP gate decreases considerably with the variation in pulse amplitude. To make it robust for the pulse amplitude error, we used a genetic algorithm [54]. For robustness optimization, the original pulse sequence of the CSWAP gate was used, and genetic algorithms optimized it for different flip angles occurring because of changes in pulse amplitude. Fig. D.3 shows the resulting error profile of the optimized pulse sequence. The optimized pulse sequence is more

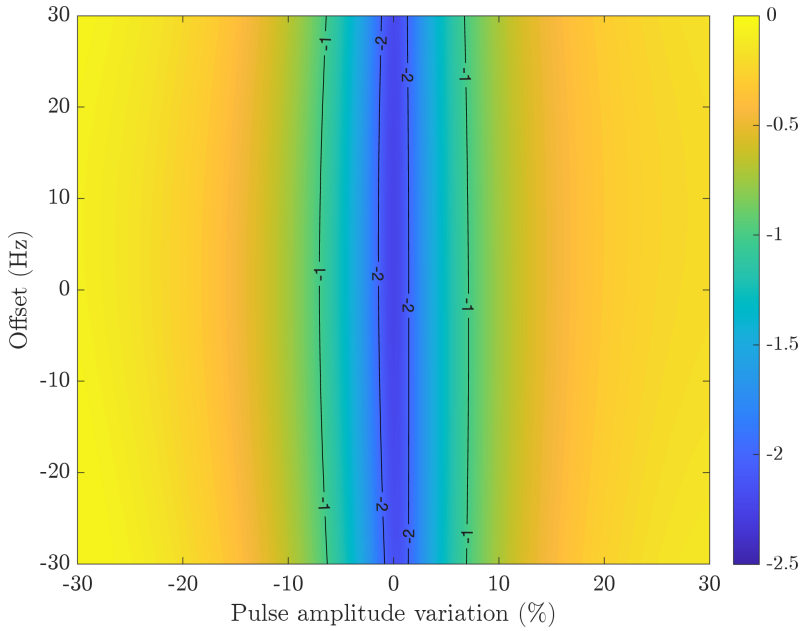


**Figure D.2:** Error profile ($log_{10}(1 - \mathcal{F}_U)$) for pulse sequence of CSWAP gate with variation in pulse amplitude ($x$ axis) and offset ($y$ axis).

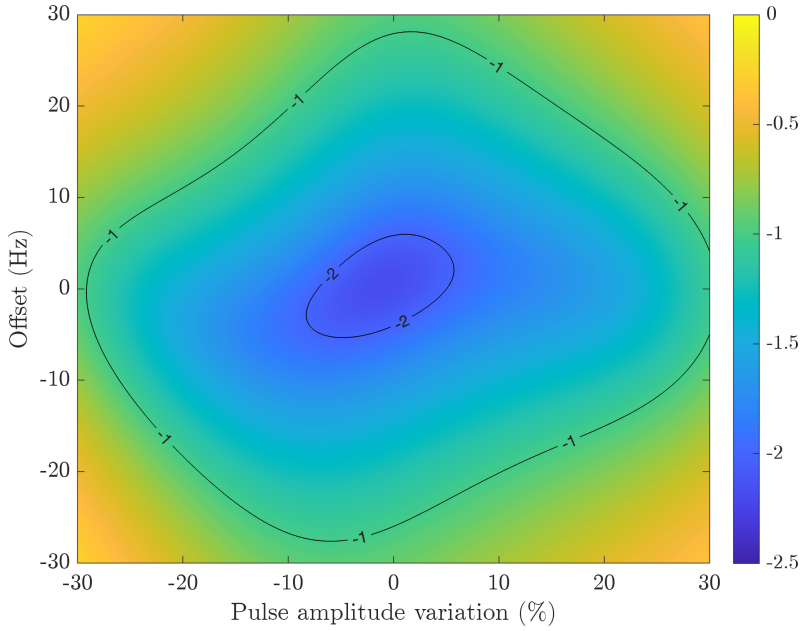


**Figure D.3:** Error profile ($log_{10}(1 - \mathcal{F}_U)$) of an optimized pulse sequence for CSWAP gate with variation in pulse amplitude ($x$ axis) and offset ($y$ axis).

robust to errors than the original sequence for the pulse amplitude variation. The

total pulse duration for the original sequence is 26.7 $\mu$sec, whereas, for the optimized sequence, the duration is 25.6 $\mu$sec.

## D.3 Experimental results

We performed the experiments for the tomography of unknown processes on a Bruker Avance III 600 MHz spectrometer using a 5 mm Shigemi tube. The preliminary experiments showed promising results for the individual blocks of the circuit (see Fig. 4.20), but the full experimental results had some errors that we could not fully understand at that point. As a result, we focused on the development of the tomography algorithms for the general-purpose pure-state quantum computer and their implementation on physical devices.

# Bibliography


[1] A. Garon, R. Zeier, and S. J. Glaser. "Visualizing operators of coupled spin systems". In: *Phys. Rev. A* 91 (4 2015), p. 042122. DOI: 10.1103/PhysRevA.91.042122.

[2] B. Schumacher. "Quantum coding". In: *Phys. Rev. A* 51 (4 1995), pp. 2738–2747. DOI: 10.1103/PhysRevA.51.2738.

[3] M. Nielsen and I. Chuang. *Quantum Computation and Quantum Information*. 10th anniversary. Cambridge: Cambridge University Press, 2010. DOI: 10.1017/CBO9780511976667.

[4] H. Goldstein, C. Poole, and J. Safko. *Classical mechanics*. American Association of Physics Teachers, 2002.

[5] M. Tesch, N. J. Glaser, and S. J. Glaser. *SpinDrops*. URL: https://spindrops.org.

[6] A. Garon. "On a new visualization tool for quantum systems and on a time-optimal control problem for quantum gates". PhD thesis. Technische Universität München, 2014. URL: http://mediatum.ub.tum.de/doc/1192392/1192392.pdf.

[7] D. Leiner, R. Zeier, and S. J. Glaser. "Symmetry-adapted decomposition of tensor operators and the visualization of coupled spin systems". In: *Journal of Physics A: Mathematical and Theoretical* 53.49 (2020), p. 495301. DOI: 10.1088/1751-8121/ab93ff.

[8] B. Koczor, R. Zeier, and S. J. Glaser. "Continuous phase-space representations for finite-dimensional quantum states and their tomography". In: *Phys. Rev. A* (2 2020), p. 022318. DOI: 10.1103/PhysRevA.101.022318.

[9] B. Koczor. "On phase-space representations of spin systems and their relations to infinite-dimensional quantum states". PhD thesis. Technische Universität München, 2019. URL: https://mediatum.ub.tum.de/doc/1463517/1463517.pdf.

[10] R. L. Stratonovich. "On Distributions in Representation Space". In: *SOVIET PHYSICS JETP* 4.6 (1957), pp. 1012–1020. URL: http://jetp.ras.ru/cgi-bin/dn/e_004_06_0891.pdf.

[11] G. Racah. "Theory of Complex Spectra. II". In: *Phys. Rev.* 62 (9-10 1942), pp. 438–462. DOI: 10.1103/PhysRev.62.438.

[12] J. D. Jackson. *Classical electrodynamics; 2nd ed.* New York, NY: Wiley, 1975.

[13] D. Leiner, R. Zeier, and S. J. Glaser. "Symmetry-adapted decomposition of tensor operators and the visualization of coupled spin systems". In: *Journal of Physics A: Mathematical and Theoretical* 53.49 (2020), p. 495301. DOI: 10.1088/1751-8121/ab93ff.

[14] D. Leiner, R. Zeier, and S. J. Glaser. "Wigner Tomography of Multispin Quantum States". In: *Phys. Rev. A* 96 (2017), p. 063413. DOI: 10.1103/PhysRevA.96.063413.

[15] B. L. Silver. "Chapter 5 - Irreducible Tensor Operators". In: *Irreducible Tensor Methods*. Ed. by Brian L. Silver. Vol. 36. Physical Chemistry: A Series of Monographs. Academic Press, 1976, pp. 51–65. DOI: https://doi.org/10.1016/B978-0-12-643650-1.50010-X.

[16] D. Leiner and S. J. Glaser. "Wigner Process Tomography: Visualization of Spin Propagators and Their Spinor Properties". In: *Phys. Rev. A* 98 (2018), p. 012112. DOI: 10.1103/PhysRevA.98.012112.

[17] S. Aaronson. "Shadow tomography of quantum states". In: *Proceedings of the 50th annual ACM SIGACT symposium on theory of computing*. 2018, pp. 325–338.

[18] H. Huang, R. Kueng, and J. Preskill. "Predicting many properties of a quantum system from very few measurements". In: *Nature Physics* 16.10 (2020), pp. 1050–1057.

[19] G. Torlai, G. Mazzola, J. Carrasquilla, M. Troyer, R. Melko, and G. Carleo. "Neural-network quantum state tomography". In: *Nature Physics* 14.5 (2018), pp. 447–450. ISSN: 1745-2481. DOI: 10.1038/s41567-018-0048-5.

[20] M. Neugebauer, L. Fischer, A. Jäger, S. Czischek, S. Jochim, M. Weidemüller, and M. Gärttner. "Neural-network quantum state tomography in a two-qubit experiment". In: *Phys. Rev. A* 102 (4 2020), p. 042604. DOI: 10.1103/PhysRevA.102.042604.

[21] D. Gross, Y. Liu, S. T. Flammia, S. Becker, and J. Eisert. "Quantum State Tomography via Compressed Sensing". In: *Phys. Rev. Lett.* 105 (15 2010), p. 150401. DOI: 10.1103/PhysRevLett.105.150401.

[22] I. L. Chuang and M. A. Nielsen. "Prescription for experimental determination of the dynamics of a quantum black box". In: *Journal of Modern Optics* 44.11-12 (1997), pp. 2455–2467. DOI: 10.1080/09500349708231894.

[23] G. Torlai, C. J. Wood, A. Acharya, G. Carleo, J. Carrasquilla, and L. Aolita. "Quantum process tomography with unsupervised learning and tensor networks". In: *Nature Communications* 14.1 (2023), p. 2858. DOI: 10.1038/s41467-023-38332-9.

[24] A. Shabani, R. L. Kosut, M. Mohseni, H. Rabitz, M. A. Broome, M. P. Almeida, A. Fedrizzi, and A. G. White. "Efficient measurement of quantum dynamics via compressive sensing". In: *Physical review letters* 106.10 (2011), p. 100401. DOI: 10.1103/PhysRevLett.106.100401.

[25] D. G. Cory, A. F. Fahmy, and T. F. Havel. "Ensemble quantum computing by NMR spectroscopy". In: *Proceedings of the National Academy of Sciences* 94.5 (1997), pp. 1634–1639. ISSN: 0027-8424. DOI: 10.1073/pnas.94.5.1634.

[26] J. A. Jones. "Quantum computing with NMR". In: *Progress in nuclear magnetic resonance spectroscopy* 59.2 (2011), pp. 91–120.

[27] A. Devra, N. J. Glaser, D. Huber, and S. J. Glaser. *DROPStomo*. URL: https://github.com/amitQC/DROPStomo.

[28] A. Devra, N. J. Glaser, D. Huber, and S. J. Glaser. *Wigner State and Process Tomography on Near-Term Quantum Devices*. 2023. DOI: 10.48550/ARXIV.2302.12725.

[29] K. Vogel and H. Risken. "Determination of quasiprobability distributions in terms of probability distributions for the rotated quadrature phase". In: *Phys. Rev. A* 40 (5 1989), pp. 2847–2849. DOI: 10.1103/PhysRevA.40.2847.

[30] U. Leonhardt. "Quantum-State Tomography and Discrete Wigner Function". In: *Phys. Rev. Lett.* 74 (21 1995), pp. 4101–4105. DOI: 10.1103/PhysRevLett.74.4101.

[31] A. G. White, D. F. V. James, P. H. Eberhard, and P. G. Kwiat. "Nonmaximally Entangled States: Production, Characterization, and Utilization". In: *Phys. Rev. Lett.* 83 (16 1999), pp. 3103–3107. DOI: 10.1103/PhysRevLett.83.3103.

[32] B. Koczor, R. Zeier, and S. J. Glaser. "Continuous phase-space representations for finite-dimensional quantum states and their tomography". In: *Phys. Rev. A* 101 (2 2020), p. 022318. DOI: 10.1103/PhysRevA.101.022318.

[33] M. Bak and N. C. Nielsen. "REPULSION, A Novel Approach to Efficient Powder Averaging in Solid-State NMR". In: *Journal of Magnetic Resonance* 125.1 (1997), pp. 132–139. ISSN: 1090-7807. DOI: https://doi.org/10.1006/jmre.1996.1087.

[34] V. I. Lebedev. "Quadratures on a sphere". In: *USSR Computational Mathematics and Mathematical Physics* 16.2 (1976), pp. 10–24. ISSN: 0041-5553. DOI: https://doi.org/10.1016/0041-5553(76)90100-2.

[35] H. J. Hogben, M. Krzystyniak, G.T.P. Charnock, P. J. Hore, and I. Kuprov. "Spinach – A software library for simulation of spin dynamics in large spin systems". In: *Journal of Magnetic Resonance* 208.2 (2011), pp. 179–194. ISSN: 1090-7807. DOI: https://doi.org/10.1016/j.jmr.2010.11.008.

[36] Florida State University. *SPHERE LEBEDEV RULE Quadrature Rules for the Sphere*. URL: https://people.sc.fsu.edu/.

[37] Y. Liang, Y. Yeh, P. E M F Mendonça, R. Y. Teh, M. D. Reid, and P. D. Drummond. "Quantum fidelity measures for mixed states". In: *Reports on Progress in Physics* 82.7 (2019), p. 076001. DOI: 10.1088/1361-6633/ab1ca4.

[38] G. Aleksandrowicz et al. *Qiskit: An Open-source Framework for Quantum Computing*. URL: https://doi.org/10.5281/zenodo.2562111.

[39] *9.10.0.2015706 (R2021a)*. The Mathworks, Inc. Natick, Massachusetts, 2021.

[40] R. A. Kennedy and P. Sadeghi. *Hilbert Space Methods in Signal Processing*. Cambridge University Press, 2013. DOI: 10.1017/CBO9780511844515.

[41] Z. Khalid, R. A. Kennedy, and J. D. McEwen. "An Optimal-Dimensionality Sampling Scheme on the Sphere With Fast Spherical Harmonic Transforms". In: *IEEE Transactions on Signal Processing* 62.17 (2014), pp. 4597–4610. DOI: 10.1109/TSP.2014.2337278.

[42] M. Edén and M. H. Levitt. "Computation of Orientational Averages in Solid-State NMR by Gaussian Spherical Quadrature". In: *Journal of Magnetic Resonance* 132.2 (1998), pp. 220–239. ISSN: 1090-7807. DOI: https://doi.org/10.1006/jmre.1998.1427.

[43] D. F. V. James, P. G. Kwiat, W. J. Munro, and A. G. White. "Measurement of qubits". In: 64 (5 2001), p. 052312. DOI: 10.1103/PhysRevA.64.052312.

[44] J. R. Driscoll and D. M. Healy. "Computing Fourier Transforms and Convolutions on the 2-Sphere". In: *Advances in Applied Mathematics* 15.2 (1994), pp. 202–250. ISSN: 0196-8858. DOI: https://doi.org/10.1006/aama.1994.1008.

[45] J. D. McEwen and Y. Wiaux. "A Novel Sampling Theorem on the Sphere". In: *IEEE Transactions on Signal Processing* 59.12 (2011), pp. 5876–5887. DOI: 10.1109/TSP.2011.2166394.

[46] J. A. Smolin, J. M. Gambetta, and G. Smith. "Efficient Method for Computing the Maximum-Likelihood Quantum State from Measurements with Additive Gaussian Noise". In: *Phys. Rev. Lett.* 108 (7 2012), p. 070502. DOI: 10.1103/PhysRevLett.108.070502.

[47] H. Singh, Arvind, and K. Dorai. "Constructing valid density matrices on an NMR quantum information processor via maximum likelihood estimation". In: *Physics Letters A* 380.38 (2016), pp. 3051–3056. ISSN: 0375-9601. DOI: https://doi.org/10.1016/j.physleta.2016.07.046.

[48] A. M. Childs, I. L. Chuang, and D. W. Leung. In: *Phys. Rev. A* 64 (1 2001), p. 012314. DOI: 10.1103/PhysRevA.64.012314.

[49] A. F. Fahmy, R. Marx, W. Bermel, and S. J. Glaser. "Thermal equilibrium as an initial state for quantum computation by NMR". In: *Phys. Rev. A* 78 (2 2008), p. 022317. DOI: 10.1103/PhysRevA.78.022317.

[50] J. M. Myers, A. F. Fahmy, S. J. Glaser, and R. Marx. "Rapid solution of problems by nuclear-magnetic-resonance quantum computation". In: *Phys. Rev. A* 63 (3 2001), p. 032302. DOI: 10.1103/PhysRevA.63.032302.

[51] R. Marx, A. Fahmy, L. Kauffman, S. Lomonaco, A. Spörl, N. Pomplun, T. Schulte-Herbrüggen, J. M. Myers, and S. J. Glaser. "Nuclear-magnetic-resonance quantum calculations of the Jones polynomial". In: *Phys. Rev. A* 81 (3 2010), p. 032319. DOI: 10.1103/PhysRevA.81.032319.

[52] A. Barenco, C. H. Bennett, R. Cleve, D. P. DiVincenzo, N. Margolus, P. Shor, T. Sleator, J. A. Smolin, and H. Weinfurter. "Elementary gates for quantum computation". In: *Phys. Rev. A* 52 (5 1995), pp. 3457–3467. DOI: 10.1103/PhysRevA.52.3457.

[53] N. Khaneja, T. Reiss, Kehlet C., T. Schulte-Herbrüggen, and S. J. Glaser. "Optimal control of coupled spin dynamics: design of NMR pulse sequences by gradient ascent algorithms". In: *Journal of Magnetic Resonance* 172.2 (2005), pp. 296–305. ISSN: 1090-7807. DOI: https://doi.org/10.1016/j.jmr.2004.11.004.

[54] A. Devra, P. Prabhu, H. Singh, Arvind, and K. Dorai. "Efficient experimental design of high-fidelity three-qubit quantum gates via genetic programming". In: *Quantum Information Processing* 17.3 (2018), p. 67. DOI: 10.1007/s11128-018-1835-8.

[55] S. J. Glaser, T. Schulte-Herbrüggen, M. Sieveking, O. Schedletzky, N. C. Nielsen, O. W. Sørensen, and C. Griesinger. "Unitary Control in Quantum Ensembles: Maximizing Signal Intensity in Coherent Spectroscopy". In: *Science* 280.5362 (1998), pp. 421–424. DOI: 10.1126/science.280.5362.421.

[56] E. Knill, I. Chuang, and R. Laflamme. "Effective pure states for bulk quantum computation". In: *Physical Review A* 57.5 (May 1998). DOI: 10.1103/PhysRevA.57.3348.

[57] J. Preskill. "Lecture notes for physics 229: Quantum information and computation". In: *California Institute of Technology* 16.1 (1998), pp. 1–8.

[58] M. Araújo, A. Feix, F. Costa, and Č. Brukner. "Quantum Circuits Cannot Control Unknown Operations". In: *New J. Phys.* 16 (2014), p. 093026. DOI: 10.1088/1367-2630/16/9/093026.

[59] Z. Gavorová, M. Seidel, and Y. Touati. "Topological Obstructions to Implementing Quantum If-Clause". In: (2022). https://arxiv.org/abs/2011.10031.

[60] X. Zhou, T. Ralph, P. Kalasuwan, M. Zhang, A. Peruzzo, B. Lanyon, and J. O'Brien. "Adding Control to Arbitrary Unknown Quantum Operations". In: *Nat. Commun.* 2 (2011), pp. 1–8. DOI: 10.1038/ncomms1392.

[61] B. Blumich and H. Spiess. "Quaternions as a Practical Tool for the Evaluation of Composite Rotations". In: *J. Magn. Reson. (1969)* 61 (1985), pp. 356–362. DOI: 10.1016/0022-2364(85)90091-5.

[62] R. R. Ernst, G. Bodenhausen, and A. Wokaun. *Principles of nuclear magnetic resonance in one and two dimensions*. BOOK. 1987.

[63] R. G. Spencer. "Equivalence of the time-domain matched filter and the spectral-domain matched filter in one-dimensional NMR spectroscopy". In: *Concepts in Magnetic Resonance Part A* 36.5 (2010), pp. 255–265. URL: https://www.ncbi.nlm.nih.gov/pmc/articles/PMC3134292/.

[64] M. Werninghaus. "Experimental Optimal Control of Superconducting Qubits". PhD thesis. Technische Universität München, 2022.

[65] M. H. Levitt. *Spin dynamics: basics of nuclear magnetic resonance*. John Wiley & Sons, 2013.

[66] I. S. Oliveira, T. J. Bonagamba, R. S. Sarthour, J. C. C. Freitas, and E. R. deAzevedo. "4 - Introduction to NMR Quantum Computing". In: *NMR Quantum Information Processing*. Amsterdam: Elsevier Science B.V., 2007, pp. 137–181. ISBN: 978-0-444-52782-0. DOI: https://doi.org/10.1016/B978-044452782-0/50006-3.

[67] J. Keeler. *Understanding NMR spectroscopy*. John Wiley & Sons, 2010.

[68] N. Khaneja, S. J. Glaser, and R. Brockett. "Sub-Riemannian geometry and time optimal control of three spin systems: Quantum gates and coherence transfer". In: *Phys. Rev. A* 65 (3 2002), p. 032301. DOI: 10.1103/PhysRevA.65.032301.

[69] T. O. Reiss, N. Khaneja, and S. J. Glaser. "Broadband geodesic pulses for three spin systems: time-optimal realization of effective trilinear coupling terms and indirect SWAP gates". In: *Journal of Magnetic Resonance* 165.1 (2003), pp. 95–101. ISSN: 1090-7807. DOI: https://doi.org/10.1016/S1090-7807(03)00245-3.